Mixing of Salt by Internal Waves

Internal waves generated over geometrical features to reduce stratification in the Rotterdam Waterway

L.M. Deen

Delft University of Technology

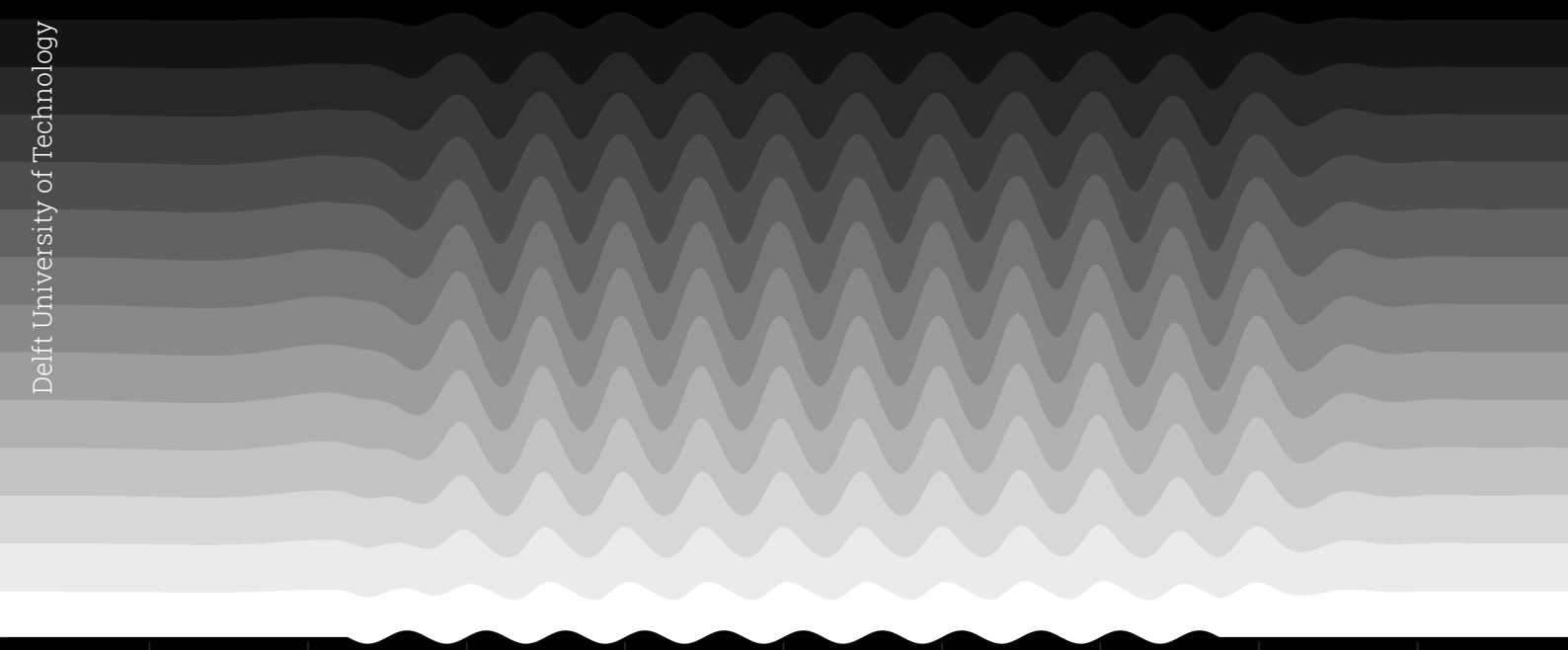

TU Delft

SVASEK HYDRAULICS
COASTAL, HARBOUR AND RIVER CONSULTANTS

Mixing of Salt by Internal Waves

Internal waves generated over geometrical features to reduce stratification in the Rotterdam Waterway

by

L.M. Deen

to obtain the degree of Master of Science

at the Delft University of Technology,

to be defended publicly on

12 November 2024 16:00 in Lecture Hall F

Student Number:	4880196	
Project Duration:	April, 2024 - November, 2024	
Thesis Committee:	Prof.dr.J.D. Pietrzak	TU Delft
	Dr.ir. R.J. Labeur	TU Delft
	Ir. T.M. Wegman	TU Delft
	Dr. A. Geyer	TU Delft
	Dr.ir. H. Talstra	Svašek Hydraulics
	Ir. S. Bom	Svašek Hydraulics

TU Delft SVAŠEK HYDRAULICS COASTAL, HARBOUR AND RIVER CONSULTANTS

Preface

This is the end... of my studies at TU Delft. The thesis you are about to read is my last step in becoming a hydraulic engineer. In the past six years, I have gotten to know the world of civil engineering and grown as a person. In my thesis, I have dived deeper into the world of internal waves. The project has taught me all about the beauty of numerical modelling and the magic of stratified flows. The Rotterdam Waterway will forever remind me of salt intrusion and whenever I walk past a river mouth all I can imagine are the internal waves propagating under the surface.

During the project, I had the pleasure of great guidance, supervision and support. Therefore, I would like to thank some people without whom this research would not have been possible. Tess, thank you for the time and effort you put into our weekly meetings and the new insights you gave me during them. I also really appreciated your enthusiasm every time I showed you the internal waves I generated in the model. I could not have done it without you. Robert Jan, thank you for your effort to explain your numerical model and the effects of the sponge layer. I am also very grateful for the time you took to provide feedback on my writing. Julie, thank you for sharing your great knowledge of internal waves and showing me the beauty of this phenomenon. Also many thanks for eating sushi with Claire, it was magical. Anna, thank you for your insights and sharp questions from a mathematical point of view, which often provided a new perspective to the problem. Harmen, thank you for your time and effort to explain the FINEL model and how to run my model simulations. I am also very grateful for your enthusiasm for numerical simulations, which was very motivating when you explained the equations behind the model. Sam, thank you for your good questions during our meetings. You always pointed out new things I had not thought about before. I would also like to thank everyone else at Svašek for having me as an intern. Thank you for making me part of your team, it was a pleasure.

Lastly, I am grateful for the support of my family and friends. Thank you all for your time and enthusiasm when listening to my stories about internal waves. Furthermore, thank you Kees* for the free coffee in the past months when I no longer had a coffee card myself. Thank you Mats for your endless love and support!

L.M. Deen
Delft, November 2024

*Kees is not the real name, the real name is known by the author.

ずっと友達でいょう

Let's always be friends.

Summary

Due to climate change, low river discharges are expected more frequently. As a result, salt intrusion in the Rotterdam Waterway will be critical at least five times more frequently, negatively impacting freshwater availability. A possible new measure to reduce salt intrusion is providing additional mixing by internal wave generation, which reduces the estuarine circulation. The potential to reduce salt intrusion in the Rotterdam Waterway by internal wave generation is investigated. To determine this the irreversible mixing generated by internal waves is quantified and related to salt intrusion length. Numerical 2DV simulations of a decelerating flow over an undular bed were executed for an idealized section of the Rotterdam Waterway. The mixing was quantified by determining the background potential energy in a chosen control volume. This method can be applied if disturbances in the velocity or density profile do not reach the boundaries of the control volume. The mixing observed in the control volume is related to salt intrusion by the buoyancy frequency of the background state. The net salt flux imported by estuarine circulation was found to be proportional to the squared buoyancy frequency. Estuarine circulation is the main forcing mechanism of salt intrusion in the seaward part of the Rotterdam Waterway. For the small idealized section of the Rotterdam Waterway, internal waves generated over geometrical features are capable of reducing the salt intrusion caused by estuarine circulation by approximately 1.7% of the initial value, if bed waves are present over 27.5% of the control volume.

Contents

Preface i

Summary iii

Nomenclature vii

1 Introduction 1
- 1.1 Context . . . 1
- 1.2 Problem statement . . . 1
- 1.3 Objective . . . 2
- 1.4 Research questions . . . 2
- 1.5 Approach . . . 2
- 1.6 Structure . . . 2

2 Literature Review 3
- 2.1 Rotterdam Waterway . . . 3
  - 2.1.1 Hydrodynamics . . . 3
  - 2.1.2 Bathymetry . . . 4
  - 2.1.3 Internal waves . . . 4
- 2.2 Salt intrusion . . . 5
- 2.3 Vertical mixing . . . 6
- 2.4 Internal waves in an estuary . . . 8
  - 2.4.1 Taylor Goldstein equation . . . 8
  - 2.4.2 Resonance conditions . . . 8
  - 2.4.3 Internal Froude number . . . 9
  - 2.4.4 Internal wave generation . . . 9
- 2.5 Summary . . . 9

3 Method 10
- 3.1 Conceptual model . . . 10
- 3.2 Approach . . . 10
- 3.3 Simulations . . . 12
  - 3.3.1 Verification runs . . . 12
  - 3.3.2 Base case . . . 12
  - 3.3.3 Variations . . . 13
  - 3.3.4 Overview simulations . . . 14
- 3.4 FINEL Model . . . 14
- 3.5 Quantification vertical mixing . . . 15
- 3.6 Reduction salt intrusion length . . . 17

4 Analysis internal wave generation 19
- 4.1 Analytical solution . . . 19
  - 4.1.1 Theoretical resonant modes . . . 19
  - 4.1.2 Propagation direction . . . 20
  - 4.1.3 Internal waves during a tidal cycle . . . 20
- 4.2 Verification internal wave generation . . . 20
  - 4.2.1 Resonant modes . . . 20
  - 4.2.2 Time scale effect . . . 22
- 4.3 Parameter variation . . . 23
  - 4.3.1 Base Case . . . 23
  - 4.3.2 Bottom friction . . . 24

4.3.3 Bed wave amplitude . . . 24
4.3.4 Stratification profile . . . 25
4.3.5 Turbulence model . . . 25
4.4 Summary . . . 25

5 Quantification irreversible mixing **27**
5.1 Verification calculation background potential energy . . . 27
5.1.1 Lock exchange . . . 27
5.1.2 Constant flow . . . 29
5.2 Decelerating flow . . . 30
5.2.1 Base case . . . 30
5.2.2 Bottom friction . . . 32
5.2.3 Bed wave amplitude . . . 34
5.2.4 Stratification profile . . . 35
5.2.5 Turbulence model . . . 36
5.3 Salt imported by estuarine circulation . . . 37
5.4 Summary . . . 37

6 Discussion **38**
6.1 Model assumptions . . . 38
6.2 Internal wave generation . . . 39
6.2.1 Resonant modes . . . 39
6.2.2 Time scale effect . . . 39
6.2.3 Propagation of internal waves . . . 40
6.2.4 Generation of internal waves during tidal cycle . . . 40
6.2.5 Stratification profile . . . 40
6.3 Evaluation quantification irreversible mixing . . . 41
6.3.1 Closed system . . . 41
6.3.2 Boundary flux . . . 41
6.4 Implications results on salt intrusion . . . 41

7 Conclusion **43**
7.1 Conclusion . . . 43
7.2 Recommendations . . . 44

References **45**

A Assumptions and approach **48**
A.1 Coriolis effect Rotterdam Waterway . . . 48
A.2 Scheme of the approach . . . 49

B Model choices **50**
B.1 Sponge layer . . . 50
B.2 Domain size . . . 53
B.3 Control volume size . . . 56
B.4 Velocity profile boundary . . . 57
B.5 Refinement . . . 58
B.5.1 Output step . . . 58
B.5.2 Grid size . . . 58

C Internal wave generation **63**
C.1 Verification internal wave generation . . . 63
C.1.1 Stationary flow . . . 63
C.1.2 Decelerating flow . . . 66
C.1.3 Accelerating flow . . . 67
C.1.4 Deceleration rate . . . 68
C.2 Parameter variation . . . 71
C.2.1 Bottom friction . . . 71
C.2.2 Bed wave amplitude . . . 71
C.2.3 Stratification profile . . . 72

C.2.4 Turbulence model 72

D Quantification irreversible mixing **82**
D.1 Analytical solution 82
D.1.1 Lock exchange 82
D.1.2 Constant flow 82
D.2 Flat bottom 82
D.3 Turbulence model 83
D.4 Salt imported by estuarine circulation 84

Nomenclature

Abbreviations

Abbreviation	Definition
LES	Large Eddy Simulation
PE	Potential Energy
BPE	Background Potential Energy

Symbols

Symbol	Definition	Unit
c	wave velocity	[m/s]
c_r	wave velocity relative to the background flow	[m/s]
C_1	$k-\epsilon$ constant	[-]
C_2	$k-\epsilon$ constant	[-]
C_μ	$k-\epsilon$ constant	[-]
C_{sm}	Smagorinsky constant	[-]
E_a	available potential energy	[J/m]
E_b	background potential energy	[J/m]
$E_{b,flux}$	background potential energy flux	[J/m/s]
$E_{b,in}$	background potential energy inflow	[J/m/s]
$E_{b,max}$	background potential energy for fully mixed condition	[J/m]
$E_{b,out}$	background potential energy outflow	[J/m/s]
$E_{b,prod}$	background potential energy production	[J/m/s]
E_p	potential energy	[J/m]
f	Coriolis parameter	[-]
g	gravitational acceleration	[m/s²]
H	water depth	[m]
h_0	bed wave amplitude	[m]
I_z	vertical integral of BPE	[J/m²]
K_H	along-channel diffusion coefficient	[m²/s]
K_S	effective vertical eddy diffusivity	[m²/s]
k	turbulent kinetic energy	[J]
k_T	bed wave number	[1/m]
N	buoyancy frequency	[1/s]
N_*	buoyancy frequency of background state	[1/s]
n	wave mode number	[-]
Ri	Richardson number	[-]
R_I	Rossby radius of deformation	[m]
u	flow velocity	[m/s]
$\overline{u}$	depth-averaged flow velocity	[m/s]
u'	deviation from depth-averaged flow velocity	[m/s]
U_0	constant uniform flow velocity	[m/s]
w	vertical velocity	[m/s]
$\hat{w}$	vertical velocity amplitude	[m/s]
s	salinity	[g/kg]

Symbol	Definition	Unit
$\overline{s}$	depth-averaged salinity	[g/kg]
s'	deviation from depth-averaged salinity	[g/kg]
s_x	derivative of s with respect to x	[g/kg/m]
x_F	upstream freshwater location in the river	[m]
x_L	left boundary of the control volume to determine BPE	[m]
x_R	right boundary of the control volume to determine BPE	[m]
z_0	reference coordinate for calculation potential energy	[m]
Δ	representative grid size	[m]
ϵ	turbulent dissipation rate	[m²/s³]
κ	molecular diffusivity of salt	[m²/s]
λ	wavelength	[m]
λ_T	bed wave length	[m]
μ_t	dynamic turbulent viscosity	[Pa]
ν_t	turbulent viscosity	[m²/s]
ρ	density	[kg/m^3]
ρ_*	reordered density	[kg/m^3]
ρ_0	reference density	[kg/m^3]
ρ_{mean}	average density in the control volume	[kg/m^3]
σ_k	$k-\epsilon$ constant	[-]
σ_ϵ	$k-\epsilon$ constant	[-]

1 Introduction

1.1. Context

Due to climate change, longer periods of lower river discharges are expected (van Vliet et al., 2013). The reduced freshwater discharge causes salt water from the sea to further penetrate landwards (Wei et al., 2016). Furthermore, the sea level is expected to rise (H. Lee et al., 2023), which will result in increased landward dispersion of the seawater. An increased salt intrusion length reduces the quality of the surface water further inland (Friocourt et al., 2014). As a result, the surface water in the Rotterdam Waterway at times does not meet the standards for agriculture or freshwater production (Kuijper & v.d. Kaaij, 2009). If this problem lasts for longer periods of time, treatment utilities or water intake locations need to be improved or relocated.

The possibility of nature-based solutions for salt intrusion is currently researched (Hendrickx et al., 2023). Nature-based solutions use the natural system, reducing cost and environmental impact (O'Hogain & McCarton, 2018). Geometrical features in a stratified flow can generate internal waves in subcritical flow conditions. The internal waves increase the mixing over the stratified water column (C. Kranenburg & Pietrzak, 1989). The increased amount of mixing has an influence on the stratification of the water column and potentially reduces salt intrusion (Pietrzak et al., 1991). Therefore, a possible nature-based solution for salt intrusion is by increased mixing of the water column by means of internal waves, resulting in a smaller vertical density difference and reduced stratification. To determine the effectiveness of mixing by internal waves a better understanding of the generation of internal waves in a stratified flow and quantification of irreversible mixing is needed.

The topic of internal waves in general has been studied before (C. Kranenburg, 1988; Long, 1955; Turner, 1979), as well as internal waves generated over the sill of fjords (Farmer & Freeland, 1983; Stigebrandt, 1976). Furthermore, internal waves in the Rotterdam Waterway have been measured (Pietrzak et al., 1990, 1991) and numerically modelled (Pietrzak & Labeur, 2004; Wegman, 2021) before. An internal wave with a larger amplitude results in a higher potential to mix the water column, because a larger surface is created for diffusion and instabilities. Internal waves with the largest amplitude are generated under resonant conditions when the free and forced wavelength are the same. During a tidal cycle, the flow conditions vary. Therefore, resonant conditions for internal waves only occur during certain periods of the tide.

1.2. Problem statement

Due to climate change, low river discharges are expected more frequently (J. Lee et al., 2024). During low river discharges, high salt concentrations are measured upstream in the estuary (W. M. Kranenburg, 2015). As a result, salt intrusion in the Rotterdam Waterway will be critical at least five times more frequently, negatively impacting freshwater availability. Measures have to be taken to reduce salt intrusion and prevent water stress. Reduction of salt intrusion length is possible by increased momentum exchange across the haloclines (Pietrzak et al., 1991), resulting in a reduction of the vertical salinity gradient. A larger momentum exchange is generated by an increased turbulence production. Internal

waves could increase the turbulence production by 30% (Labeur & Pietrzak, 2004). In earlier simulations, the irreversible mixing generated by the internal waves was not quantified or was only determined using methods that do not differentiate between stirring and irreversible mixing. Therefore, the degree of irreversible mixing by internal waves should be quantified to determine the effect of internal waves on salt intrusion.

1.3. Objective

The aim of this research is to study the degree of mixing generated by the presence of internal waves and its potential to reduce salt intrusion in the Rotterdam Waterway. The internal waves are expected to generate additional vertical mixing, which reduces the salt intrusion length. The degree of vertical mixing is dependent on the size and shape of the internal waves. The conditions leading to the largest degree of additional vertical mixing generated are determined, as well as the impact on salt intrusion length. The potential to reduce salt intrusion in the Rotterdam Waterway by means of internal wave generation is evaluated.

1.4. Research questions

The main question this research aims to answer is:

To what extent can internal waves generated over geometrical features reduce the salt intrusion in the Rotterdam Waterway?

To answer the main research question, the following sub-questions are considered:

1. *What is the relation between vertical mixing of the water column and salt intrusion?*
2. *How can additional vertical mixing by internal waves be quantified?*
3. *Which parameters influence the generation of internal waves over geometrical features?*

1.5. Approach

The research questions are answered by means of a literature study and model simulations. Using a literature review, the relations between internal waves, vertical mixing and salt intrusion length are analysed. By simulations, the influence of the processes on each other can be quantified. The simulations are run in an idealised situation using the FINEL software of Svašek Hydraulics, based on the environmental conditions of the Rotterdam Waterway.

1.6. Structure

The literature related to the research topic is described in Chapter 2. Thereafter, the approach to answer the research question is discussed in Chapter 3. In Chapter 4 the results related to the generation of internal waves are presented. Consecutively, in Chapter 5 the mixing generated by the internal waves is quantified and the reduction in salt intrusion is determined. The implications of the results are discussed in Chapter 6. Lastly, conclusions are drawn and recommendations are made in Chapter 7.

2

Literature Review

To determine the possibility of reducing the salt intrusion length in the Rotterdam Waterway by internal wave generation, first understanding of the Rotterdam Waterway and its physical processes is gained by a literature review. The Rotterdam Waterway is introduced and its characteristics are explained. Using literature the processes influencing salt intrusion are determined. Furthermore, literature relating salt intrusion length to changes in stratification profile is reviewed. Literature is used to describe the process of vertical mixing, which changes the stratification profile, as well as to determine the degree of vertical mixing. The generation of vertical mixing by internal waves is investigated. Finally, the generation of internal waves is considered.

2.1. Rotterdam Waterway

The Rotterdam Waterway is used as the case study for this research. The Rotterdam Waterway is part of the Dutch Rhine-Meuse Delta. Through the Rotterdam Waterway water from the Rhine and Meuse flows into the North Sea. There is an open connection to the sea, allowing frequent navigation into the Rotterdam harbour, as well as the intrusion of salt water. A map of the Rotterdam Waterway is shown in Figure 2.1. The hydrodynamics, bathymetry and internal wave observations of the Rotterdam Waterway are described in this section.

Figure 2.1: Map Rotterdam Waterway (Google, n.d.).

2.1.1. Hydrodynamics

The Rotterdam Waterway can be described as a partially mixed estuary during low river discharge combined with spring tide and as a stratified system during high river discharge combined with neap tide (Pietrzak et al., 1991). In the seaward part of the Rotterdam Waterway the estuarine circulation is the main forcing mechanism of landward salt transport, whereas, the depth-averaged tidal forcing

is dominant in the more landward part of the Rotterdam Waterway (W. M. Kranenburg et al., 2022). Additional mixing reduces the estuarine circulation and thereby the stratification (Hendrickx et al., 2023). Therefore, additional mixing created by internal waves would have the most effect in the seaward part of the estuary where the estuarine circulation is dominant.

The density in the Rotterdam Waterway varies between 1012 kg/m³ and 1025 kg/m³ during low and high tide respectively (Port of Rotterdam, 2021). The density difference over the vertical is assumed to be around 15 kg/m³. The location of the pycnocline, the sharp gradient in density, vertically changes during the tide (de Nijs et al., 2011). During ebb flow the vertical location of the pycnocline decreases. Conversely, during flood flow the vertical location of the pycnocline increases. However, in all time instances, the fluid is well mixed near the bottom and surface. The surface water is mixed by wind forcing and the water near the bottom by bed friction. The stratification profile that best fits the measurements of the Rotterdam Waterway is a tangent hyperbolic profile. The tangent hyperbolic profile is shown in Figure 2.2. The profile is based on Figure A.1 of Wegman (2021), which shows the stratification in the Rotterdam Waterway near Hoek van Holland.

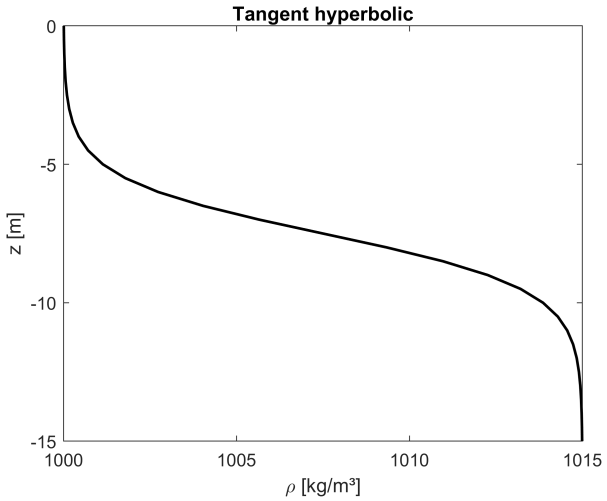

Figure 2.2: Typical tangent hyperbolic stratification profile Rotterdam Waterway.

The velocity profile that develops from the bottom is logarithmic. However, the pycnocline causes damping of bottom friction generated turbulence (de Nijs et al., 2011). Therefore, at the pycnocline, the velocity reduces and once far enough above the pycnocline, the profile is almost uniform until the surface. The depth-averaged maximum velocity in the Rotterdam Waterway is between 0.8 and 1.2 m/s, dependent on the width of the river section (van Rijn et al., 2018). The effect of Coriolis on the flow can be neglected, see Appendix A.1.

2.1.2. Bathymetry

The bottom level in the Rotterdam Waterway is between -16.40 m NAP and -14.50 m NAP (Rijkswaterstaat, 2024b). The average water level over the past 15 years at Hoek van Holland is + 0.1 m NAP (Rijkswaterstaat, 2024a). Therefore, the water depth is assumed to be 15 m for the simulations. The bed waves in the Rotterdam Waterway were measured during a field survey in 1987. The observed bed waves had a wavelength of 30-80 m and an amplitude of 0.5-1 m (Pietrzak et al., 1990). During field measurements in the Rotterdam Waterway in 2022 bed wave amplitudes of 0.2-0.3 m were observed besides bed waves of 0.5-1 m, expanding the range of bed wave amplitudes to 0.2-1 m. The bottom of the Rotterdam Waterway consists of fine to medium sand and the degree of mud increases in landwards direction (van Rijn et al., 2018). Bed ripples have a height in the order of tens of millimeters. Bed ripples for fine sand have a height of 15-20 mm (Ganju & Sherwood, 2010; Raudkivi, 1997).

2.1.3. Internal waves

Pietrzak et al. (1990) observed internal waves with amplitudes up to 4 m in the Rotterdam Waterway. Furthermore, the internal wave amplitude observed is three to four times the bed wave amplitude.

Moreover, internal waves were not observed during all parts of the tidal cycle. The mode 1 internal wave response, which results in the largest amplitudes, dominates the higher modes in field observations of the Rotterdam Waterway (Pietrzak & Labeur, 2004).

2.2. Salt intrusion

In an estuary the fresh river discharge and salt seawater meet, causing a salinity exchange. This results in a horizontal density gradient over the estuary, creating depth-dependent horizontal pressure gradients (Bowden, 1963). The bottom flow is forced landward and the surface flow is seaward. A density-driven circulation exists in the estuary and stratified layers form to create a balance of the forces, the residual flow caused by these forces is called estuarine circulation. Stratification limits the vertical length scale of the turbulent eddies and boundary layer mixing, stabilizing the stratification further (Geyer & MacCready, 2014).

The stratification in the Rotterdam Waterway is influenced by river discharge and tidal currents. A larger river discharge flushes the seawater downstream in the estuary and increases the horizontal salinity gradient (Geyer & MacCready, 2014). During ebb flow, the freshwater is strained over the salt water. The stratification created by this straining stabilizes the vertical mixing created by the tidal current. Shear stress is the main contributor to turbulence in ebb flow (Stacey & Ralston, 2005). During flood flow the salt water is strained over the fresh water, resulting in less stable stratification. The buoyancy of the freshwater, which is strained underneath the salt water, can create additional turbulence in the flow. Therefore, mixing is reduced during ebb and enhanced during flood tide (Simpson et al., 1990). During neap tide, the tidal mixing decreases compared to spring tide. The salt water is dispersed further landwards and the horizontal salinity gradient is reduced (Geyer & MacCready, 2014). However, during neap tide, the advection due to the tidal forcing is reduced, as the velocity amplitude is smaller. The total effect of these two processes decides whether neap or spring tide results in the largest salt intrusion. Tidal currents reduce the estuarine circulation by increasing mixing, which reduces stratification (Hendrickx et al., 2023). Additional mixing, for example created by internal waves, therefore, reduces the stratification as well.

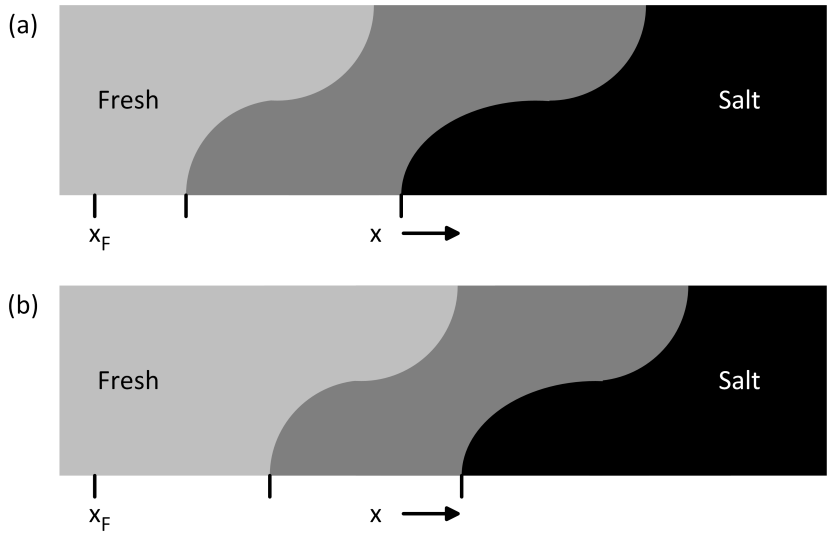

Figure 2.3: Salinity profiles in an estuary. The fresh and saltwater meet. At point x_F the water remains fresh. (a) salt intrusion. (b) reduced salt intrusion, the brackish and saltwater reach less far landwards.

The degree of salt intrusion can be described by the salt intrusion length, which is the distance the saltwater intrudes landwards. The salt intrusion length is influenced by the change in salt imported and stored in the estuary. Two different salt intrusion lengths are shown in Figure 2.3. The salt storage is larger in Figure 2.3 (a) than in (b), since the salt intrusion length is longer in (a). If the salt imported into the estuary is reduced, the salt intrusion length is reduced as well. The change in salt storage in the estuary is described by MacCready (2004) as

$$\frac{d}{dt}\int_{x_F}^{x} \overline{s} dx = -\overline{u}\,\overline{s} - \overline{u's'} + K_H \overline{s_x} \tag{2.1}$$

in which x_F the upstream location of the river where the water remains fresh, u the flow velocity, s the salinity, K_H the along-channel diffusion coefficient, the overbars represent depth-averaging, u' and s' are the deviations from the depth-averaged velocity and salinity respectively, and the subscript is the derivative with respect to the variable $\overline{s}_x = \frac{\partial \overline{s}}{\partial x}$. The first term on the right-hand side of the equation is the effect of change in river discharge, the second term is the effect of estuarine circulation and the last term is the effect of horizontal dispersion. Additional vertical mixing reduces the horizontal density gradient (Linden & Simpson, 1986). The reduced density gradient leads to a smaller buoyancy forcing, which reduces the strength of the estuarine circulation. In Subsection 2.1.1 the estuarine circulation was found to be the dominant forcing for landwards salt transport in the seaward part of the Rotterdam Waterway. Therefore, the additional mixing will be effective for that part of the Rotterdam Waterway.

Additional vertical mixing thus has an influence on $\overline{u's'}$ from Equation 2.1, which describes estuarine circulation. The effect of the estuarine circulation on the salt storage in the estuary is described by MacCready (2004) as the proportionality

$$-\overline{u's'} \propto -\frac{1}{K_S} \tag{2.2}$$

in which K_S is the effective vertical eddy diffusivity. Vertical mixing decreases the vertical density gradient, which reduces the buoyancy frequency. The buoyancy frequency is described in Equation 2.10. The vertical eddy diffusivity is related to an inverse power of the buoyancy frequency by Osborn (1980) as

$$K_S = \Gamma \frac{\epsilon}{N^2} \tag{2.3}$$

in which ϵ is the dissipation rate of turbulent kinetic energy, N is the buoyancy frequency and gamma is the flux coefficient dependent on the ratio between buoyancy and turbulence. Gamma is formulated as

$$\Gamma = \frac{R_f}{1 - R_f} \tag{2.4}$$

in which R_f is the flux Richardson number. The flux Richardson number gives the ratio of the buoyancy flux and turbulence production. Gamma has an upper limit of 0.2, at higher values of R_f the turbulence is suppressed by the buoyancy flux. A decrease in buoyancy frequency results in an increase in vertical eddy diffusivity. A larger vertical eddy diffusivity indicates more potential to mix the salt and a reduction in the salt imported by estuarine circulation.

2.3. Vertical mixing

If a salinity gradient is present in a fluid, the salt spreads by the effects of advection and diffusion. Advection transfers the salt in bulk to another location. Diffusion mixes the salt of different concentrations to a more homogeneous value. Turbulent motions can enhance this mixing process. The ability of turbulence to mix salt depends on the salinity gradient and Prandtl-Schmidt number, which is the ratio between eddy viscosity and eddy diffusivity of salt (Reynolds, 1975).

There are two types of mixing. Reversible mixing in which no transfer of salt to the surrounding area occurs. The salt is moved in the vertical and over time returns to the initial position, during this advective process the concentration stays constant. The other type is irreversible mixing. The concentration of the salt is changed in this diffusive process by transfer of salt to the surrounding area (Winters & D'Asaro, 1996). A distinction between these two processes is made using changes in potential energy. The potential energy is split into two parts. One part is background potential energy, which is the potential energy of the background state. The background state is the density profile obtained when the found density profile is redistributed to a from the bottom upwards monotonically decreasing density profile (Winters et al., 1995). The other part is available potential energy, which can be reversibly transferred to kinetic energy or irreversibly transferred to background potential energy. The available potential energy can be seen as the deviation of the mean due to the sinusoidal shape of the internal waves. In

the crest the available potential energy is positive and in the trough the available potential energy is negative. Thus the potential energy is equal to these two parts

$$E_p = E_b + E_a \tag{2.5}$$

in which E_p the potential energy, E_b the background potential energy and E_a the available potential energy. The degree of mixing in the flow is influenced by the potential energy. The stability of the flow is a measure of the amount of potential energy available for mixing (Dimotakis, 2005). In stably stratified flows an energy source is required to increase vertical overturning and generate irreversible mixing, thereby increasing the background potential energy. Whereas, in an unstably stratified flow potential energy is available for mixing. The degree of available potential energy converted to background potential energy determines the amount of irreversible mixing by the unstably stratified flow. To determine the stability of a stratified flow, the Richardson number is used. The Richardson number relates the buoyancy term to the shear rate as

$$Ri = \frac{N^2}{|\frac{\partial u}{\partial z}|^2} \tag{2.6}$$

in which N is the buoyancy frequency and $\frac{\partial u}{\partial z}$ the shear rate of the fluid. A stratified fluid is stable when $Ri > ca.\ 1/4$, assuming an inviscid, non-heat-conducting, incompressible fluid (Miles, 1961). A higher Richardson number corresponds to a stronger stratification of the flow and a lower amount of turbulence. In a stable flow the turbulence is damped by the buoyancy and the eddy diffusivity is in the order of the molecular value (Ivey et al., 2008). For unstable flow, the eddy diffusivity is dependent on the ratio of turbulence and buoyancy as described in Equation 2.3.

The vertical mixing is quantified by the changes in the background potential energy. An increase in background potential energy indicates irreversible mixing. The amount of irreversible mixing over a time interval is determined by comparing the background state of two moments in time. The background potential energy over a volume is defined by Winters et al. (1995) as

$$E_b = g \int_V \rho z_* dV. \tag{2.7}$$

In a domain with open boundaries, the background potential energy is changed by irreversible mixing and advective boundary fluxes. To determine the amount of irreversible mixing generated inside the domain of interest, the boundary influences on the background potential energy should be quantified. For open systems, the change in background potential energy over time is defined by Winters et al. (1995) as

$$\frac{1}{dt}E_b = -g \oint_S \psi \mathbf{u} \cdot \hat{\mathbf{n}} dS + \kappa g \oint_S z_* \nabla \rho \cdot \hat{\mathbf{n}} dS + \kappa g \int_V -\frac{dz_*}{d\rho} |\nabla \rho|^2 dV \tag{2.8}$$

in which $\psi = \int^{\rho} z_*(\hat{\rho}) d\hat{\rho}$, $\hat{n}$ the unit vector normal to the surface S enclosing V and κ the molecular diffusivity of salt. The first term on the right-hand side is the advective boundary flux. The second term is the diffusive boundary flux. The last term is the irreversible mixing. The diffusive boundary flux is assumed to be small compared to the advective boundary flux, since the flow velocity is much larger than the molecular and turbulent diffusion. The boundary flux over a time interval, dt, is thus calculated using

$$E_{b,flux} = -g \int_t \oint_S \psi \mathbf{u} \cdot \hat{\mathbf{n}} dS dt. \tag{2.9}$$

The mixing of a stratified fluid can be caused by different phenomena. Near the bottom the fluid is mixed by bed friction and near the surface the fluid is mixed by wind forcing. Furthermore, the fluid can be mixed by internal waves present in the water column, which can be generated by topographic features. Internal waves generate turbulence by breaking and shearing. If the turbulence is generated in regions with salinity gradients, the turbulence results in mixing. The internal waves can break due to convective overturning or shear instabilities causing Kelvin-Helmholtz instabilities (Jones et al., 2020). The possibility of shear instabilities can be determined by looking at the stability of the stratification through the Richardson number. The mixing caused by internal wave breaking is generally larger than mixing due to shear between layers of different salinity (Wunsch & Ferrari, 2004). Therefore, if the topography generates internal waves that break the most vertical mixing is obtained.

2.4. Internal waves in an estuary

Internal waves are physical phenomena, which occur in stratified fluids. Geometrical features in a waterway push the water layers up or pull them down and thereby cause displacements of the isopycnals. The flow tends to restore the displacements. In restoring, the equilibrium is overshot, creating an oscillating pattern (Huppert, 1980). This oscillation around the equilibrium is the internal wave. The strength of the oscillatory behaviour of the internal waves is described by the Brunt-Väisälä frequency or buoyancy frequency,

$$N = \sqrt{-\frac{g}{\rho_0}\frac{\partial \rho}{\partial z}} \tag{2.10}$$

with z being positive from the bottom upwards.

2.4.1. Taylor Goldstein equation

The Taylor Goldstein equation is used to describe the dynamics of internal waves. The equation is used to obtain an analytical solution of the vertical velocity pattern for different background velocities. A more complex equation does not have an analytical solution, therefore the Taylor Goldstein equation is used. The flow is assumed to be quasi-steady, therefore, at each instance of time, the solution is in a steady state. An analytical solution to the Taylor Goldstein equation exists if the topography is sinusoidal with amplitude h_0 and wave number k_T, the stratification profile is linear, the flow velocity is constant over the depth and the phase speed of the internal waves with respect to the topography is zero, $c = 0$. The vertical velocity is then described as

$$w(x,z) = \frac{U_0 k_T h_0 \sin\left(\frac{n\pi}{H}(H-z)\right)\cos(k_T x)}{\sin(n\pi)} \tag{2.11}$$

in which w is the vertical velocity, U_0 the constant background flow velocity, H the water depth and n the wave mode number (Pietrzak & Labeur, 2004).

2.4.2. Resonance conditions

Using the Taylor Goldstein equation the background velocities at which resonance occurs can be determined. These resonant conditions depend on which wave type is formed. If the background flow determines the wavelength, lee internal waves are formed. In an internally critical flow, the phase speed of long waves tends to zero, creating a stationary lee wave. This results in the accumulation of energy and resonant large amplitude internal waves (C. Kranenburg, 1988). The resonance condition is formulated as

$$|U_0| = |c_r|_{\lambda\to\infty} \tag{2.12}$$

in which c_r is the phase velocity relative to the background flow. The phase velocity relative to the background flow is expressed as

$$|c_r| = \frac{NH}{\sqrt{\frac{4\pi^2 H^2}{\lambda^2} + n^2\pi^2}} \tag{2.13}$$

in which λ is the internal wavelength. In the case of lee internal waves the wavelength is going to the long wave limit $\lambda \to \infty$. In the long wave limit, the wave number approaches zero. Therefore, the phase velocity relative to the background flow when assuming a continuously stratified fluid, N constant, is described as

$$|c_r|_{\lambda\to\infty} = \frac{NH}{n\pi} \tag{2.14}$$

with n the wave mode number, which are only positive integers for the resonant modes ($n = 1, 2, 3, ...$). If the wavelength of the topographical feature determines the wavelength of the internal waves, trapped internal waves are formed. Resonance of trapped internal waves occurs when the phase speed of a wave with the wavelength of the topography is equal to the horizontal velocity of the background flow (Pietrzak et al., 1991). The resonance condition for trapped internal waves is formulated as

$$|U_0| = |c_r|_{\lambda=\lambda_T} \tag{2.15}$$

in which λ_T is the wavelength of the topography, $\lambda_T = 2\pi/k_T$. If the topography has a monochromatic profile, the topography wavelength is a single value. Therefore, only one internal wavelength satisfies

the resonant conditions (Pietrzak & Labeur, 2004). However, resonance conditions could be met for different vertical wave modes, n. For a trapped wave in a continuously stratified fluid, the relative phase velocity is given by

$$|c_r|_{\lambda=\lambda_T} = \frac{NH}{\sqrt{k_T^2 H^2 + n^2\pi^2}}. \tag{2.16}$$

The internal wave mode describes the distribution of the vertical velocity over the vertical when resonance conditions are approached. The resonance conditions in Equation 2.12 and 2.15 excite different vertical wave modes, n. The modes are numbered according to the number of half waves in the oscillation. The first mode requires the largest background velocity. As the velocity decreases, higher modes are excited. The higher modes propagate slower and generate less internal wave energy. In a continuously stratified fluid an infinite number of vertical wave modes are possible.

2.4.3. Internal Froude number

The flow condition is described by the internal Froude number, which is an indicator for the generation of internal waves. The internal Froude number, F, describes the ratio between flow inertia and reduced gravity and is defined as

$$F = \frac{|U_0|}{|c_r|_{\lambda\to\infty}} \tag{2.17}$$

If the flow is internally supercritical, $F > 1$, internal waves are not formed. The background flow velocity is larger than the wave velocity, immediately restoring the disturbances and preventing internal wave formations (Long, 1955). For internal waves to be formed, an internally subcritical or critical flow, $F \leq 1$, is required.

2.4.4. Internal wave generation

The generation of internal waves and its amplitude depend on multiple variables. The first variable is the stratification profile. This profile influences the vertical density gradient and thereby the buoyancy frequency, N in Equation 2.10. The buoyancy frequency influences the resonance conditions of the internal waves, Equation 2.14 and 2.16. The second and third variable are the bed wave length and amplitude respectively. The length of the bed wave, λ_T, influences the resonance condition of trapped internal waves, Equation 2.16. The bed wave amplitude, h_0, influences the amplitude of the internal wave, Equation 2.11. The fourth variable that influences internal wave generation is the background flow velocity. Internal waves are not generated in supercritical flow, as described in Subsection2.4.3. Therefore, $|U_0| = |c_r|_{\lambda\to\infty}$ is the upper limit for the background flow velocity in which internal waves are generated. The background flow velocity also determines the mode that is excited. Furthermore, from Equation 2.11 follows that the background flow velocity influences the amplitude of the internal wave. The fifth variable is water depth. The wave velocity at which resonance occurs is influenced by the water depth, Equation 2.14 and 2.16. Moreover, the water depth influences the vertical density gradient, Equation 2.10. The last variable is bottom friction. Bottom friction results in shear stress. This causes additional viscous dissipation of energy, limiting the energy available for internal wave generation.

2.5. Summary

In the Rotterdam Waterway estuarine circulation is one of the main forcing mechanisms of salt import. Therefore, the salt intrusion can be reduced by increased mixing. The mixing is quantified by the change in background potential energy, which is the state of minimum potential energy over a volume. The additional mixing is generated due to the shearing or breaking of internal waves. These internal waves are generated by geometrical features. The reduction in salt intrusion is determined by the change in buoyancy frequency of the background state, which decreases if the fluid is mixed. The change in buoyancy frequency influences the vertical eddy diffusivity and the vertical eddy diffusivity is related to the salt imported by estuarine circulation. The irreversible mixing generated by the internal waves has not been quantified before. The methods to determine the mixing used before do not differentiate between stirring and irreversible mixing. The addition of this research is the quantification of irreversible mixing by internal waves and the influence on salt intrusion.

3

Method

To answer the research question multiple steps have to be taken. The relation between the processes described in Chapter 2 is studied. Thereafter, the approach to answer the research question is explained. The model used to gain more insight into the generation of internal waves, as well as the simulations planned are described. Furthermore, the method used to quantify the irreversible mixing is explained. Lastly, the method to determine the change in salt intrusion due to the mixing is described.

3.1. Conceptual model

The processes related to salt intrusion, mixing and internal waves described in Sections 2.2, 2.3 and 2.4 respectively are summarized in a conceptual model. The internal waves generated over the topography can result in additional vertical mixing of the salt. The degree of mixing can be quantified by the change in background potential energy. The additional vertical mixing results in a reduction of the stratification, which reduces the salt intrusion length. The detailed overview of the conceptual model for salt intrusion in an estuary is shown in Figure 3.1. The aim of the research is to determine the influence of internal waves on mixing and salt intrusion. Therefore, the main variables of interest are internal wave amplitude and internal wave energy, as well as the effect of these variables on mixing and salt intrusion. To simplify the model, the river discharge, water depth and bed wave length are kept constant, for which typical values are chosen characterising the Rotterdam Waterway. The background flow velocity is assumed to be only a function of time, which follows a M2 tidal circulation. The other tidal effects are neglected.

3.2. Approach

Using the conceptual model the parameters influencing the internal wave generation are determined. Based on the relations found in the conceptual model the influence of the bottom friction, stratification profile and bed wave amplitude on the generation of internal waves are explored. To isolate the influence of each variable on internal wave generation and mixing, the problem is simulated in a model. In a model, each variable can be varied independently. Therefore, the process of internal wave generation is first analysed using a very simplified case. Thereafter, complexity is added to each consecutive simulation.

Firstly, the internal waves generated in the model are compared to the theoretical Taylor Goldstein solution. Based on this the model's ability to represent the internal waves is determined. Thereafter, the bottom friction, stratification profile and bed wave amplitude are varied in simulations and the influence on internal wave generation is analysed. The next step is to determine the mixing generated by the internal waves. The mixing is quantified by determining the background potential energy. The calculation of the background potential energy is executed for a simplified case and compared to the analytical solution. In this way, the accuracy of the calculated background potential energy is determined. Thereafter, the background potential energy is determined for the more complex simulations including bed waves, bottom friction or tangent hyperbolic stratification. Lastly, the mixing generated by the internal waves is related to the salt intrusion length. A schematic of the approach is shown in Appendix A.2.

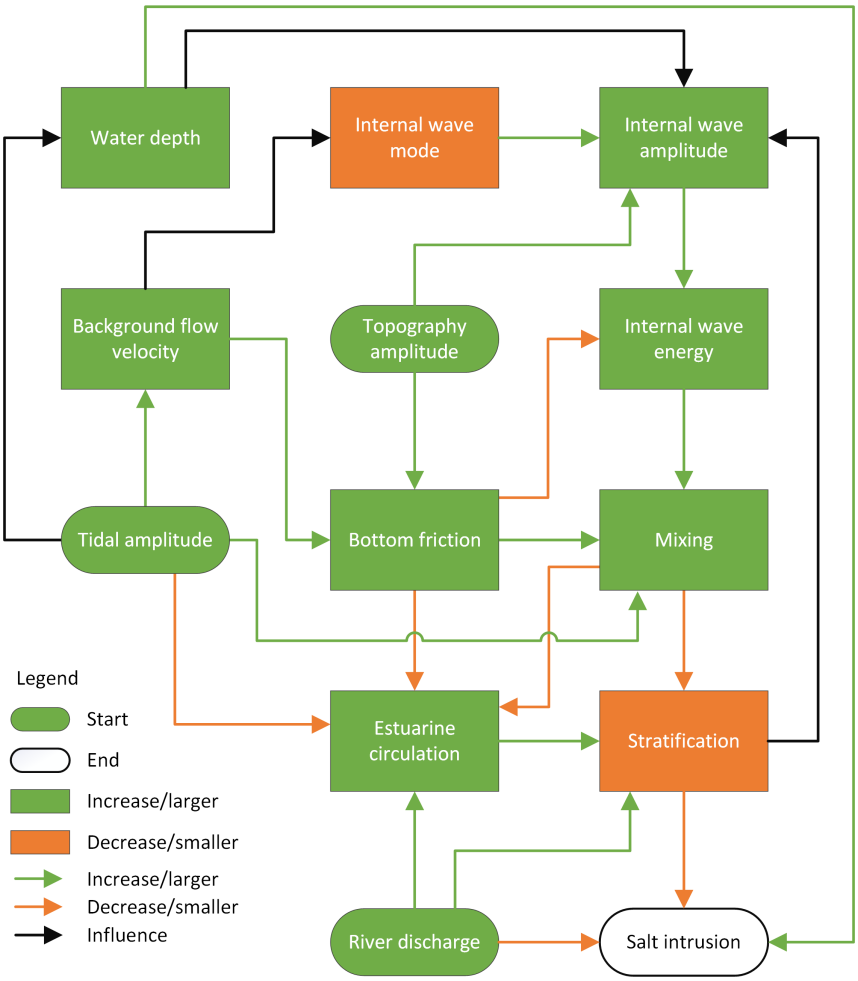

Figure 3.1: Overview of the connections between the processes relevant to salt intrusion and internal wave generation. The green color of a variable indicates the quantity increases. Conversely, an orange color indicates a decrease. A green arrow coming from a green source variable indicates the increased source variable results in an increase in the dependent variable. A green arrow coming from an orange source variable indicates the decreased source variable results in an increase in the dependent variable. Conversely, an orange arrow indicates a decrease. A black arrow indicates the source variable influences the dependent variable, however, this relation can be both positive and negative.

3.3. Simulations

Verification simulations are run to compare model results with theory. The base case for the simulations is chosen based on resemblance to the theory. Environmental conditions used in the model are based on the Rotterdam Waterway. An overview of the typical environmental conditions in the Rotterdam Waterway is shown in Table 3.1, which is based on the findings in section 2.1. The entire model set-up for the base case is explained in this section. Different variations of the base case are tested to investigate the influence of the turbulence model, bottom friction and stratification profile on the generation of internal waves and its additional mixing. An overview of the variations of the base case is presented. By comparing the simulations most similar to the Rotterdam Waterway and a simulation with a flat bed the additional mixing by internal waves can be determined.

Table 3.1: Environmental conditions characterising the Rotterdam Waterway

Parameter	Value
depth	15 m
bed wave amplitude	0.5 m
bed wave length	50 m
maximum velocity amplitude	1 m/s
vertical density difference	15 kg/m³
stratification profile	tangent hyperbolic

3.3.1. Verification runs

The simulations to verify the internal waves generated in the model align with expectations from theory are done in the same domain as the base case, which is explained in Subsection 3.3.2. The only difference is the velocity prescribed at the boundaries. To compare the results to the stationary Taylor Goldstein solution a constant velocity is prescribed at the boundaries. To analyse the time scale needed for the resonance to grow simulations using a linearly decreasing velocity are analysed. Lastly, a comparison is made between an accelerating and decelerating flow. An overview of the velocity signals as a function of time prescribed at the boundaries is shown in Table 3.2.

Table 3.2: Overview of verification simulations.

Run	Velocity [m/s]
v1	0.40
v2	0.36
v3	0.22
v4	0.18
v5	0.15
v6	$0.5 - 9.3 \cdot 10^{-5}\ t$
v7	$0.5 - 4.6 \cdot 10^{-5}\ t$
v8	$0.5 - 5.4 \cdot 10^{-6}\ t$
v9	$0.5 \cos(\frac{\pi t}{22350})$
v10	$0.5 \sin(\frac{\pi t}{22350})$

To verify the method to determine the background potential energy is implemented correctly, simulations of a lock exchange in a closed domain are performed. The results of the initial state can be compared to analytical solutions. To verify the calculation of the background potential energy boundary fluxes is correct a simulation in the same domain as the base case is performed except the bottom profile is flat and the background velocity is kept constant at 0.3 m/s. In this way, the background potential energy boundary flux can be compared to the theoretical value.

3.3.2. Base case

The reference case has a 3600 m long domain, since the solution is then independent of the domain size, see appendix B.2. On both ends of the domain, a sponge layer of 100 m is present to force the solutions to the boundary conditions and avoid reflection of internal waves at the boundary. The

simulation time is 11175 seconds, which is a quarter of the M2-tidal cycle. The analysis focuses on the internal wave generation on the decelerating tide. Thus, 11175 seconds of the M2-tide result in only the decelerating part of the tide. The density difference over the vertical is 15 kg/m³ and the water depth is 15 m, both are based on observed values in the Rotterdam Waterway. The stratification profile over the vertical is linear to allow comparison to theory. The bottom boundary has no friction to avoid additional mixing due to bed friction and isolate the effect of the internal waves. The bottom topography consists of 11 bed waves of wavelength 50 m, based on observations in the Rotterdam Waterway, and a bed wave amplitude of 0.15 m. A smaller bed wave amplitude than observed in reality is chosen since the amplitude of the internal waves grows to about 7 times the bed wave amplitude if bottom friction is excluded. The top boundary condition is a rigid-lid to eliminate the effect of surface waves on energy generation. In simulations with a free surface, a surface wave is going back and forth through the domain, disrupting the velocity signal and internal wave generation. At both horizontal boundaries a velocity profile following an M2-tide with velocity amplitude 1 m/s is prescribed by $u(t) = \cos(\frac{\pi}{22350}t)$. The velocity is uniform over the depth to allow comparison to theory. Furthermore, at both boundaries, a continuously stratified salinity profile is prescribed. The grid size is 1 m horizontal and on average 0.5 m in the vertical. The size is based on the expected internal wavelength of 50 m, which is equal to the bed wavelength and the necessity to have enough points to capture the internal wave and avoid aliasing. Furthermore, grid sizes of the same order magnitude have been used in similar simulations by Pietrzak and Labeur (2004) and Wegman (2021). The time step of the simulations is 1 second. In this way, the Courant number remains one or lower. The simulation begins with a cold start. The initial velocity field is zero and the initial stratification profile is linear. The internal waves start to generate at velocities around 0.4 m/s and the velocity decreases from 1 m/s to zero following an M2-tide, about 8200 seconds have passed when the background velocity reaches 0.4 m/s. Therefore, enough time is available for the system to adapt to the velocity forcing before the internal waves are generated. For the turbulence closure Large Eddy Simulation (LES) is used with a Smagorinsky constant of 0.10.

3.3.3. Variations

Four variations of the base case are considered. The turbulence model, bottom friction, stratification profile and bed wave amplitude are varied. To determine the significance of the amount of the additional mixing generated, the influence of the type of turbulence model on the increase in potential energy is researched. Therefore, the results using LES, k-ϵ and constant eddy viscosity turbulence models are analysed.

Another variation researched is bottom friction. The Rotterdam Waterway has a rough bottom. Furthermore, bottom friction dissipates part of the energy available for internal wave formation by viscous dissipation, limiting the amplitudes of the internal waves (Wegman, 2021). Bottom friction influences the mixing near the bed and reduces the stratification in the boundary layer. This is all more in line with observed internal wave amplitudes in the Rotterdam Waterway, therefore bottom friction is a better representation of reality. The bottom friction is modelled using a Nikuradse roughness height of 0.02 m. Furthermore, the velocity at the boundaries is prescribed using a logarithmic profile over the depth for simulations using bottom friction. The determination of the logarithmic profile prescribed at the boundaries for the case with bottom friction is described in Appendix B.4.

The amplitude of the bed waves is chosen to be 0 m (a flat bed), 0.15 m or 0.5 m. Bed waves of 0.15 m are used in earlier numerical simulations of internal waves (Labeur & Pietrzak, 2004, 2005; Pietrzak & Labeur, 2004). Furthermore, these bed waves result in a reasonable internal wave height for the frictionless case. For simulations with bottom friction, a larger bed wave amplitude is needed to obtain internal wave amplitudes similar to the values observed in reality. Due to the dissipated energy by bed shear the vertical velocity is reduced near the bed and the amplitude of the generated internal waves is smaller. Bed waves with 0.5 m amplitude are observed in the Rotterdam Waterway. The simulations with a flat bed, bed wave amplitude 0 m, are used to estimate the mixing created by the bed waves by determining the difference between the undular and flat bed.

The last variation is the stratification profile. A continuously stratified fluid and a tangent hyperbolic stratified fluid are analysed. The first is to compare simulations to the Taylor Goldstein equation, which assumes a continuously stratified fluid. The second represents the stratification profile in the Rotterdam Waterway, which allows for researching mixing by internal waves in the Rotterdam Waterway.

3.3.4. Overview simulations

In table 3.3 an overview of the parameter variations is given. If the bed wave amplitude is above zero, bed waves are present in the domain over $-275 \leq x \leq 275$. In all simulations the background velocity decreases using $u(t) = \cos\left(\frac{2\pi}{44700}t\right)$. To determine the influence of the turbulence model runs 0, 1 and 2 are compared, as well as 3, 4, 5. To determine the effect of bed friction on internal wave generation and mixing runs 0 and 6 are compared. The effect of bed wave amplitude is determined by comparing run 0 to run 3 and run 6 to run 7. By comparing run 0 to run 9 the effect of a different stratification profile is investigated. To estimate the additional mixing in the Rotterdam Waterway due to internal waves run 3 is compared to run 10.

Table 3.3: Overview of the model simulations.

Run #	Turbulence model	Bed friction [m]	Bed wave amplitude [m]	Stratification profile
0 (base)	LES	0	0.15	linear
1	k-epsilon	0	0.15	linear
2	constant eddy viscosity	0	0.15	linear
3	LES	0	0.5	linear
4	k-epsilon	0	0.5	linear
5	constant eddy viscosity	0	0.5	linear
6	LES	0.02	0.15	linear
7	LES	0.02	0.5	linear
8	LES	0.02	0.5	tangent hyperbolic
9	LES	0	0.15	tangent hyperbolic
10	LES	0	0	linear

3.4. FINEL Model

The model used for the simulations is FINEL, which is developed by Labeur (2009) and Svašek Hydraulics. FINEL is a non-hydrostatic model based on the finite element method. The non-hydrostatic nature of the model allows resolving of internal waves. The model is based on the incompressible Navier-Stokes equations and the Boussinesq approximation is made.

The FINEL model is described in detail in Labeur (2009). The governing momentum, transport and continuity equation, on which the model is based, are given in Equations 3.1, 3.2 and 3.3 below respectively, in which ν_t is the turbulent viscosity.

$$\frac{\partial \mathbf{u}}{\partial t} + (\mathbf{u} \cdot \nabla)\mathbf{u} + \frac{1}{\rho_0}\nabla p - \nabla \cdot (\nu_t \nabla \mathbf{u}) = -\frac{\rho}{\rho_0} g \mathbf{e}_z \tag{3.1}$$

$$\frac{\partial (\rho - \rho_0)/\rho_0}{\partial t} + \mathbf{u} \cdot \nabla (\rho - \rho_0)/\rho_0 = \nabla(\kappa \nabla (\rho - \rho_0)/\rho_0) \tag{3.2}$$

$$\nabla \cdot \mathbf{u} = 0 \tag{3.3}$$

The grid used for the simulations is built of finite elements. The flow over topographical features is simulated in a 2-dimensional vertical plane. Therefore, the grid consists of triangular elements. At the velocity boundaries of the domain a sponge layer is applied. In the sponge layer, the solution of the domain is forced to the conditions prescribed at the boundaries. To create a smooth transition the flow is slowly adapted to the boundary conditions over the length of the sponge layer using a relaxation constant which follows a cosine shape. The reduction in reflection at the boundary due to the sponge layer is shown in Appendix B.1.

Three turbulence closure models are applied in different simulations. Large Eddy Simulation (LES) resolves the largest eddies in the simulation based on the grid size. The subgrid scale is resolved by a constant value for each grid cell based on the stresses observed. The viscosity for the Large Eddy

Simulation is determined as follows

$$\nu_t = (C_{sm}\Delta)^2 \sqrt{\left(\frac{\partial u_i}{\partial x_k} + \frac{\partial u_k}{\partial x_i}\right)\frac{\partial u_i}{\partial x_k}} \tag{3.4}$$

in which C_{sm} is the Smagorinsky constant, which is dependent on the flow type, and Δ is the representative grid size, determined using $\Delta = \sqrt{\Delta x \Delta z}$ for a 2D vertical grid (Deardorff, 1970). Another possibility is the $k-\epsilon$ model. In the $k-\epsilon$ model the transport equations of the turbulent dissipation and turbulent kinetic energy are coupled to determine the turbulent viscosity locally. The transport equation for turbulent dissipation, the transport equation for turbulent kinetic energy and the dynamic turbulent viscosity are shown below in Equation 3.5, 3.6 and 3.7 respectively

$$\frac{D\epsilon}{Dt} = \frac{1}{\rho}\frac{\partial}{\partial x_k}\left(\frac{\mu_t}{\sigma_\epsilon}\frac{\partial \epsilon}{\partial x_k}\right) + \frac{C_1\mu_t}{\rho}\frac{\epsilon}{k}\left(\frac{\partial u_i}{\partial x_k} + \frac{\partial u_k}{\partial x_i}\right)\frac{\partial u_i}{\partial x_k} - C_2\frac{\epsilon^2}{k^2} \tag{3.5}$$

$$\frac{Dk}{Dt} = \frac{1}{\rho}\frac{\partial}{\partial x_k}\left(\frac{\mu_t}{\sigma_k}\frac{\partial k}{\partial x_k}\right) + \frac{\mu_t}{\rho}\left(\frac{\partial u_i}{\partial x_k} + \frac{\partial u_k}{\partial x_i}\right)\frac{\partial u_i}{\partial x_k} - \epsilon \tag{3.6}$$

$$\mu_t = C_\mu \rho \frac{k^2}{\epsilon} \tag{3.7}$$

in which μ_t is the dynamic turbulent viscosity $\nu_t = \mu_t/\rho$, k is the turbulent kinetic energy and C_1, C_2, C_μ, σ_ϵ, σ_k are constants dependent on the flow type. The values of these constants for mixing layers are described in Table 2.1 of Launder and Spalding (1983). The last turbulence model of interest is constant eddy viscosity. In this turbulence model, the viscosity of the turbulent motion is set to a constant value for each grid point.

3.5. Quantification vertical mixing

To determine the degree of irreversible mixing the background potential energy is calculated. By post-processing the output from the FINEL simulations, the change in background potential energy over time is estimated. The background potential energy is determined using Equation 2.7. In this case, the domain is two dimensional, therefore, the volume integral becomes a surface integral. Each grid point is assumed to be an infinitely small fluid element. The first step is to determine the control volume over which the background potential energy is calculated. The boundaries of the control volume have to be chosen far enough away from the bed waves to avoid internal waves passing the boundary and disrupting the energy fluxes determined. Furthermore, the boundaries of the control volume should be far enough away from the sponge layer to avoid disruption of the energy fluxes due to the relaxation in the sponge layer. Moreover, a larger domain results in a smaller fraction of the domain in which mixing occurs and therefore a smaller relative increase in potential energy. The size of the control volume is chosen at $-1000 \leq x \leq 1000$. This is determined by analysing the results of calculations using different control volumes in appendix B.3. The integral to determine the background potential energy including the boundaries for the control volume based on the equations of Winters et al. (1995) becomes

$$E_b = g\int_{x_L}^{x_R}\int_{z_0}^{z} \rho z_* dz dx. \tag{3.8}$$

in which x_L is the left boundary of the control volume and x_R is the right boundary of the control volume. A simplified sketch of the grid with an example control volume is shown in Figure 3.2.

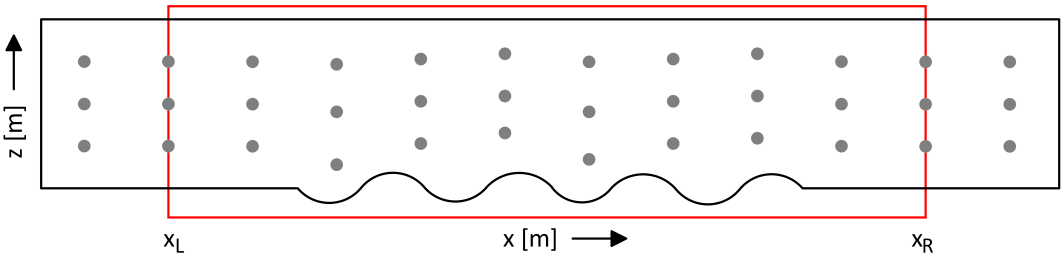

Figure 3.2: Sketch of the FINEL domain including grid points, control volume and x-coordinates of the control volume. The red rectangle indicates the control volume.

Secondly, the reference position in a state of minimum potential energy, z_*, of each fluid element in the control volume is determined. This is done by sorting the density profile in a descending order and the z-coordinates in an ascending order using all grid points in the control volume. The highest density values are matched with the location (x,z) of the smallest z-coordinates. This results in an array of densities for which the heaviest fluid element has x,z-coordinates which correspond to the smallest z-coordinate and conversely the lightest elements have coordinates corresponding to the highest z-coordinate. The obtained array is called ρ_*. An example of an initial density profile, ρ, and the corresponding reordered density profile, ρ_{star} are plotted in Figure 3.3 (a) and (b) respectively. Since the density values are reordered to a state of minimal potential energy when ρ_* is used, the reference position is equal to the z-coordinate, $z_* = z$.

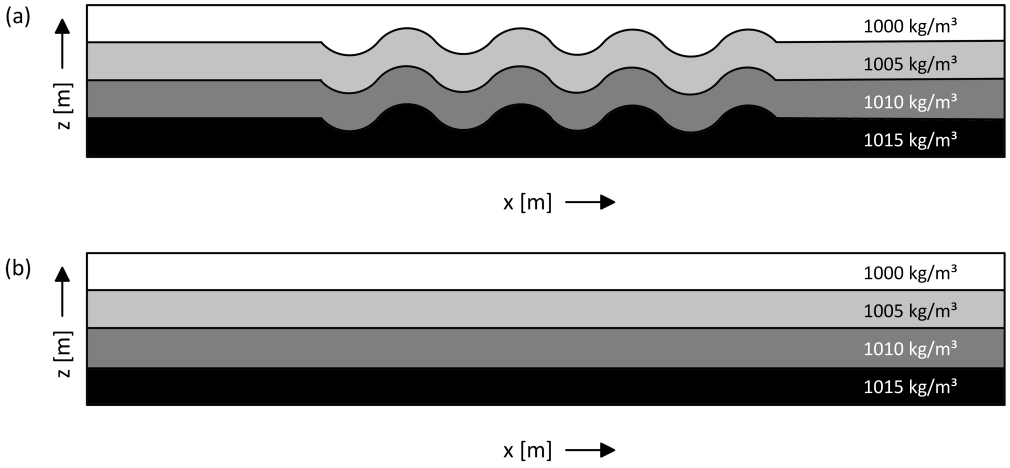

Figure 3.3: Density profiles. (a) Density resulting from the FINEL simulation, $\rho(x, z)$. (b) Reordered density to a state of minimum potential energy, $\rho_*(x, z)$.

To obtain the background potential energy, the third step is to integrate $\rho_* z$ over the control volume and multiply it by the gravitational acceleration. The numerical integration is done using the trapezoidal method. Thereby, the density field is approximated as a linear function between two fluid elements. First, the z-direction is integrated. Due to the bed waves the spacing is non-uniform in this direction. Therefore, the chained trapezoidal rule is applied using

$$\int_{z_0}^{z} \rho_*(x,z)z(x)dz \approx \sum_{i=1}^{n_z} \frac{\rho_*(x,z_i)z_i(x) + \rho_*(x,z_{i+1})z_{i+1}(x)}{2}(z_{i+1}(x) - z_i(x)) = I_z(x) \tag{3.9}$$

in which z_0 is the reference level for the potential energy, n_z is the number of vertical layers in the grid and I_z is a shorter notation for the summation. The reference level used in FINEL is the surface. Therefore, all z-coordinates are negative. To have a positive value for the potential energy the z-coordinates are converted to positive values. This is done by choosing the reference level for the potential energy, z_0, slightly below the bed waves at 16 m below the surface and adding this value to the z-coordinates outputted by FINEL. The number of vertical layers is constant over the domain. Secondly, integration over the x-direction is done. The spacing is uniform in this direction. Therefore, combined with Equation 3.9 the following trapezoidal rule is used for the integration over both directions

$$E_b = g\int_{x_L}^{x_R}\int_{z_0}^{z} \rho_*(x,z)z(x)dzdx \approx g\frac{\Delta x}{2}\sum_{j=1}^{n_x}(I_z(x_j) + I_z(x_{j+1})) \tag{3.10}$$

in which Δx is the horizontal grid spacing and n_x is the number of horizontal grid intervals.

The next step is to determine the background potential energy fluxes at the boundary using Equation 2.9. The flux is integrated over the vertical at the left and right boundary of the control volume. Since the simulations are done using rigid-lid and a closed bottom, only boundary fluxes in the horizontal direction are present. The flow in the domain is positive from left to right. At the left boundary the flow

into the domain is positive and results in an increase in potential energy in the control volume. The flow at the right boundary out of the domain is positive, resulting in a decrease in potential energy. The boundary flux becomes

$$E_{b,flux} = g \int_t \int_z \rho(x_L) z_*(x_L) u(x_L) dz dt - g \int_t \int_z \rho(x_R) z_*(x_R) u(x_R) dz dt. \tag{3.11}$$

In this case, the density is again reordered over the vertical and the index of the z-coordinates is changed according to the indices of the reordered density, resulting in z_*. To simplify the notation the left flux is defined as

$$E_{b,in} = g \int_z \rho(x_L) z_*(x_L) u(x_L, z) dz$$

and the right flux is defined as

$$E_{b,out} = g \int_z \rho(x_R) z_*(x_R) u(x_R, z) dz.$$

The integral in z-direction is again solved using the chained trapezoidal rule. The output rate of FINEL is every 75 seconds, this choice is justified in appendix B.5.1. The flux of background potential energy over the boundary of the control volume is calculated by linearly interpolating two time steps as shown below

$$E_{b,flux} = \frac{E^m_{b,in} - E^m_{b,out} + E^{m+1}_{b,in} - E^{m+1}_{b,out}}{2} t_{map} \tag{3.12}$$

in which m is the time step of interest and t_{map} the output rate.

The final step is to calculate the production of background potential energy in the control volume using conservation of energy. The change in background potential energy between two time steps is balanced by the background potential energy flux and production as described in the equation below

$$\Delta E_b = E_{b,flux} + E_{b,prod} \tag{3.13}$$

in which $E_{b,prod}$ is the production of background potential energy. A negative value for the production would indicate dissipation of background potential energy, which is not expected to occur since the creation of background potential energy is irreversible. Therefore, the only way background potential energy possibly decreases in time is due to the boundary fluxes.

To create a reference point for the change in background potential energy observed the found value is related to the background potential energy found when the control volume is completely mixed. The background potential energy in the mixed condition is determined by calculating the mean density of the control volume, multiplying this with the z-coordinate of each grid point and integrating this over the control volume. The following equation is used

$$E_{b,max} = g \int_{x_L}^{x_R} \int_{z_0}^{z} \rho_{mean} z dz dx \tag{3.14}$$

in which ρ_{mean} is the mean density over the control volume.

3.6. Reduction salt intrusion length

Using equations from literature a relation between vertical mixing and salt imported due to estuarine circulation is found. A decrease in buoyancy frequency results in an increase in vertical eddy diffusivity. In Equation 2.2 it can be seen that the salt import by estuarine circulation is inversely proportional to vertical eddy diffusivity. The vertical eddy diffusivity is inversely proportional to the buoyancy frequency, as depicted in Equation 2.3. Combining Equation 2.2 and 2.3 results in the following proportionality

$$-\overline{u's'} \propto N^2. \tag{3.15}$$

An increase in vertical mixing, and thereby in stratification profile, results in a decrease of the import of salt by estuarine circulation and thus a decreased salt intrusion length, assuming all other parameters in the equations remain unchanged. To determine the influence of irreversible mixing on the stratification

profile the buoyancy frequency of the background state is determined. Changes in the background state indicate irreversible mixing. Therefore, a change in the buoyancy frequency of the background state is used to relate the irreversible mixing to the reduction in salt imported by estuarine circulation. The buoyancy frequency of the background state is based on equation 2.10 and expressed as

$$N_*^2 = -\frac{g}{\rho_0}\frac{\partial \rho}{\partial z_*} \tag{3.16}$$

in which ρ_0 is the reference density and z_* the reference position in the state of minimum potential energy (Winters et al., 1995). The buoyancy frequency of the background state is determined between every two vertically adjacent grid points in the control volume using

$$N_{*(i,j)}^2 = -\frac{g}{\rho_0}\frac{\rho_{*(i+1,j)} - \rho_{*(i,j)}}{z_{(i+1,j)} - z_{(i,j)}}. \tag{3.17}$$

Thereafter, the mean value is taken over each horizontal layer in the domain. In this way, the reordering errors are reduced. Only linearly stratified profiles are analysed, since the buoyancy frequency can then be assumed independent of depth. Therefore, the mean value is taken over the vertical to create one depth-averaged buoyancy frequency of the background state for each time step.

The change in buoyancy frequency of the background state between the first and last time step is an indication of the change in salt storage. The results of a case including bed waves are compared to the results of the same simulation with a flat bottom. Hereby, the spin-up effects at the start of the simulation are removed, as well as the diffusion generated by effects other than the internal waves, which is the diffusion found in the case of a flat bed.

4

Analysis internal wave generation

In this chapter, the model results are verified by comparison to an analytical solution. Furthermore, the period during a decelerating tide in which internal waves are present is determined. Lastly, the effects of bottom friction, bed wave amplitude and stratification profile on the generation of internal waves are investigated.

4.1. Analytical solution

Using the literature review in Chapter 2, theoretical expectations of the generation of internal waves in the Rotterdam Waterway are made. The background velocity at which the resonant modes occur, as well as the propagation direction of the internal waves are predicted. Furthermore, the time scale effect of the resonant response is investigated.

4.1.1. Theoretical resonant modes

Based on the environmental conditions in the Rotterdam Waterway and using the Taylor Goldstein equation an estimate is made of the background velocity at which the respective resonant mode occurs. The analytical resonant conditions for the base case are shown in Table 4.1. The vertical velocity is plotted against the background velocity in Figure 4.1 and shows the resonance peaks. When the background flow approaches the resonance conditions a sharp increase in vertical velocity occurs, resulting in large internal waves.

Table 4.1: Background velocities at which resonant modes occur according to the Taylor Goldstein equation for continuously stratified conditions with a density difference of 15 kg/m³ over 15 m water depth and bed waves of length 50 m.

Resonant mode	Background velocity [m/s]
1	0.406
2	0.226
3	0.155
4	0.117
5	0.094

In the simulations of interest the background velocity decreases, the rate of change influences the applicability of the quasi-steady flow assumption used in the Taylor Goldstein equation. Because of this assumption, the Taylor Goldstein equation is independent of time. However, when the resonance conditions are excited the wave amplitudes need time to grow and reach their resonance equilibrium. If the time scale to reach the equilibrium is larger than the time needed to decrease the background velocity, the maximum amplitude occurs at a lower background velocity than expected. Furthermore, the model simulations contain viscosity, which is needed for a physically stable flow with an energy dissipation that matches the situation in the Rotterdam Waterway. These differences between the model simulations and analytical solution could cause non-linear behaviour in the model results and a difference between the model results and analytical solution. Non-linear effects are observed when

the internal wave shape deviates from the sinusoidal shape predicted by linear theory, such as wave skewness. Furthermore, the phase speed of the internal waves can be influenced by non-linear effects.

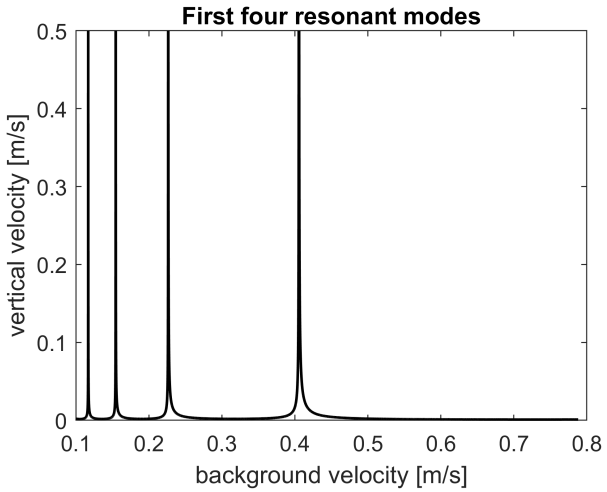

Figure 4.1: First four resonant peaks and the corresponding background velocity. Results shown are for bed waves of length 50 m, water depth of 15 m and density difference of 15 kg/m³ over the vertical.

4.1.2. Propagation direction

When the internal waves are generated the wave velocity can be determined using the background velocity and stratification profile. In the case of trapped internal waves, the wave velocity is equal to the background velocity, but with an opposite sign. As the background flow decelerates over time, the internal waves generated at an earlier time step than the present are expected to have a higher wave velocity than the present background velocity, since the internal waves were formed by a higher background velocity. Therefore, the internal waves are expected to propagate upstream. During the simulations, internal waves are expected to form above the bed waves and in the lee of the last bed wave. As the flow decelerates the internal waves are expected to propagate upstream until the internal wave energy has dissipated.

4.1.3. Internal waves during a tidal cycle

As described in Subsection 2.4.4 internal waves can only be generated during subcritical flow. The flow in the Rotterdam Waterway is subcritical when the absolute value of the velocity is equal to or lower than 0.47 m/s, which is determined using equation 2.14 and 2.17. During a quarter of the tidal cycle in the model simulations the velocity decreases from 1 to 0 m/s using the cosine function $u(t) = \cos\left(\frac{2\pi}{44700}t\right)$. Therefore, during 69% of the decelerating tide the flow is supercritical and no internal waves are generated. Once the background velocity drops below 0.47 m/s the resonant modes start to appear as the flow decelerates further to the velocities given in Table 4.1 and diapycnal mixing of salt is expected to occur.

4.2. Verification internal wave generation

The density and vertical velocity are analysed in animations of the simulations. The vertical velocities observed in stationary flow simulations are compared to theory to verify the model results. Moreover, the background velocities at which the resonant modes occur are determined using the density profile. Furthermore, the time dependence of the modes is investigated.

4.2.1. Resonant modes

The background velocities at which the resonant modes occur are predicted by theory in Table 4.1. The analytical solution assumes a stationary flow. In order to compare to theory, simulations with a constant background velocity are performed. The model set-up is the same as the base case except for the velocity at the boundaries, which is constant in time. Mode 1 is the most observed in the field, therefore, a velocity near a theoretical resonant mode 1 response is chosen. To check the ability

of the model to represent higher modes, a near mode 2 and mode 3 response are also simulated. Furthermore, a simulation with a mode between 1 and 2, as well as a simulation with a mode between 2 and 3 are done. In between two resonant modes, the influence of the resonance peak on differences in the magnitude of the vertical velocity is small. Therefore, the amplitudes of the velocity are expected to match well for velocities further away from the resonance peaks. The constant background velocities corresponding to the modes are chosen based on the velocities in Table 4.1.

A theoretical near resonant mode 1 response and the related Taylor Goldstein solutions are shown in Figure 4.2. When comparing the model to the corresponding analytical solution a difference in both vertical velocity magnitude and direction is observed. To obtain a match between the vertical velocity magnitude and mode number, the background velocity used in the Taylor Goldstein equation is chosen slightly higher than the background velocity prescribed at the boundaries of the numerical model. The higher background velocity is chosen by increasing the background velocity by 0.001 m/s until a visual match is obtained between the amplitudes and phases. Due to truncation errors, the background velocity above the bed waves can slightly deviate from the background velocity prescribed at the boundaries. Since the response is near resonant a small deviation in background velocity could lead to large variations in vertical velocity amplitude. Furthermore, the background velocity is slightly higher over the vertical at the top of a bed wave due to a smaller water depth compared to the flat bottom and slightly lower at the trough. The vertical velocity magnitudes do not match when comparing model and theory, Figure 4.2 (a) and (b) respectively. When the background velocity of the analytical solution is increased by 17.5% to 0.47 m/s the model and analytical solution align, Figure 4.2 (a) and (c) respectively. The increase in background velocity of this magnitude cannot be explained by numerical errors.

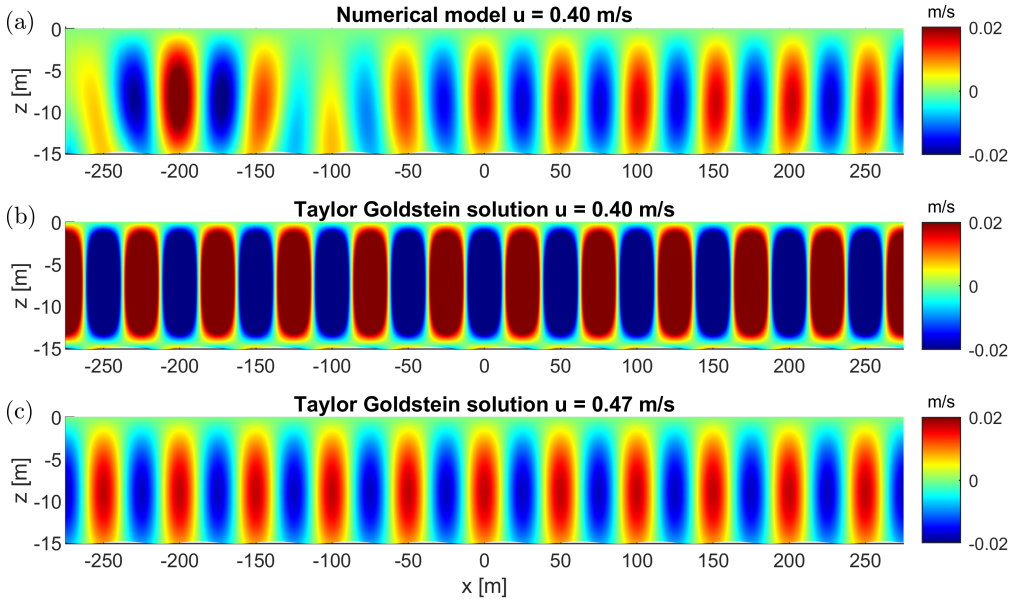

Figure 4.2: Theoretical resonant mode 1 response. Bed waves of amplitude 0.15 m are present over $-275 \leq x \leq 275$ m. The flow is from left to right. (a) The vertical velocity determined using the numerical model for a flow with a constant background velocity of 0.40 m/s and including viscosity. (b) The vertical velocity found using the analytical solution to the Taylor Goldstein equation for a constant velocity of 0.40 m/s. (c) The vertical velocity found using the analytical solution to the Taylor Goldstein equation for a constant velocity of 0.47 m/s.

The near resonant mode 1 response in the model is far from the analytical resonant mode 1 response. The difference between model and theory for mode 2 and 3 is smaller than for the mode 1, 6.8% for mode 2 and 6% for mode 3. For this order of magnitude the deviation could be due to truncation errors, since small deviations in velocity lead to large changes in vertical velocity near the resonance peak. To verify this two constant background velocities away from the resonant peaks are simulated, 0.36 m/s and 0.18 m/s. Away from the resonant peak small deviations in background velocity should result in small deviations in the vertical velocity profile since no steep peaks are present. In this way, it can be determined whether the deviation between model and theory only occurs near the resonance peaks or for all velocities. The simulations of background velocities away from the resonance peaks show a

large difference between model and theory as well. Differences of 17.2% between theory and model for a constant flow of 0.36 m/s and 19.4% for a constant flow of 0.18 m/s are observed. Therefore, the difference between model and theory is not caused by small deviations on the resonance peaks leading to large vertical velocity differences. The detailed results of the simulations of near mode 2 and near mode 3, as well as the simulations between two modes of 0.36 m/s and 0.18 m/s are shown in Appendix C.1.1.

4.2.2. Time scale effect

The resonant response needs time to grow and reach its equilibrium, as shown in Figure 4.3. The vertical velocity amplitude increases from Figure 4.3 (a) until (g). The difference between the velocity amplitudes in Figure 4.3 (g) and (h) is small. Thus, the vertical velocity increases for 1000 seconds, thereafter, the maximum vertical velocity is reached and remains about constant. For higher modes, more time is needed for the resonant response to reach its maximum. For the mode 2 simulation, 1800 seconds were needed to reach the state shown and for the mode 3 simulation 2100 seconds were needed to reach the equilibrium. The higher modes are generated at lower background velocities, which have less momentum. Therefore, more time is needed to reach the maximum vertical velocity for a higher mode.

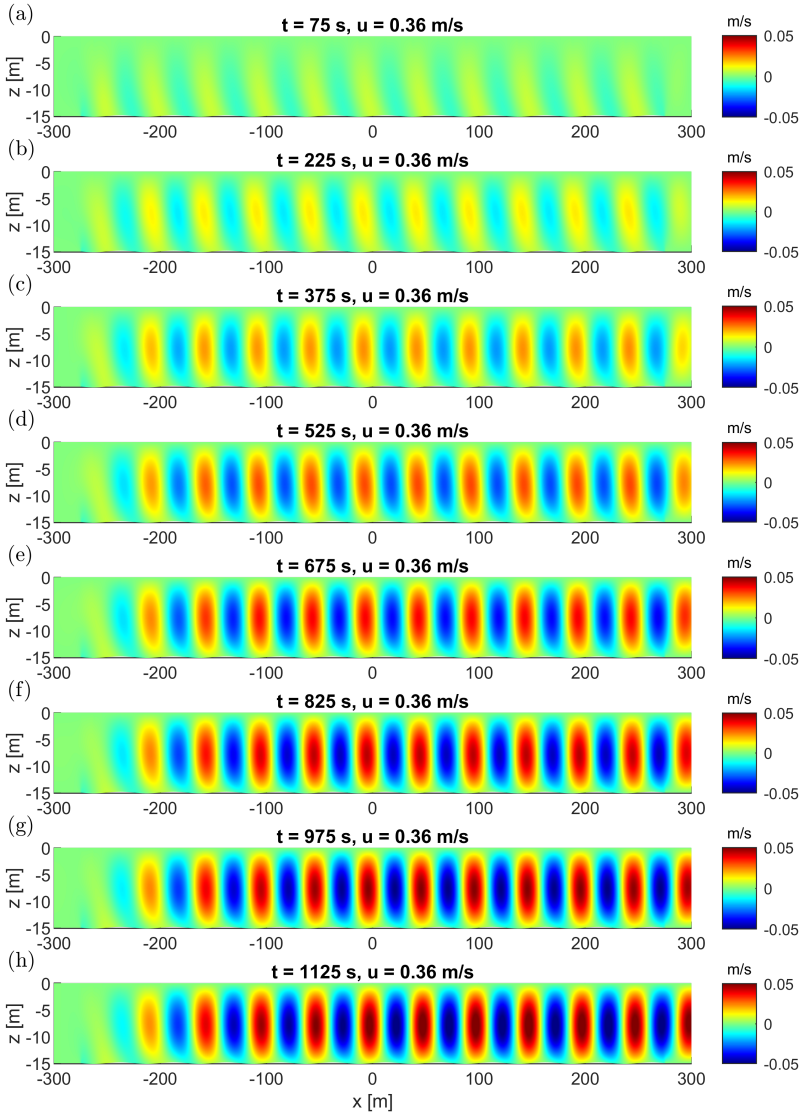

Figure 4.3: Vertical velocity of flow with constant background velocity 0.36 m/s over time using the numerical model. Bed waves of amplitude 0.15 m are present over $-275 \leq x \leq 275$ m. The flow is from left to right.

The time needed for the amplification of the response when the resonance point is passed influences when the resonant responses appear in a decelerating flow. For three different deceleration rates the moment of the maximum mode 1 response is determined. The simulations with different deceleration rates are similar to the base case except the velocity prescribed at the boundaries decreases linearly at deceleration rates of $9.3 \cdot 10^{-5}$, $4.6 \cdot 10^{-5}$ and $5.4 \cdot 10^{-6}$ m/s². The resonant mode 1 response is observed at background velocities of 0.29 m/s, 0.31 m/s and 0.35 m/s respectively. A larger deceleration rate leads to a lower background velocity at which the maximum resonant response is present, due to the time needed for the amplification to grow once the resonant condition is met. The Figures of the different deceleration rates are shown in Appendix C.1.4.

A difference in the time scale effect between a decelerating and accelerating flow is observed. The mode 1 resonant response in a decelerating flow occurs at a velocity 24% below the theoretical velocity at which mode 1 occurs in a stationary flow. In an accelerating flow, the mode 1 response occurs at a velocity that is only 7.5% below the theoretical value. It seems as if in a decelerating flow more time is needed for the resonant response to reach its maximum. Furthermore, the mode 1 response remains in the domain in the case of a decelerating flow and dominates the higher modes. This is not the case in an accelerating flow, since the higher modes are generated first. In the decelerating flow, the flow is subcritical after the resonant mode is generated. In contrast, the flow is supercritical after the resonant mode is generated in an accelerating flow. Therefore, the generated resonant modes remain in the domain longer for a decelerating flow than for an accelerating flow. Thus, the time scale effect is larger in a decelerating flow than in an accelerating flow. The figures and more detailed analysis of the decelerating and accelerating flow can be found in Appendix C.1.2 and C.1.3 respectively.

4.3. Parameter variation

The effect of changing the parameters influencing the generation of internal waves, which are determined in Section 3.1, is investigated by comparing model simulations. To this extent the bottom friction, bed wave amplitude, stratification profile and turbulence model are varied. The figures of the simulations other than the base case can be found in Appendix C.2.

4.3.1. Base Case

The results of the base case are analysed. The internal waves start to appear after 8000 s in the simulation. Before this time the flow remains supercritical. Therefore, the internal waves are present on 28% of the decelerating tide. During the other 72% of the decelerating tide, the amplitude of the internal waves remains small and the additional mixing generated by internal waves will be negligible. The 72% of the decelerating tide in which the flow is supercritical is similar to the theoretical value of 69% found in Subsection 4.1.3. This small difference could be because it is difficult to find the exact moment the internal waves are generated, as the internal wave amplitude is small at the start of the generation.

The results of the base case, for the part of the decelerating flow in which internal waves appear, are shown in Figure 4.4. The internal waves remain above the bed waves and propagate about 100 meters downstream between Figure 4.4 (a) and (f) for the density and between 4.4 (i) and (n) for the vertical velocity. In Figure 4.4 (g) and (h), as well as 4.4 (o) and (p), the internal waves start to propagate upstream of the bed waves. As the resonance conditions for mode 1 are met the amplitude of the internal waves increases, Figure 4.4 (a) and (b) as well as 4.4 (i) and (j), and reaches its maximum around 0.30 m/s, Figure 4.4 (c) and (k), which is a deviation of 26% from the theoretical mode 1 response at 0.406 m/s. The internal waves have a maximum amplitude of about 1 m. Thereafter, the mode 1 response remains in the domain, dominating the higher modes, Figure 4.4 (d) until (h) and 4.4 (l) until (p). A mode 2 response is only visible at the beginning of the bed waves between $x = -250$ m and $x = -150$ m in Figure 4.4 (m) until (p). It is more difficult to observe the mode 2 response at this interval in density Figure 4.4 (e) until (h). Higher modes than the second are not observed.

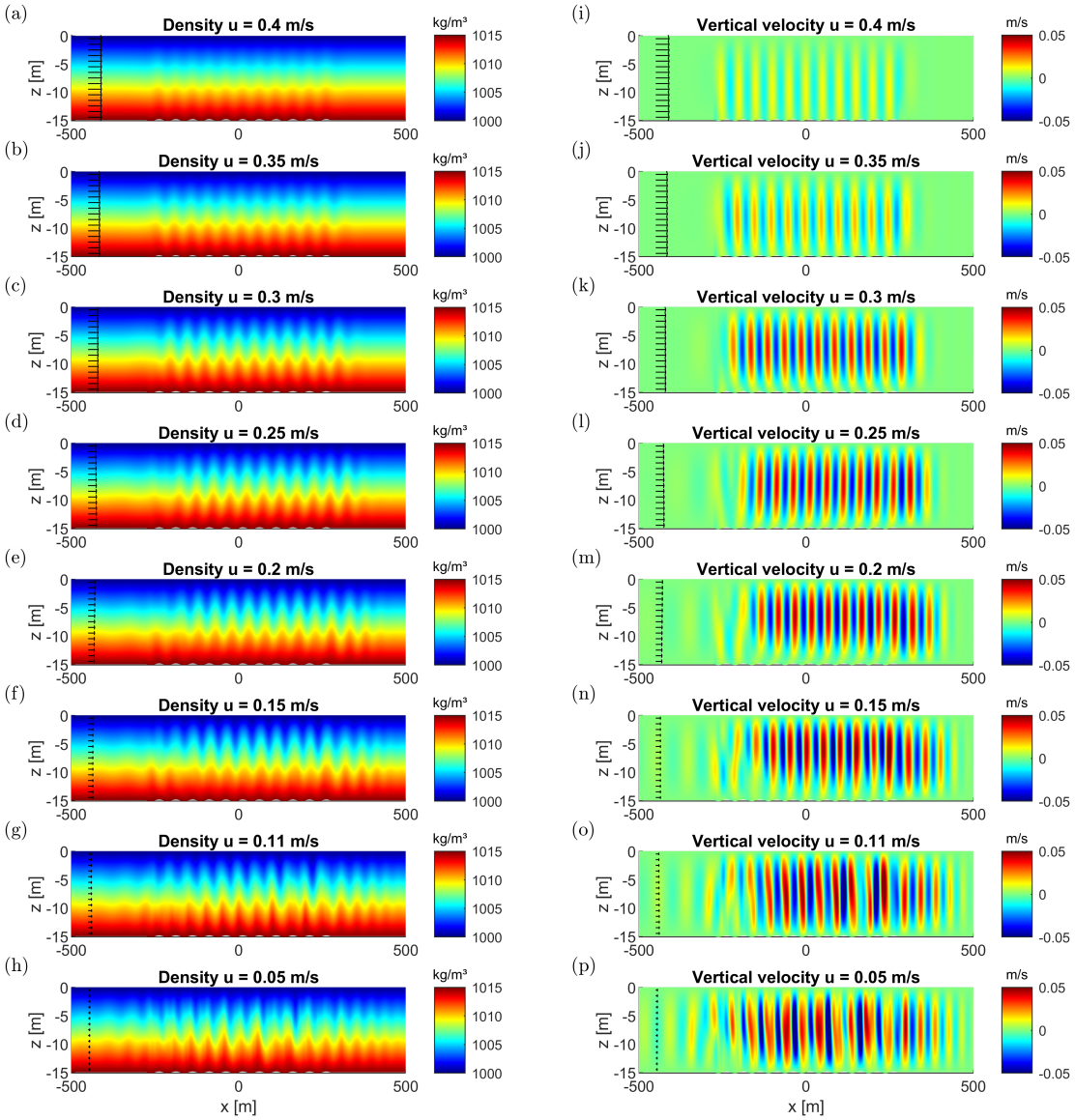

Figure 4.4: Numerical simulation of a decelerating flow from 1 m/s to zero, the base case. Bed waves of amplitude 0.15 m are present over $-275 \leq x \leq 275$ m. The flow is from left to right. Plots (a) until (h) show the density profile and plots (i) until (p) show the vertical velocity.

4.3.2. Bottom friction

The influence of bottom friction is determined, as it is representative of the Rotterdam Waterway. For a simulation including bottom friction, the horizontal velocity shows a logarithmic profile, which is characteristic of a flow including bottom friction. The internal waves have an amplitude of about 0.2 m at the maximum mode 1 response. The amplitude has been reduced by 80% compared to the case without friction. The bottom friction dissipates energy. In the case of no bottom friction, this energy is used for the generation of internal waves. In the simulation including bottom friction, only a mode 1 response is observed. Bottom friction reduces the internal wave amplitude and thereby the potential of the internal waves to mix.

4.3.3. Bed wave amplitude

To determine the effect of bed wave amplitude simulations using higher bed waves of 0.5 m amplitude are performed. This amplitude is also observed in the Rotterdam Waterway. The bed wave amplitude is increased by about 230%, from 0.15 m to 0.5 m. For the simulation without bottom friction and larger bed waves, run #3 of Table 3.3, the internal waves have an amplitude of about 3.5 m. This is an

increase in internal wave amplitude of 250% compared to the simulation with the bed waves of 0.15 m amplitude in the base case. For the simulation with bottom friction and larger bed waves, run #7 of Table 3.3, the internal waves have an amplitude of about 0.4 m. This gives an increase in internal wave amplitude of 100% compared to the simulation with bed waves of 0.15 m amplitude, run #6. An increase in bed wave amplitude results in a larger internal wave amplitude. The relative increase in internal wave amplitude is about equal to the relative increase in bed wave amplitude for the frictionless case. However, the relative increase in internal wave amplitude is smaller than the relative increase in bed wave amplitude for the case including friction. Therefore, the bottom friction reduces the energy available for internal wave generation.

4.3.4. Stratification profile

To determine the effect of stratification on internal wave generation two stratification profiles are considered. Up to now all results were of the linear stratification profile. However, the tangent hyperbolic stratification is a better representation of the Rotterdam Waterway. In a tangent hyperbolic stratified flow, the internal waves are generated in the middle of the vertical, between $z = -10$ and $z = -5$, where the sharp gradient in density is present. For the simulation without bottom friction and bed waves of amplitude 0.15 m, run #9, the observed internal wave amplitude is 1.1 m. This internal wave amplitude is 10% higher than the one observed for a linearly stratified flow, the base case. In a tangent hyperbolic stratified flow, the buoyancy frequency is larger at the sharp density gradient than in a linear stratified flow. Therefore, the resonance condition is satisfied for a higher background velocity for a tangent hyperbolic profile, 0.42 m/s, than for a linear profile, 0.30 m/s. Furthermore, the maximum amplitude of the internal waves in the tangent hyperbolic profile is larger than in the linear profile. For the simulation with bottom friction and bed waves of amplitude 0.5 m, run #8, the internal waves have an amplitude of about 0.5 m. This is 25% higher than for the same simulation with a linear stratified flow. Furthermore, the mode 1 resonance is observed at a 5% higher background velocity than for the linear stratified flow. These increases are in line with the results from the case without friction. Thus, the tangent hyperbolic stratification profile results in a larger internal wave amplitude than the linear stratification profile. However, these larger waves are only present at the sharp density gradient, whereas in the linear profile, these are present over a larger part of the vertical.

4.3.5. Turbulence model

To investigate the influence of the choice of turbulence model, three different turbulence models are considered: LES, $k-\epsilon$ and constant eddy viscosity. For simulations using the small bed wave amplitude of 0.15 m, the internal waves reach their maximum amplitude of 1 m at a background velocity of 0.3 m/s for all three turbulence models. Furthermore, no breaking is observed. For simulations using the larger bed wave amplitude of 0.5 m, the internal waves reach an amplitude of 3.5 m for all turbulence models. The background velocity at which the maximum internal wave amplitude occurs for the LES model is 0.24 m/s. The background velocity at which the maximum internal wave amplitude occurs is 0.25 m/s for the $k-\epsilon$ model and constant eddy viscosity model, which is 4% higher than the LES model. In all simulations, internal wave breaking is observed in the last 1500 seconds of the simulation. Thus, the influence of the turbulence model on the internal wave generation is negligible.

4.4. Summary

In this chapter, the model results are verified by comparison to an analytical solution. Furthermore, the effects of bottom friction, bed wave amplitude, stratification profile and turbulence model on the generation of internal waves are investigated. To obtain an agreement between the analytical solution using the Taylor Goldstein equation and stationary model simulations, the background velocity used in the analytical solution had to be up to 19% higher than the background velocity used in the model simulation. This difference is observed for near-resonant responses, as well as for stationary simulations away from the resonant peaks. Thus, the difference can not be explained by truncation errors in near-resonant solutions. It was discovered the resonant modes need time to reach the maximum amplitude. The time scale needed for the resonance conditions to grow and reach the maximum amplitude is significant compared to the deceleration rate. This explains why the maximum resonant response occurs at a background velocity below the corresponding theoretical value for decelerating flows. Therefore, the model results are considered valid. A difference in internal wave generation between the decelerating

and accelerating tide is observed. On the decelerating tide, the mode 1 response is dominant once it has formed, while the accelerating tide shows higher modes as well. This results in longer periods of mode 1 resonant waves on the decelerating tide than on the accelerating tide and more potential to mix is expected on the decelerating tide. Only during the last 28% of the simulation time internal waves are observed in the simulations, during the rest of the time the flow is supercritical and no internal waves are generated. The results of the parameter variations show bottom friction reduces the internal wave amplitude by 80%. Furthermore, an increase in bed wave amplitude results in an increase of the same order of magnitude of the internal wave amplitude. A tangent hyperbolic stratification profile results in a larger internal wave amplitude than the linear stratification profile. Furthermore, the internal waves are generated at higher background velocity in the tangent hyperbolic stratification than in the linear stratification. Therefore, the internal waves are present in the domain for a larger part of the simulation in the case of a tangent hyperbolic stratification. However, these larger waves are only present at the sharp density gradient, whereas in the linear profile, these are present over a larger part of the vertical. Lastly, the influence of the turbulence model on the internal wave generation was found to be negligible.

5

Quantification irreversible mixing

To quantify the degree of mixing the background potential energy is determined. First, the method to calculate the background potential energy is verified for simplified cases. Thereafter, the background potential energy is analysed for the base case in detail. The influence of bottom friction, bed wave amplitude, stratification profile and turbulence model on the observed mixing is determined. Lastly, the effect of bed wave amplitude on salt intrusion is determined.

5.1. Verification calculation background potential energy

To verify if the method to determine the background potential energy is implemented correctly, the model results are compared to theoretical solutions. This is done for an open and closed system. In both cases, the model results are close to the theoretical solutions. Therefore, the method is implemented correctly.

5.1.1. Lock exchange

To verify if the background potential energy calculated in the control volume is correct, a lock exchange is simulated in a closed basin. In a closed basin, the boundary fluxes are absent and therefore the increase in background potential energy should be clearly visible. The basin used in the simulation of the lock exchange is 200 m long and has a height of 15 m. The grid resolution is 1 m in the horizontal and 0.5 m in the vertical. The simulation is run for 1000 s.

To verify the results quantitatively the potential energy, background potential energy and background potential energy for a fully mixed domain are determined analytically for the initial state and compared to the model results. The density profiles corresponding to the potential energy, background potential energy and background potential energy for a fully mixed domain are shown in Figure 5.1.

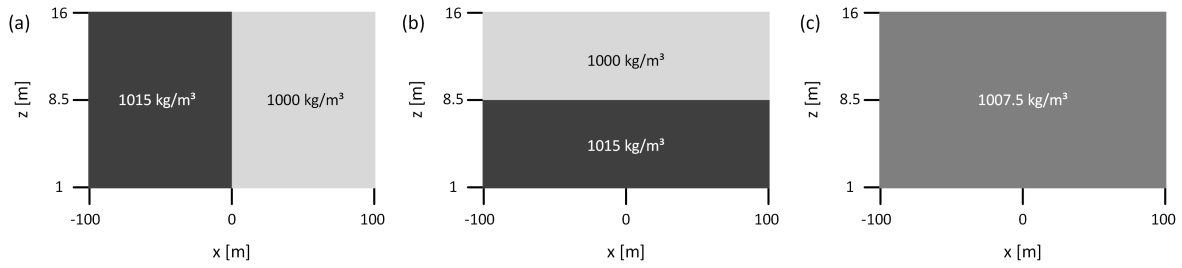

Figure 5.1: Density profile in the initial state of (a) potential energy, (b) background potential energy and (c) background potential energy for a fully mixed domain.

The analytical solution of the potential energy in the initial state is 252,031,163 J/m. In the case of the background potential energy, the analytical solution in the initial state is 251,203,444 J/m. The analytical solution of the background potential energy for a fully mixed domain in the initial state is 252,031,163

J/m. The calculation of these analytical solutions is shown in Appendix D.1.1. The model results for the potential energy, background potential energy and background potential energy for a fully mixed domain in the initial state are 252,040,543 J/m, 251,213,137 J/m and 252,040,496 J/m respectively. The differences between model and theory are 9380 J/m, 9693 J/m and 9333 J/m respectively. The background potential energy needed to fully mix the initial state is the difference between $BPE_{mixed,t0}$ and BPE_{t0}. According to theory, 827,719 J/m background potential energy is needed to fully mix the domain and according to the model 827,359 J/m, which is a deviation of -0.04%. The difference in potential energy, background potential energy and background potential energy for a fully mixed domain between model and theory in the initial state is about 1% of the energy needed to fully mix the domain and therefore small.

The density in the model is not uniform in each horizontal, because once the fluid elements of the heaviest density are all used then a fluid element with a slightly lower density is placed next to it in the horizontal. This situation is visible in the reordered density profile in Figure 5.2 (b), where a small drop is present in the reordered profile around $x = 10$ m. In reality, each fluid element in the non-uniform horizontal layer would change its density profile, resulting in only a density gradient parallel to gravity. This error is reduced by refining the grid. A new simulation uses a grid with a resolution of 0.1 m in both horizontal and vertical direction. The initial and reordered density profile of the finer grid are shown in Figure 5.3. The differences between model and theory in the initial state for the potential energy, background potential energy and background potential energy for a fully mixed domain are 939 J/m, 945 J/m and 939 J/m respectively for the finer grid. This is about 0.1% of the energy needed to fully mix the initial state, which is negligible. Therefore, the method to determine the background potential energy in the control volume works very well.

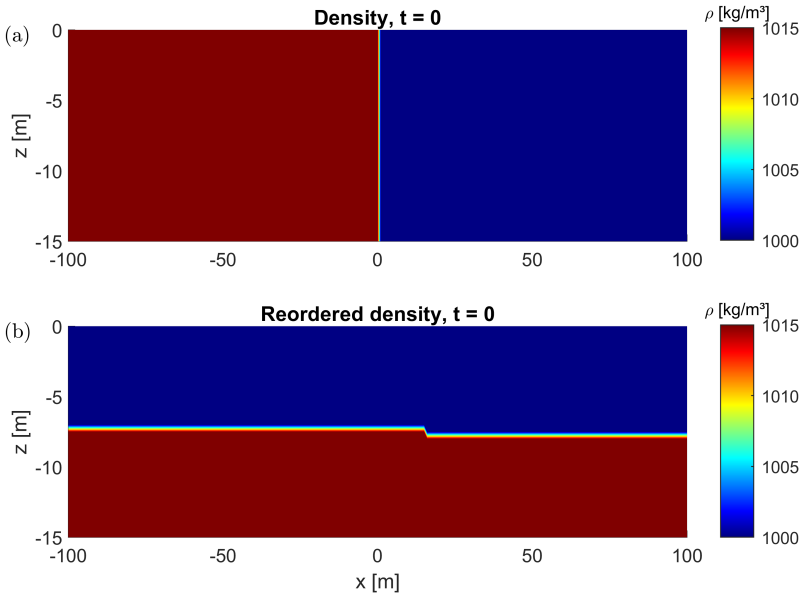

Figure 5.2: (a) Initial density profile and (b) reordered initial density profile for simulation of the lock exchange without bottom friction using a grid of 1x0.5m.

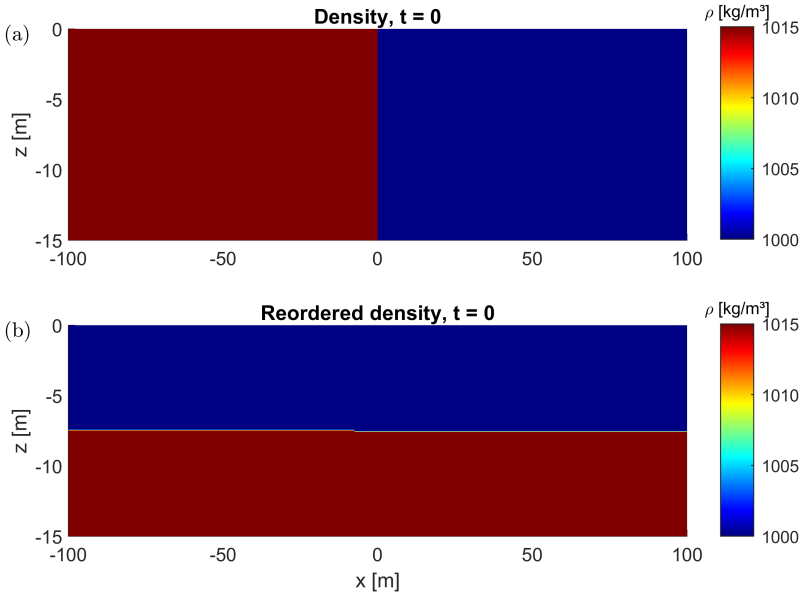

Figure 5.3: (a) Initial density profile and (b) reordered initial density profile for simulation of the lock exchange without bottom friction using a grid of 0.1x0.1m.

To verify the result of the background potential energy method qualitatively the results of the full simulation of the lock exchange are analysed. The background potential energy is shown in Figure 5.4 for each time step. The background potential energy never decreases, which is in line with theory. Furthermore, the potential energy is always above the background potential energy. This agrees with the expectations since the potential energy consists of the background potential and the available potential energy, which are both positive for a closed domain.

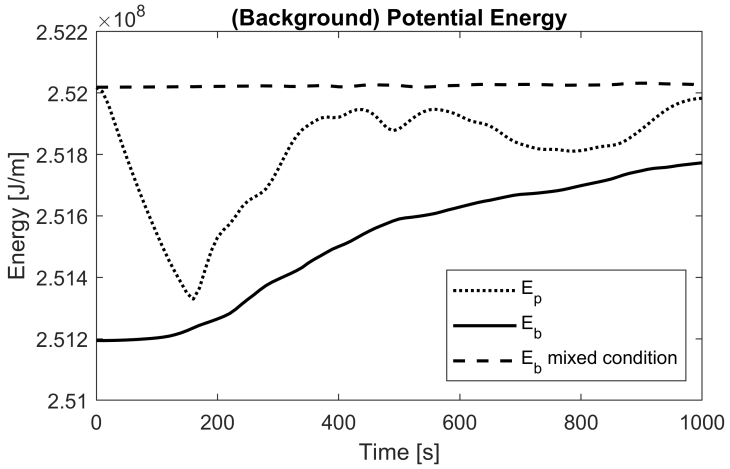

Figure 5.4: Potential energy (PE), background potential energy (BPE) and background potential energy for a fully mixed domain for each time step for a lock exchange.

5.1.2. Constant flow

To verify if the background potential energy fluxes calculated at the boundaries of the control volume are in line with the theoretical solution, a constant flow of 0.3 m/s with a linear stratification is simulated over a flat bed with no bottom friction. The simulation is similar to the base case described in Subsection 3.3.2, except the bottom profile is flat and the velocity prescribed at the boundary is constant in time in this case. The control volume for the calculation of the background potential energy is $-1000 \leq x \leq 1000$ m. For a linearly stratified profile at the boundary, the background potential energy is equal to the potential energy. The background potential energy influx and outflow are equal when no dissipation is

present and the velocity is uniform over the depth since, in theory, the linear stratified profile remains and flows through the control volume at a constant velocity of 0.3 m/s. The linearly stratified density profile is described by $\rho = 1016 - z$ kg/m³. The analytical inflow and outflow of background potential energy is equal to 377,219 J/m/s. The calculation of this value is shown in Appendix D.1.2. The background potential energy fluxes found in the model are shown in Figure 5.5. The differences between inflow and outflow are negligible. At the first few time steps the background potential energy flux is equal to 377,224 J/m/s, which is 0.001% above the theoretical solution. The largest flux observed in the model is an outgoing flux of 377,287 J/m/s at time step 4950 s, which is 0.02% larger than the theoretical solution. Therefore, the boundary flux of background potential energy is determined correctly. The largest difference between in and outgoing flux is 52 J/m/s, which is 0.014% of the theoretical solution. The model includes viscosity. Therefore, the salt is mixed due to diffusion as well. Due to this, the density is different by 0.03 kg/m³ compared to the theoretical profile. Furthermore, close to the bottom and rigid-lid the velocity deviates slightly from the prescribed 0.3 m/s. These effects result in a small difference between theory and model, as well as a difference between incoming and outgoing flux in the model simulation. The production of background potential energy in the control volume is determined using Equation 3.13 and equal to about 50 J/m/s. Therefore, production of this order magnitude is not produced by internal waves, but by diffusion.

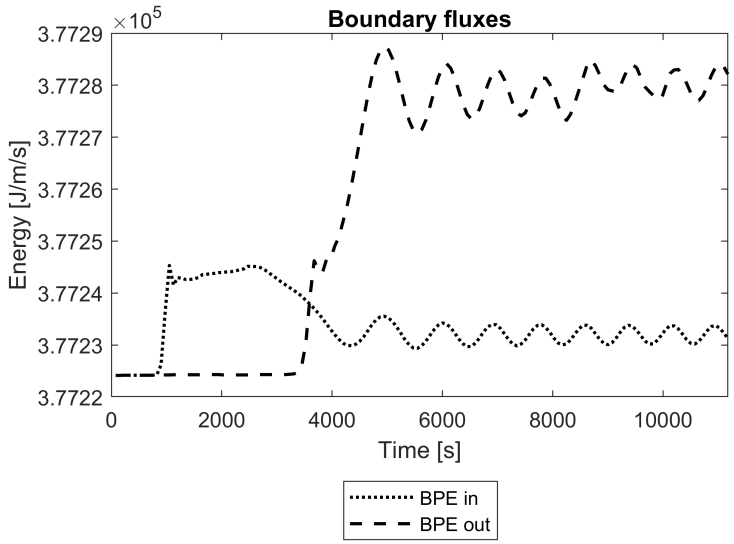

Figure 5.5: Background potential energy flux at the boundaries of the control volume ($x = -1000$ and $x = 1000$) for a simulation using a linearly stratified density profile, flat bottom, no bottom friction and constant background velocity of 0.3 m/s.

5.2. Decelerating flow

The mixing in simulations of decelerating flow is analysed by determining the background potential energy. In this way, the possibility to determine the mixing of a decelerating flow using the background potential energy is investigated. Furthermore, the influence of the turbulence model and bottom friction on the mixing observed are determined.

5.2.1. Base case

The potential energy and background potential energy are calculated in the control volume at each time step. The increase in energy compared to the initial state is determined relative to the energy needed to mix the initial state fully. The results of the base case, Table 3.3 run #0, are shown in Figure 5.6. The potential energy and the background potential energy are equal to each other until the internal waves are generated at 8000 s. Thereafter, the potential energy is larger than the background potential energy, since the internal waves generate available potential energy. From 8000 s onwards, the potential energy and background potential energy deviate from the results of the flat bed, results of the flat bed are shown in Appendix D.2. The potential energy and background potential energy increase due to the internal waves generated by the bed waves, whereas for the flat bed, no internal waves are present. The internal waves reach their maximum amplitude at 9000 s. Thereafter, these mode 1

internal waves remain in the domain, causing a sharper increase in background potential energy from 9000 s onwards.

The increase in background potential energy is small compared to the energy needed to fully mix the control volume. The increase in background potential energy is approximately 0.6% of the energy needed to mix the control volume fully. Compared to the flat bed, where the background potential energy increased with 0.1% of the energy needed to completely mix the control volume, the absolute increase in background potential energy due to the internal waves is 0.5% of the energy needed to mix the control volume fully.

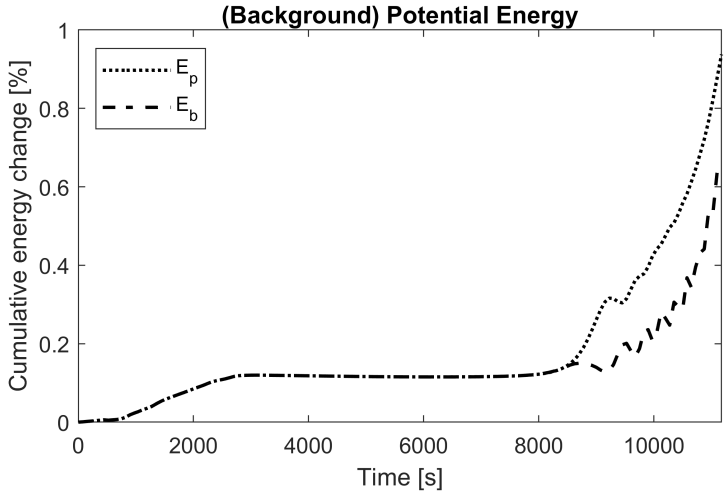

Figure 5.6: The change in potential energy (E_p) and background potential energy (E_b) compared to the initial state relative to the energy needed to reach a fully mixed control volume is plotted for each time step for the base case simulation: no bottom friction, viscosity and bed waves of amplitude 0.15 m.

The boundary flux of the background potential energy is determined since background potential energy can leave the control volume through the open boundaries. Using the boundary flux and the change of BPE in the control volume, the BPE production is determined by Equation 3.13. The individual terms of Equation 3.13 are determined relative to the energy needed to fully mix the initial state. The results for the base case are plotted in Figure 5.7. The fluctuations visible in the plot for $t \leq 3000$ are caused by spin-up effects due to waves reflecting of the topography. In all simulations, these fluctuations occur around the same time. The spin-up effects have disappeared after 3000 seconds. The change in background potential energy, E_b, is negligible compared to the boundary flux, $E_{b,flux}$. Therefore, the background potential energy production is approximately opposite to the boundary flux, $E_{b,flux} \approx -E_{b,prod}$. After 9500 s the boundary flux starts to show a more oscillatory behaviour. This causes a drop in the background potential energy production between 9500 s and 10500 s. However, the production of background potential energy should be irreversible. Negative production is not possible or indicates counter-gradient mixing, which is not expected to happen in the flow situation of the base case. After 9500 s the velocity fluctuations caused by the internal waves start to propagate through the boundaries of the control volume. The fluctuations in cumulative boundary flux indicate changes in the horizontal velocity profile or density profile at the boundary. This is caused by small internal waves passing through the boundaries which disrupt the background potential energy fluxes. Therefore, the energy balance is disrupted, since the available potential energy is then also included in the background potential energy boundary flux. Thus, the background potential energy production, which includes the boundary fluxes cannot be quantified when the internal waves propagate through the boundaries of the control volume.

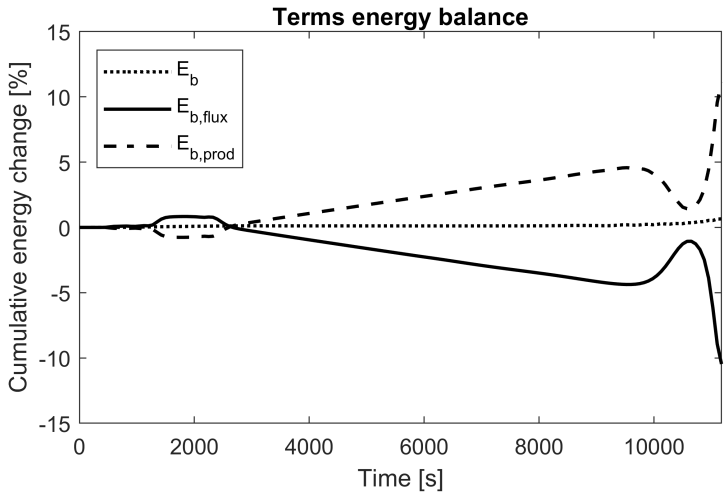

Figure 5.7: Absolute change in background potential energy, boundary flux of background potential energy and potential energy production for the base case simulation.

5.2.2. Bottom friction

To achieve a more accurate representation of the Rotterdam Waterway, the impact of bottom friction is accounted for. The cumulative change in background potential energy in the control volume compared to the energy needed to fully mix the control volume is shown for a simulation including bottom friction in Figure 5.8. At all time steps the background potential energy is approximately equal to the potential energy. Therefore, the available potential energy is zero, indicating the internal waves in the domain do not generate additional mixing. The background potential energy decreases in the first 3800 s. This decrease is caused by spin-up effects caused by the bottom friction. A decrease in background potential energy can only be caused by boundary fluxes since the BPE represents irreversibly mixing. Once it is generated the BPE cannot be transferred back to available potential energy. The cumulative boundary flux of BPE ($E_{b,flux}$) is shown in Figure 5.9, as well as the cumulative production of BPE ($E_{b,prod}$) and the cumulative change of BPE (E_b). The boundary flux is dominant over the change in BPE. However, the BPE flux is positive, meaning BPE is imported into the domain. Therefore, the production of BPE is negative. This is not in line with the expected positive value of the BPE production, since it represents irreversible mixing.

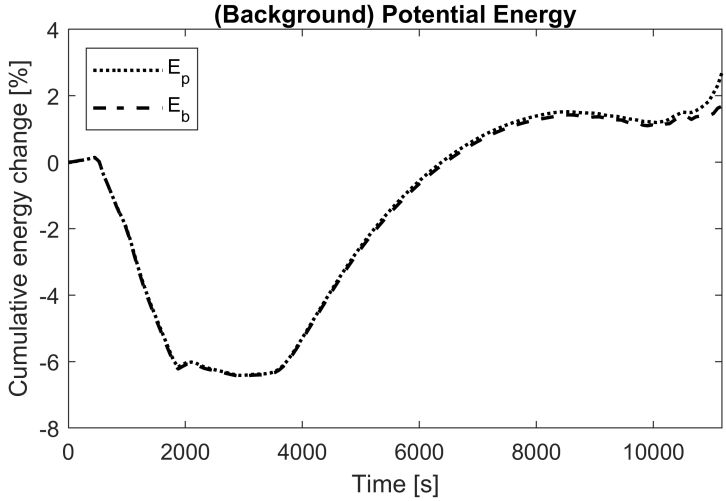

Figure 5.8: Simulation of a decelerating flow with bed waves of amplitude 0.5 m and bottom friction. The cumulative change in potential energy (E_p) and background potential energy (E_b) compared to the initial state relative to the energy needed to reach a fully mixed control volume.

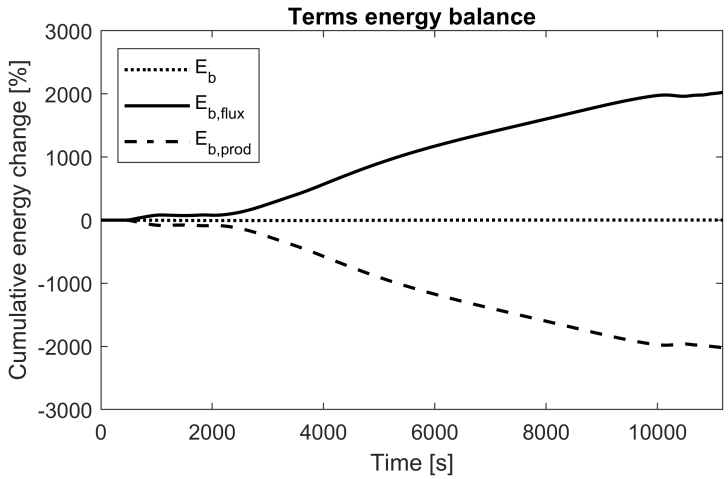

Figure 5.9: Simulation of a decelerating flow with bed waves of amplitude 0.5 m and bottom friction. Absolute change in background potential energy, boundary flux of background potential energy and potential energy production for the base case simulation relative to the energy needed to fully mix the initial state of the control volume.

To determine the reason for the negative production, the BPE boundary fluxes are further investigated. The depth-averaged density and horizontal velocity at the inflow and outflow of the control volume are similar. However, when comparing the depth-dependent density and horizontal velocity profiles, differences are observed. The horizontal velocity profile over the vertical for the inflow and outflow of the control volume at 6750 s is shown in Figure 5.10. The horizontal velocity profile of the outflow is slightly larger than the inflow until 8 m above the bed. From 8 m above the bed until the surface the horizontal velocity of the inflow is larger than the outflow. Near the surface, the horizontal velocity is 0.05 m/s higher at the inflow than the outflow. The density profile over the vertical for the inflow and outflow of the control volume at 6750 s is shown in Figure 5.11. The density profile over the vertical is similar for the inflow and outflow of the control volume from 3 m above the bed until the surface. Between 0 to 3 m above the bed, the density profile of the outflow drops 1 kg/m³ below the density profile of the inflow. The potential energy increases with the z-coordinate. Therefore, changes to the density or horizontal velocity near the surface have the largest influence on the background potential energy. The difference in horizontal velocity profile between the inflow and outflow of the control volume is the largest near the surface. This has a larger impact on the background potential energy flux than the difference in density near the bottom.

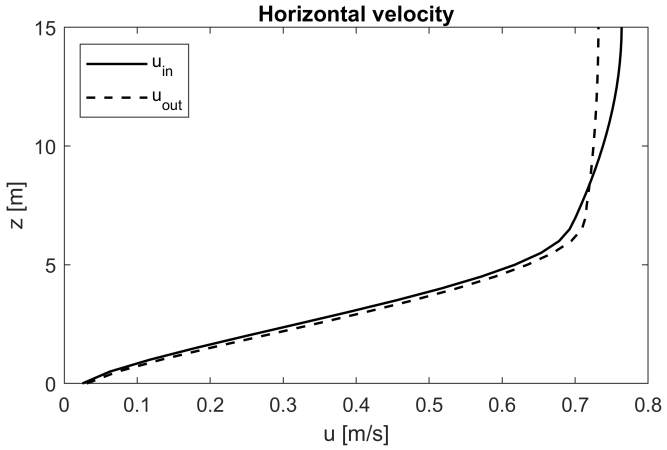

Figure 5.10: Horizontal velocity profile at the inflow $x = -1000$ and outflow $x = 1000$ of the control volume.

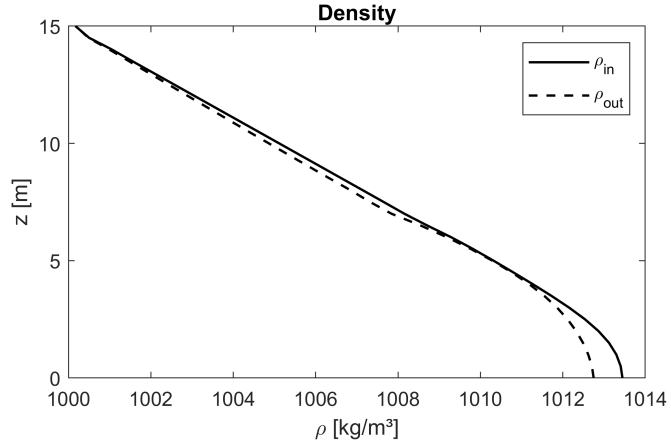

Figure 5.11: Vertical density profile at the inflow $x = -1000$ and outflow $x = 1000$ of the control volume.

To reduce mixing near the bottom a simulation with a tangent hyperbolic profile is done. In this case, the fluid is well mixed near the bottom. Therefore, the mixing due to bottom friction should be smaller. However, the results of a decelerating flow with a tangent hyperbolic stratification and including bottom friction also show a negative production for most of the simulation time. The negative background potential energy production is smaller for the tangent hyperbolic stratification than for the linearly stratified profile. Therefore, the mixed profile near the bottom worked as expected. However, the change in stratification does not change the difference in horizontal velocity profile between the left and right side of the control volume. Therefore, the background potential energy production in the domain cannot be quantified well, since the boundary fluxes are difficult to quantify and these dominate the background potential energy production in the control volume.

5.2.3. Bed wave amplitude

To determine the effect of bed wave amplitude simulations using higher bed waves of 0.5 m amplitude are performed. This amplitude is also observed in the Rotterdam Waterway. The cumulative background potential energy in the control volume is plotted as a percentage of the background potential energy required to fully mix the control volume in Figure 5.12. The available potential energy is larger for the larger bed waves. The internal waves have a larger amplitude due to the larger bed waves. The larger internal wave amplitude results in a higher potential energy. The background potential energy has also increased due to the larger bed waves, but less than the potential energy. Therefore, the potential to mix increases, resulting in a larger available potential energy. The increase in background potential energy is approximately 2.7% of the energy needed to mix the control volume fully. Compared to the results of the bed wave amplitude 0.15 m, the increase in background potential energy due to the larger bed waves is 2.1% of the energy required to mix the control volume fully.

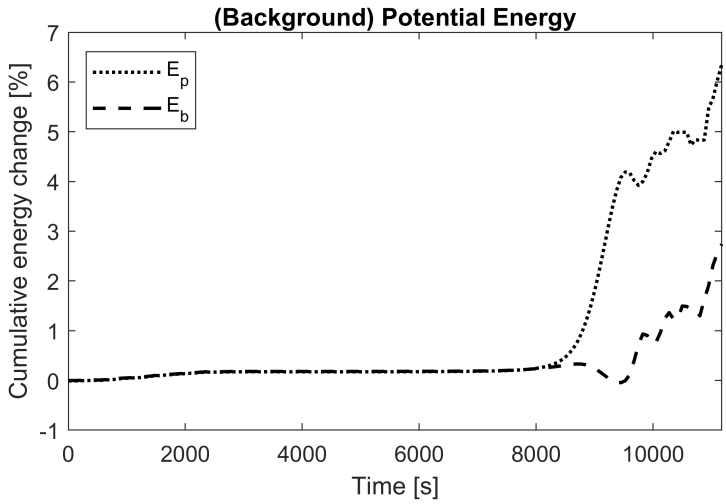

Figure 5.12: The change in potential energy (E_p) and background potential energy (E_b) compared to the initial state relative to the energy needed to reach a fully mixed control volume. Simulation of a decelerating flow with a linear stratification, bed waves of amplitude 0.5 m and no bottom friction.

5.2.4. Stratification profile

To better resemble the Rotterdam Waterway, tangent hyperbolic stratification is considered instead of linear stratification. The cumulative background potential energy in the control volume is plotted as a percentage of the background potential energy required to fully mix the control volume in Figure 5.13. The increase in background potential energy is 2.5% of the energy required to mix the control volume fully. This is 1.8% of the energy needed to fully mix the control volume more than for the linear stratification, there the background potential energy increased by 0.7% of the energy required for a fully mixed control volume. Therefore, the observed mixing for the tangent stratification is larger than for the linear stratification. However, in both cases the increase in background potential energy remains small, only a few percent of the energy needed to mix the control volume completely. The difference observed between the linear and tangent hyperbolic stratification can be explained by different phenomena. The internal waves are generated at higher background velocities in a tangent hyperbolic stratification compared to a linear one. Therefore, the internal waves are present for a longer period for the tangent hyperbolic, resulting in slightly more mixing. Furthermore, the density gradient is sharper in the tangent hyperbolic stratification, which can cause additional mixing until the gradient becomes too large and acts as a strong restoring force. Lastly, the internal wave amplitude is larger for the tangent hyperbolic stratification, resulting in more mixing. However, the internal waves are only present at the sharp density gradient for the tangent hyperbolic stratification profile, whereas, for the linear stratification, the internal waves are present over almost the entire vertical.

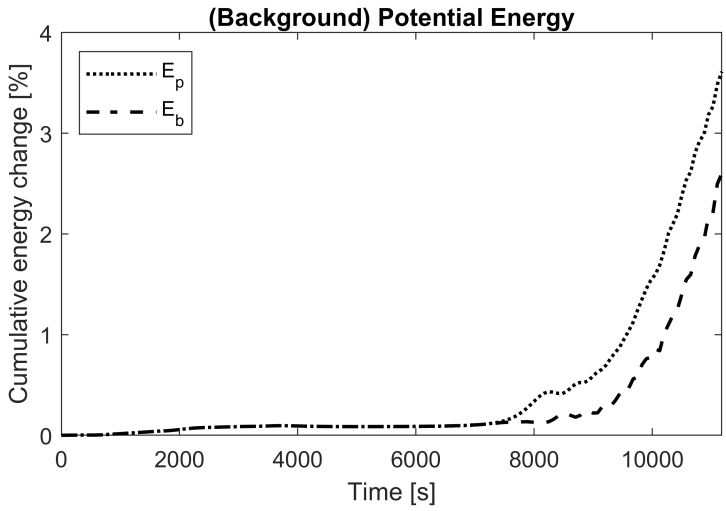

Figure 5.13: The change in potential energy (E_p) and background potential energy (E_b) compared to the initial state relative to the energy needed to reach a fully mixed control volume. Simulation of a decelerating flow with a tangent hyperbolic stratification, bed waves of amplitude 0.15 m and no bottom friction.

5.2.5. Turbulence model

To investigate the influence of the choice of turbulence model, three different turbulence models are considered: LES, $k-\epsilon$ and constant eddy viscosity. The results of simulations with bed waves of amplitude 0.15 m are depicted in Appendix D.3. The mixing observed is negligible. Therefore, no clear distinction between the turbulence models is observed. To observe the influence of the turbulence models on internal wave breaking, simulations using a bed wave amplitude of 0.5 m are analysed. The cumulative background potential energy in the control volume is plotted as a percentage of the background potential energy needed to fully mix the control volume for the simulation with bed waves of 0.5 m amplitude in Figure 5.14. For the larger bed waves, the background potential energy follows a similar pattern for all three turbulence models. Once the internal waves are generated after 8000 s, the LES results slightly deviate from the other two turbulence closure models. However, the difference between the three models remains small, at a maximum of approximately 0.4% of the energy needed to mix the control volume fully. Furthermore, the breaking of the internal waves starts around 10,000 s for all three models and shows similar behaviour, which explains the similar results observed for all three models. Therefore, the effect of the turbulence model on the calculated background potential energy is small.

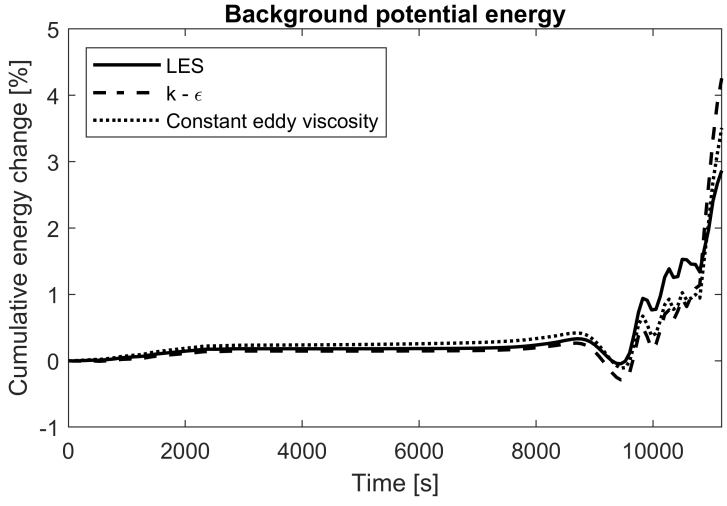

Figure 5.14: The cumulative change in background potential energy (E_b) compared to the initial state relative to the energy needed to reach a fully mixed control volume for three different turbulence models. Simulation of a decelerating flow with bed waves of amplitude 0.5 m and no bottom friction.

5.3. Salt imported by estuarine circulation

To determine the change in salt imported by estuarine circulation the squared buoyancy frequency of the background state is analysed over time, based on the relation found in Equation 3.15. The reduced salt imported by estuarine circulation due to bed waves is determined for the base case. Furthermore, the influence of bed wave amplitude on the salt intrusion reduction is determined. The squared buoyancy frequency over time for three different simulations is plotted in Appendix D.4.

First, the change in buoyancy frequency for the simulation with flat bottom and linear stratification is determined, simulation #10 of Table 3.3. This is the reference value for the simulations including bed waves. The buoyancy frequency of the background state decreased by 2.45% compared to the initial value for the simulation with flat bottom. Spin-up effects cause this decrease.

In the simulation including the bed waves of amplitude 0.15 m, simulation #0 of Table 3.3, the buoyancy frequency of the background state decreased by 3.15% of the initial value. Therefore, the bed waves result in a decrease of the buoyancy frequency of 0.70% compared to the flat bed. The squared buoyancy frequency is proportional to the salt imported by estuarine circulation, as depicted in Equation 3.15. Thus, the salt imported due to estuarine circulation is reduced by 0.7% due to the bed waves of 0.15 m.

In the simulation including the bed waves of amplitude 0.5 m, simulation #3 of Table 3.3, the buoyancy frequency of the background state decreased by 4.21% of the initial value. Therefore, the bed waves of amplitude 0.5 m decrease the buoyancy frequency by 1.76% compared to the flat bed. The squared buoyancy frequency is proportional to the salt imported by estuarine circulation. Thus, the salt imported due to estuarine circulation is reduced by 1.76% due to the bed waves of 0.5 m.

In Subsection 4.3.3 it was determined that the internal wave amplitude increases when the bed wave amplitude increases. The internal waves of larger amplitude result in more irreversible mixing, which results in a larger decrease in buoyancy frequency. Therefore, the increased bed wave amplitude results in a reduction of salt intrusion.

5.4. Summary

The calculation of background potential energy was verified by analytical solutions of a closed domain and steady-state open domain. The results are in line with the theoretical expectations. Therefore, the method is implemented correctly. However, if internal waves propagate through the boundaries of the control volume, the boundary flux of background potential energy shows large fluctuations. Differences between the horizontal velocity profile at the inflow and outflow are observed, as well as in the density profiles. Therefore, the background potential energy flux cannot be quantified correctly by Equation 3.11. So additional terms might need to be added in the flux term or it could be that the background potential energy cannot be quantified as a flux term, since in the case of the flux the background potential energy is calculated over a vertical instead of an area. Simulations using the different turbulence models LES, $k-\epsilon$ and constant eddy viscosity show similar results. Thus, the influence of the turbulence model on the observed mixing is small. The tangent hyperbolic profile results in slightly more mixing than the linear profile, the background potential energy increased with 1.8% of the energy required for a fully mixed control volume. The mixing caused by bottom friction and the development of the logarithmic profile are dominant over mixing generated by internal waves, since no available potential energy is observed in the simulation including bottom friction. Therefore, the question arises whether the background potential energy is the right method to quantify irreversible mixing by internal waves in the case of bottom friction, as the bottom friction seems to dominate the mixing results. The additional mixing created by the presence of bed waves, which generate internal waves, is expressed in a reduction of salt intrusion. An increase in bed wave amplitude of 230% results in an increase of internal wave amplitude of the same magnitude and a decrease in salt intrusion of 1% relative to the initial situation if the bed waves are present in 27.5% of the domain.

6

Discussion

6.1. Model assumptions

Only a small part of the estuary is simulated in the model. The model is used to represent the processes related to salt intrusion in an estuary, based on the characteristics of the Rotterdam Waterway. The flow simulated in the small part of the estuary is assumed to be representative of the entire estuary. In reality, different forcing mechanisms dominate salt intrusion in various parts of the estuary (Dijkstra et al., 2022). Furthermore, the stratification profile differs along the estuary.

At the boundaries of the domain, a constant velocity is prescribed. For the cases without bottom friction, the velocity is uniform over the depth and decreases using a M2-tide. Tidal asymmetry is not considered in the model. The internal tidal asymmetry in the Rotterdam Waterway is negligible (de Nijs et al., 2011). However, the velocity forcing at the mouth of the estuary does show a difference between ebb and flood velocity and period (de Nijs et al., 2011). Therefore, the external tidal forcing is not a perfect cosine, which is used in the simulations. For the cases including bottom friction, the velocity profile is logarithmic over the depth, which is more in line with the Rotterdam Waterway. The case including bottom friction is therefore a better representation of reality. Besides velocity, the stratification is prescribed at the boundaries. The sponge layer needs a reference stratification which is prescribed at the boundary. In reality, the stratification profile is not the same at the two ends of the domain if mixing occurs.

At the top boundary of the domain, a rigid-lid is applied. In this way, the effects of surface waves are eliminated. A surface wave propagating through the domain disturbs the velocity signals, which makes it difficult to differentiate between the internal wave effect and the surface wave effect. Therefore, the internal wave effects are isolated by the rigid-lid. However, this might overestimate the internal wave energy slightly, since the surface waves can dissipate part of the internal wave energy. The effect could also be the opposite in which the surface waves add energy to the internal waves. Internal waves are then generated due to wind forcing (Bergh & Berntsen, 2009). Furthermore, wind forcing mixes the stratification near the surface. This effect is taken into account by using the tangent hyperbolic stratification.

The water depth is assumed to be constant in the simulations and all bed waves are assumed to be identical. In reality, the water depth varies and the bed waves span a variety of lengths and heights. Therefore, in reality, internal waves of different wavelengths are generated at different background velocities. This results in the generation of internal waves of a wide variation of frequencies and wavelengths. The different wavelengths cause the internal waves to reach their resonance conditions at a variety of background velocities. Therefore, internal waves are in reality generated over a larger part of the decelerating tide, which results in more mixing than observed in the model simulations.

The relation between salt imported by estuarine circulation and squared buoyancy frequency, depicted in Equation 3.15, is based on the relation between vertical eddy diffusivity and buoyancy frequency found by Osborn (1980), equation 2.3. The relation of Osborn (1980) is developed for oceans. The buoyancy flux is determined as a local variable. Therefore, the related vertical eddy diffusivity is also

locally determined. Therefore, a single value for the entire domain can only be obtained when the local buoyancy flux is approximately the same everywhere in the domain. The buoyancy frequency is independent of depth for a linear stratification. Moreover, in the background state the the buoyancy frequency is independent of the horizontal position. Therefore, the proportionality found in Equation 3.15 can be applied for a linear stratification.

6.2. Internal wave generation

The results of the generation of internal waves are discussed and compared to earlier research. Furthermore, the time scale effect of the resonant modes found is discussed, as well as the part of the tidal cycle during which internal waves are generated. Lastly, the effect of a tangent hyperbolic stratification is discussed.

6.2.1. Resonant modes

In Subsection 4.2.1, a difference between model and theory was observed for stationary simulations. The model results correspond to an analytical solution with a higher background velocity compared to the model input. It was considered that near the resonant point, small deviations in background velocity result in large deviations in the vertical velocity profile, due to the steep resonance peaks. However, also velocities away from the resonance peak show a difference in the background velocity of around 19% compared to the theoretical solutions. In Labeur (2009) a model similar to FINEL was used to simulate the stationary modes and the model results align with the theoretical result of the Taylor Goldstein equation. The settings used in this research are slightly different from Labeur (2009). In this research, the density difference over the vertical is higher, the horizontal grid size is finer, the amount of bed waves is larger and the turbulence closure is done by large eddy simulation instead of constant eddy viscosity. However, these differences are not expected to lead to the large difference between the results of this research and the results of Labeur (2009). More research is needed to explore the reason for the difference in results of this study and the theoretical solution, as well as the results of Labeur (2009). This can be done by a detailed analysis of any other differences in input parameters, such as the time integration. Furthermore, changes made to the FINEL model can be compared to the model described in Labeur (2009) and see whether these differences could impact the result significantly, in order to create the large difference between model and theory observed.

In the decelerating flow shown in Subsection 4.2.1, the background velocity at which the resonant mode 1 response was observed in the model was 24% lower than the stationary theoretical solution. Furthermore, no clear mode 2 response was observed. Numerical simulations of internal waves using a similar version of the model resulted in a difference of 3% between the model and theoretical resonant mode 1 response in Labeur and Pietrzak (2004) and Pietrzak and Labeur (2004). No clear mode 2 response is observed in Labeur and Pietrzak (2004) and the maximum mode 2 response in Pietrzak and Labeur (2004) is observed at a background velocity 27% below the theoretical value. The small difference between theory and model observed for mode 1 resonance is explained by non-negligible non-linear effects due to a high internal wave amplitude to water depth ratio by Pietrzak and Labeur (2004). These non-linear effects are not included in the Taylor Goldstein equation. The difference in mode 2 response between theory and model is caused by time scale effects (Labeur & Pietrzak, 2004).

6.2.2. Time scale effect

The resonant mode 1 responses observed for the different deceleration rates in Subsection 4.2.2 occur at lower background velocities than the theoretical value predicted in Table 4.1. However, for a smaller deceleration rate, the solution comes closer to the theoretical solution. The time scale needed for the resonance conditions to grow and reach the maximum is significant compared to the deceleration rate. Therefore, the background velocity in the decelerating flows simulated has decreased before the resonant response reaches the maximum amplitude. This time scale effect explains why the resonant mode 1 response observed in the model was 24% lower than the stationary theoretical solution. However, the time scale effect is not observed for mode 1 in the results of Labeur and Pietrzak (2004). The difference is caused by different model settings related to the time dependence of the model. However, which settings these are is to be determined in future research.

6.2.3. Propagation of internal waves

In a deceleration flow, the time dependence of the response is important (Labeur & Pietrzak, 2004). The time-dependent background velocity in a decelerating flow causes the internal waves to propagate after generation. During a mode, the internal waves are trapped to the topography and the wave speed is determined by the background velocity at the time of the trapping. Once the flow decelerates further the internal waves are freed and propagate away from the bed. Since the flow decelerates the background velocity is smaller than the wave speed and therefore the internal waves are expected to travel upstream. The mode 1 internal waves would travel upstream in the domain after formation. When propagating slowly upstream over the bed waves the mode 1 internal waves dominate the higher modes formed. In an accelerating flow, the higher modes are generated first and are not disturbed by the lower modes. This explains why the mode 2 response was only observed in small parts of the domain for a decelerating flow and higher modes were not visible, whereas these were visible in an accelerating flow.

In Pietrzak and Labeur (2004) upstream propagating internal waves are observed at the lower velocities of the decelerating tide. The same was observed in the results of this thesis. The small downstream propagation of internal waves observed in the base case of this thesis is also visible in the results of Labeur and Pietrzak (2004). In Figure 3 of Labeur and Pietrzak (2004) the mode 1 internal waves propagate about 75 m downstream before starting to propagate upstream. Therefore, the propagation of the mode 1 internal waves is similar to earlier research. The reason for the downstream propagation could be non-linear effects. To determine whether that is the case the results of an analytical solution including the non-sinusoidal shape of the waves can be considered. The internal wave velocity should then be determined analytically based on the size of the bed waves and the background velocity. The resulting internal wave velocity should give more insight into the influence of the included non-linear effect on the downstream propagation.

6.2.4. Generation of internal waves during tidal cycle

From theory, it was determined that internal waves are formed when the flow is subcritical. The flow is theoretically subcritical for 31% of the decelerating tide. Once the flow is subcritical the internal waves need time to develop and amplify when the resonance condition is met. During 28% of the decelerating tide, internal waves are observed in the simulations, during the rest of the time the flow is supercritical and no additional mixing is observed. A similar pattern is observed for the background potential energy in the control volume. The background potential energy remains constant until the last 25% of the simulation. Thereafter, the background potential energy starts to increase due to internal wave activity. Therefore, the generation of internal waves is only effective during a quarter of the decelerating tide. However, the mixing created is irreversible and contributes to the reduction of salt intrusion during the remainder of the tidal cycle. Therefore, the found reduction in salt intrusion is the minimum value that could be observed during a full tidal cycle, since irreversible mixing is also generated during the accelerating tide. The mixing during the accelerating tide is expected to be smaller than for the decelerating tide, as during the accelerating tide the resonant mode 1 response is present in the domain for a shorter period than for the decelerating tide. To determine the exact value of additional mixing by internal waves over a tidal cycle further research including simulations of a complete tidal cycle is recommended.

6.2.5. Stratification profile

Earlier research on internal wave generation, as well as analytical solutions, are all based on linear stratification. In this research, a tangent hyperbolic stratification is considered besides the linear stratification, since a tangent hyperbolic stratification is a better representation of the Rotterdam Waterway. In Subsection 4.3.4 it was determined that in the simulations without bottom friction, the amplitude of the internal waves is 10% larger for a tangent hyperbolic stratification than for a linear stratification and in the simulations including bottom friction the amplitude of the internal waves is 25% larger. Furthermore, the resonant mode 1 response is reached at a background velocity 40% higher than the background velocity at which the resonant mode 1 response appears in a linear stratification. Therefore, the internal waves are present for a longer period in the tangent hyperbolic stratification than in the linear stratification. The internal waves mix the fluid for a longer period and have larger amplitudes in a tangent hyperbolic stratification. Therefore, the tangent hyperbolic stratification results in an increase of

the background potential energy of 1.8% of the energy required to mix the control volume completely, compared to the linear stratification.

6.3. Evaluation quantification irreversible mixing

The concept of background potential energy works very well for closed systems, as seen in the lock exchange example in Subsection 5.1.1. However, for a bounded domain in an open system, it is difficult to determine the boundary flux because internal waves can pass through this boundary. Moreover, if bottom friction is included, the development of the logarithmic velocity profile has a large influence on the boundary fluxes and the resulting background potential energy production.

6.3.1. Closed system

The background potential energy can easily be determined in a closed system, as described in Subsection 5.1.1. The results correspond both qualitatively and quantitatively to the theoretical expectations. The background potential energy increases for each time step in the lock exchange. These results align quantitatively with the continuously increasing background potential energy theoretically determined in Winters et al. (1995) and shown in the results of Lamb and Nguyen (2009).

6.3.2. Boundary flux

When an open system is considered, a boundary flux of background potential energy is present. The boundary flux of background potential energy has not been quantified before. Lamb (2007) uses the initial undisturbed density as the reference state to determine the background potential energy, which is then independent of time. This method is not applicable to determine irreversible mixing, since the change in background potential energy is of interest to quantify irreversible mixing.

If no overturning is present at the boundaries of the control volume, the density profile at the boundary is already in a state of minimum potential energy. Therefore, no reordering is needed and the background potential energy is equal to the potential energy at the boundary. The background potential energy flux is influenced by internal waves passing the boundary, similar to the potential energy and available potential energy. Therefore, the background potential energy flux cannot be differentiated from potential energy flux, if internal waves pass the boundary. Therefore, the irreversible mixing can only be determined in a control volume with boundaries far away from the source of the internal waves to avoid internal waves passing the boundaries. The irreversible mixing is quantified by the change in background potential energy inside the control volume. Boundary fluxes of background potential energy are not considered, since the method to calculate these is influenced too much by minor changes at the boundary. Further research can search for another method to determine the background potential energy flux at the boundary of the control volume. Another possibility is to look into the energy budget and determine whether the conservation of energy assumed in Equation 3.13 based on Equation 2.8 is truly conserved or an additional term is needed in case of a bounded control volume in an open domain, such as the pressure gradient.

6.4. Implications results on salt intrusion

A relation between change in salt intrusion length and vertical mixing was found in Section 3.6. The change in salt storage due to estuarine circulation is proportional to the change in buoyancy frequency of the background state. The salt storage is related to the salt intrusion length and the buoyancy frequency is influenced by the stratification profile, which is changed due to vertical mixing. In Section 5.3 it was determined that the salt imported by estuarine circulation is reduced by 1.76% compared to the initial situation, due to the presence of bed waves of amplitude 0.5 m and the thereby generated internal waves, for a linear stratification. The relation between salt imported into the estuary by estuarine circulation and buoyancy frequency is only valid for a linear stratification, as the buoyancy frequency is then independent of depth. For the tangent hyperbolic stratification, the buoyancy frequency varies with depth. Therefore, it is more complex to determine one representative value for the entire vertical. Further research is needed to establish the relation between the buoyancy frequency and salt imported by estuarine circulation for a stratification other than linear. For the tangent hyperbolic stratification, the vertical distance over which the sharp density gradient is present needs to be determined for each time step. The average buoyancy frequency should be determined based on this vertical distance. In

this way, the depth-averaged buoyancy frequency is not influenced by the very small values near the surface and bottom of the water column where the fluid is well mixed. Another possibility is to keep the buoyancy frequency as a local variable and determine the vertical eddy diffusivity locally, which can be locally added to a model simulation of the estuary. This also aligns with the locally determined buoyancy frequency used in the relation of Osborn (1980). The proportionality found in 3.15 can in that case also be used for a non-linear stratification profile.

The reduction of salt imported by estuarine circulation of 1.76% compared to the initial situation is reached if the additional vertical mixing is present over the full estuary. Therefore, the bed waves need to be implemented in multiple places of the estuary to increase the diffusivity over the full estuary. The results of the simulations show the internal waves propagate a few hundred meters upstream and downstream of the bed waves. Therefore, gaps can be left between bed wave trains. The bed waves could be placed every other kilometer for example. However, to determine in which part of the estuary bed waves are the most effective for generating internal waves more research is needed. A better understanding of the effect of the mixing generated by internal waves on the processes related to salt intrusion needs to be gained by simulations of an entire estuary. In this way, it can be determined in which part of the estuary bed waves are the most effective to generate internal waves resulting in additional mixing. Moreover, the amount of bed waves needed can be determined.

In a more general sense, the method can be applied to other estuaries besides the Rotterdam Waterway. However, the salt intrusion is very dependent on the specific characteristics of the estuary. In general, the effect of mixing by internal waves is expected to be small if estuarine circulation is not a dominant forcing mechanism of salt intrusion in the estuary.

7

Conclusion

7.1. Conclusion

This research aimed to quantify irreversible mixing generated by internal waves and determine the potential to reduce salt intrusion in the Rotterdam Waterway by internal wave generation over geometrical features. To this extent, simplified simulations of a decelerating flow over an undular bed were done for an idealized section of the Rotterdam Waterway using a non-hydrostatic numerical model.

The irreversible mixing is quantified by determining the background potential energy in a chosen part of the domain. The background potential energy is the potential energy found if the density in a control volume is adiabatically reordered to the state of minimum potential energy. This method functions very well for a closed domain since the total energy in the control volume is always conserved. However, when an open domain is considered, the applicability of the method is limited. Determining the boundary flux of background potential energy is difficult as the method used is based on calculation over a volume to average out fluctuations, which is impossible at the boundary. To solve this, the boundaries of the control volume should be chosen far enough from the source generating internal waves, to avoid internal waves passing the boundaries. Furthermore, the domain should be sufficiently long in the case of bottom friction to ensure the boundary layer is fully developed before the control volume starts.

The bed wave amplitude greatly influenced the generation of internal waves. An increased bed wave amplitude increased the internal wave amplitude by the same order of magnitude for the frictionless case. Furthermore, the tangent hyperbolic profile increased the background potential energy by 1.8% of the energy required for a fully mixed control volume compared to the linear profile. The mixing generated in the domain is related to salt intrusion by the buoyancy frequency of the state of minimum potential energy. The squared buoyancy frequency was found to be proportional to the salt imported by estuarine circulation.

The model results show the salt intrusion caused by estuarine circulation is reduced by 1.76% compared to the initial state due to internal waves generated in a linear stratified flow over bed waves of amplitude 0.5 m and length 50 m present in 27.5% of the domain of interest. This result is found for a case without bottom friction. However, in reality, the Rotterdam Waterway has a rough bed. Bottom friction was found to reduce the internal wave amplitude by 80%, due to dissipation of internal wave energy. Therefore, the reduction in salt intrusion is expected to be smaller in the Rotterdam Waterway. The result is for a linear stratification, while the Rotterdam Waterway has a tangent hyperbolic stratification. The internal wave amplitude for a tangent hyperbolic stratification is 25% larger than for a linear profile for simulations including bottom friction and 10% larger than for the linear stratification for simulations without bottom friction. Furthermore, the internal waves are generated at a higher background velocity and are longer present in the domain, resulting in more time to mix.

To conclude, internal waves generated over geometrical features are capable of reducing the salt intrusion caused by estuarine circulation by a few percent compared to the initial situation for the Rotterdam Waterway, if bed waves are present over a quarter of the topography.

7.2. Recommendations

Based on the outcome of this research recommendations for further research are done. The first recommendation is to do simulations including bottom friction using a larger model domain to be able to quantify the mixing generated in the case of bottom friction correctly. The domain should be large enough for the boundary layer to be fully developed before the area of interest starts.

Another recommendation is to search for a method to determine the buoyancy frequency as one representative value of the domain in the case of a non-linear stratification. For a tangent hyperbolic profile this can be done by determining the distance over which the density gradient is present and only using that part of the domain to find the buoyancy frequency.

The results found are for a bed wave coverage of 27.5% of the topography. This amount is not yet optimized. Therefore, simulations with different degrees of bed wave coverage should be executed to determine the optimal spacing and degree of bed waves.

The results are based on a small part of the estuary. Therefore, simulations of the full estuary are needed to determine the effectiveness of additional mixing if the stratification changes over the horizontal. Furthermore, observations of the estuary are needed to verify estuarine circulation is the dominant forcing mechanism in all parts of the estuary, as well as to analyse the velocity profiles to determine the influence of the neglected asymmetric tidal effects.

Lastly, to determine if the use of bed waves is cost-efficient for the Rotterdam Waterway a cost-benefit analysis should be made of the construction and maintenance of the bed waves and the expected reduction in salt intrusion.

References

Bergh, J., & Berntsen, J. (2009). Numerical studies of wind forced internal waves with a nonhydrostatic model. *Ocean Dynamics*, *59*, 1025–1041.

Bowden, K. (1963). The mixing processes in a tidal estuary. *International Journal of Air and Water Pollution*, *7*(4-5), 343–356.

Deardorff, J. W. (1970). A numerical study of three-dimensional turbulent channel flow at large reynolds numbers. *Journal of Fluid Mechanics*, *41*(2), 453–480.

de Nijs, M. A., Pietrzak, J. D., & Winterwerp, J. C. (2011). Advection of the salt wedge and evolution of the internal flow structure in the rotterdam waterway. *Journal of Physical Oceanography*, *41*(1), 3–27.

Dijkstra, Y. M., Schuttelaars, H. M., & Kranenburg, W. M. (2022). Salt transport regimes caused by tidal and subtidal processes in narrow estuaries. *Journal of Geophysical Research: Oceans*, *127*(12). https://doi.org/10.1029/2021JC018391

Dimotakis, P. E. (2005). Turbulent mixing. *Annu. Rev. Fluid Mech.*, *37*, 329–356.

Farmer, D. M., & Freeland, H. J. (1983). The physical oceanography of fjords. *Progress in Oceanography*, *12*(2), 147–219. https://doi.org/10.1016/0079-6611(83)90004-6

Friocourt, Y., Kuijper, K., & Leung, N. (2014). *Salt intrusion* [Deltafact]. https://www.stowa.nl/deltafacts/zoetwatervoorziening/delta-facts-english-versions/salt-intrusion

Ganju, N. K., & Sherwood, C. R. (2010). Effect of roughness formulation on the performance of a coupled wave, hydrodynamic, and sediment transport model. *Ocean Modelling*, *33*(3-4), 299–313.

Geyer, W. R., & MacCready, P. (2014). The estuarine circulation. *Annual review of fluid mechanics*, *46*, 175–197.

Google. (n.d.). Google maps rotterdam waterway [Online; accessed May 29, 2024]. https://www.google.com/maps/@51.9594198,4.231067,11.5z?entry=ttu

Hendrickx, G. G., Kranenburg, W. M., Antolínez, J. A., Huismans, Y., Aarninkhof, S. G., & Herman, P. M. (2023). Sensitivity of salt intrusion to estuary-scale changes: A systematic modelling study towards nature-based mitigation measures. *Estuarine, Coastal and Shelf Science*, *295*, 108564. https://doi.org/10.1016/j.ecss.2023.108564

Huppert, H. E. (1980). Topographic effects in stratified fluids. In *Fjord oceanography* (pp. 117–140). Springer.

Ivey, G., Winters, K., & Koseff, J. (2008). Density stratification, turbulence, but how much mixing? *Annu. Rev. Fluid Mech.*, *40*(1), 169–184. https://doi.org/10.1146/annurev.fluid.39.050905.110314

Jones, N., Ivey, G., Rayson, M., & Kelly, S. (2020). Mixing driven by breaking nonlinear internal waves. *Geophysical Research Letters*, *47*(19). https://doi.org/10.1029/2020GL089591

Kranenburg, C. (1988). On internal waves in partially mixed and stratified tidal flows. In *Physical processes in estuaries* (pp. 213–238). Springer.

Kranenburg, C., & Pietrzak, J. D. (1989). Internal lee waves in turbulent two-layer flow. *Journal of Hydraulic Engineering*, *115*(10), 1352–1370. https://doi.org/10.1061/(ASCE)0733-9429(1989)115:10(1352)

Kranenburg, W. M. (2015). *Evaluatie van het osr-model voor zoutindringing in de rijnmaasmonding (i): Onderdeel kpp b&o waterkwaliteitsmodelschematisaties 2014*. Deltares.

Kranenburg, W. M., Van der Kaaij, T., Tiessen, M., Friocourt, Y., & Blaas, M. (2022). Salt intrusion in the rhine meuse delta: Estuarine circulation, tidal dispersion or surge effect. *Proceedings of the 39th IAHR World Congress. June. Granada, Spain*, 5601–5608.

Kuijper, C., & v.d. Kaaij, T. (2009). *Herstel van de "trapjeslijn" in de nieuwe waterweg en de nieuwe maas: Fase 1: Voorstudie naar de effecten op de zoutindringing*. waterdienst. Deltares.

Labeur, R. J. (2009). *Finite element modelling of transport and non-hydrostatic flow in environmental fluid mechanics* [Phd thesis]. Delft University of Technology. http://resolver.tudelft.nl/uuid:7b2d7144-4ea8-4bba-9a05-14ec761b43c3

Labeur, R. J., & Pietrzak, J. D. (2004). Computation of non-hydrostatic internal waves over undular topography [International symposium on shallow flows, Delft, 2003 ; Conference date: 16-06-2003 Through 18-06-2003]. In G. Jirka & W. Uijttewaal (Eds.), *Proceedings of the international symposium on shallow flows* (pp. 187–194). CRC Press / Balkema - Taylor & Francis Group.

Labeur, R. J., & Pietrzak, J. D. (2005). A fully three dimensional unstructured grid non-hydrostatic finite element coastal model [The Second International Workshop on Unstructured Mesh Numerical Modelling of Coastal, Shelf and Ocean Flows]. *Ocean Modelling*, *10*(1), 51–67. https://doi.org/10.1016/j.ocemod.2004.06.008

Lamb, K. G. (2007). Energy and pseudoenergy flux in the internal wave field generated by tidal flow over topography. *Continental shelf research*, *27*(9), 1208–1232.

Lamb, K. G., & Nguyen, V. T. (2009). Calculating energy flux in internal solitary waves with an application to reflectance. *Journal of Physical Oceanography*, *39*(3), 559–580.

Launder, B. E., & Spalding, D. B. (1983). The numerical computation of turbulent flows. In *Numerical prediction of flow, heat transfer, turbulence and combustion* (pp. 96–116). Elsevier.

Lee, H., Calvin, K., Dasgupta, D., Krinner, G., Mukherji, A., Thorne, P., Trisos, C., Romero, J., Aldunce, P., Barret, K., Blanco, G., Cheung, W. W., Connors, S. L., Denton, F., Diongue-Niang, A., Dodman, D., Garschagen, M., Geden, O., Hayward, B., … Park, Y. (2023). *Climate change 2023: Synthesis report, summary for policymakers.* (10.59327/IPCC/AR6-9789291691647.001). Intergovernmental Panel on Climate Change (IPCC). Geneva, Switzerland, Intergovernmental Panel on Climate Change (IPCC).

Lee, J., Biemond, B., de Swart, H., & Dijkstra, H. A. (2024). Increasing risks of extreme salt intrusion events across european estuaries in a warming climate. *Communications Earth & Environment*, *5*(1), 60.

Linden, P. F., & Simpson, J. E. (1986). Gravity-driven flows in a turbulent fluid. *Journal of Fluid Mechanics*, *172*, 481–497. https://doi.org/10.1017/S0022112086001829

Long, R. R. (1955). Some aspects of the flow of stratified fluids: Iii. continuous density gradients. *Tellus*, *7*(3), 341–357.

MacCready, P. (2004). Toward a unified theory of tidally-averaged estuarine salinity structure. *Estuaries*, *27*, 561–570. https://doi.org/10.1007/BF02907644

Miles, J. W. (1961). On the stability of heterogeneous shear flows. *Journal of Fluid Mechanics*, *10*(4), 496–508.

O'Hogain, S., & McCarton, L. (2018). Nature-based solutions. *A Technology Portfolio of Nature Based Solutions: Innovations in Water Management*, 1–9.

Osborn, T. R. (1980). Estimates of the local rate of vertical diffusion from dissipation measurements. *Journal of physical oceanography*, *10*(1), 83–89. https://doi.org/10.1175/1520-0485(1980)010<0083:EOTLRO>2.0.CO;2

Pietrzak, J. D., Kranenburg, C., & Abraham, G. (1990). Resonant internal waves in fluid flow. *Nature*, *344*, 844–847. https://doi.org/10.1038/344844a0

Pietrzak, J. D., Kranenburg, C., Abraham, G., Kranenborg, B., & van der Wekken, A. (1991). Internal wave activity in rotterdam waterway. *Journal of Hydraulic Engineering*, *117*(6), 738–757. https://doi.org/10.1061/(ASCE)0733-9429(1991)117:6(738)

Pietrzak, J. D., & Labeur, R. J. (2004). Trapped internal waves over undular topography in a partially mixed estuary. *Ocean Dynamics*, *54*(3), 315–323. https://doi.org/10.1007/s10236-003-0081-4

Port of Rotterdam. (2021). *Port information guide*.

Raudkivi, A. J. (1997). Ripples on stream bed. *Journal of Hydraulic Engineering*, *123*(1), 58–64.

Reynolds, A. (1975). The prediction of turbulent prandtl and schmidt numbers. *International Journal of heat and mass transfer*, *18*(9), 1055–1069.

Rijkswaterstaat. (2024a). Gauge data at hoek van holland. https://waterinfo.rws.nl/#/expert/Waterhoogten/Hoek-van-Holland%28HOEKVHLD%29/details?parameters=Waterhoogte___20berekend___20Oppervlaktewater___20t.o.v.___20Normaal___20Amsterdams___20Peil___20in___20cm

Rijkswaterstaat. (2024b). *Nieuwe waterweg*. https://www.rijkswaterstaat.nl/water/vaarwegenoverzicht

Simpson, J. H., Brown, J., Matthews, J., & Allen, G. (1990). Tidal straining, density currents, and stirring in the control of estuarine stratification. *Estuaries*, *13*, 125–132.

Stacey, M. T., & Ralston, D. K. (2005). The scaling and structure of the estuarine bottom boundary layer. *Journal of Physical Oceanography*, *35*(1), 55–71.

Stigebrandt, A. (1976). Vertical diffusion driven by internal waves in a sill fjord. *Journal of physical oceanography*, *6*(4), 486–495.

Turner, J. S. (1979). *Buoyancy effects in fluids*. Cambridge university press.

van Rijn, L., Grasmeijer, B., & Perk, L. (2018). Effect of channel deepening on tidal flow and sediment transport: Part i—sandy channels. *Ocean Dynamics*, *68*(11), 1457–1479.

van Vliet, M. T., Franssen, W. H., Yearsley, J. R., Ludwig, F., Haddeland, I., Lettenmaier, D. P., & Kabat, P. (2013). Global river discharge and water temperature under climate change. *Global environmental change*, *23*(2), 450–464. https://doi.org/10.1016/j.gloenvcha.2012.11.002

Wegman, T. M. (2021). *Undular bottom topography as a salt intrusion mitigation measure: A study on the potential of trapped internal waves to enhance vertical mixing* [Msc thesis]. Delft University of Technology. http://resolver.tudelft.nl/uuid:c7516ec1-3698-4127-af4a-096f0b3500f1

Wei, X., Schramkowski, G. P., & Schuttelaars, H. M. (2016). Salt dynamics in well-mixed estuaries: Importance of advection by tides. *Journal of Physical Oceanography*, *46*(5), 1457–1475. https://doi.org/10.1175/JPO-D15-0045.1

Winters, K. B., & D'Asaro, E. A. (1996). Diascalar flux and the rate of fluid mixing. *Journal of Fluid Mechanics*, *317*, 179–193.

Winters, K. B., Lombard, P. N., Riley, J. J., & D'Asaro, E. A. (1995). Available potential energy and mixing in density-stratified fluids. *Journal of Fluid Mechanics*, *289*, 115–128.

Wunsch, C., & Ferrari, R. (2004). Vertical mixing, energy, and the general circulation of the oceans. *Annu. Rev. Fluid Mech.*, *36*(1), 281–314.

A

Assumptions and approach

A.1. Coriolis effect Rotterdam Waterway

The internal Rossby radius of deformation is a measure of the scale at which the rotation of the Earth influences the flow. The Rossby radius of deformation, R_I, is the ratio between the phase speed of the long internal waves and the Coriolis parameter.

$$R_I = \frac{\sqrt{\frac{\Delta\rho}{\rho_0} g H}}{f} \tag{A.1}$$

The density difference over the vertical in the Rotterdam Waterway is typically 15 kg/m³. The reference density is 1000 kg/m³. The representative water depth is 15 m. The Coriolis parameter is determined using $f = 2\Omega \sin\phi$. The latitude of the Rotterdam Waterway is 52°, resulting in a Coriolis parameter of $f = 10^{-4}$. The Rossby radius of deformation is therefore 15 km and Coriolis is neglected.

A.2. Scheme of the approach

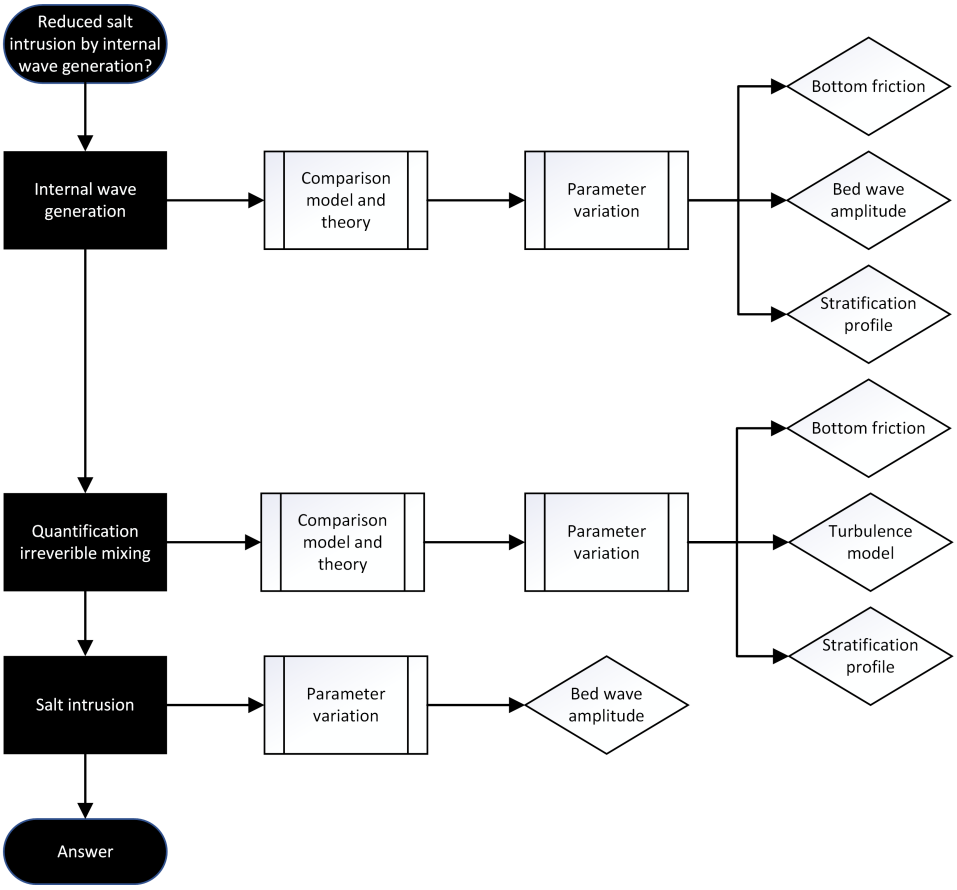

Figure A.1: Schematic of the approach used to answer the research question.

B

Model choices

B.1. Sponge layer

The sponge layer is added at the left and right boundary of the domain to prevent internal wave reflection at the boundary. In Figure B.1 a simulation without the sponge layer is shown. At the left boundary internal waves reflecting at the boundary are visible by the irregular large internal waves at the boundary. In Figure B.2 a simulation including the sponge layer is shown. Here the reflections of internal waves at the boundary are removed. Therefore, the sponge layer is effective in removing internal waves reflecting at the boundaries. Both simulations include bottom friction. The only waves still present at the left boundary at the end of the sponge layer are caused by a mismatch between the velocity prescribed at the boundary and the velocity determined in the domain. This effect is reduced by prescribing a logarithmic velocity profile at the boundary.

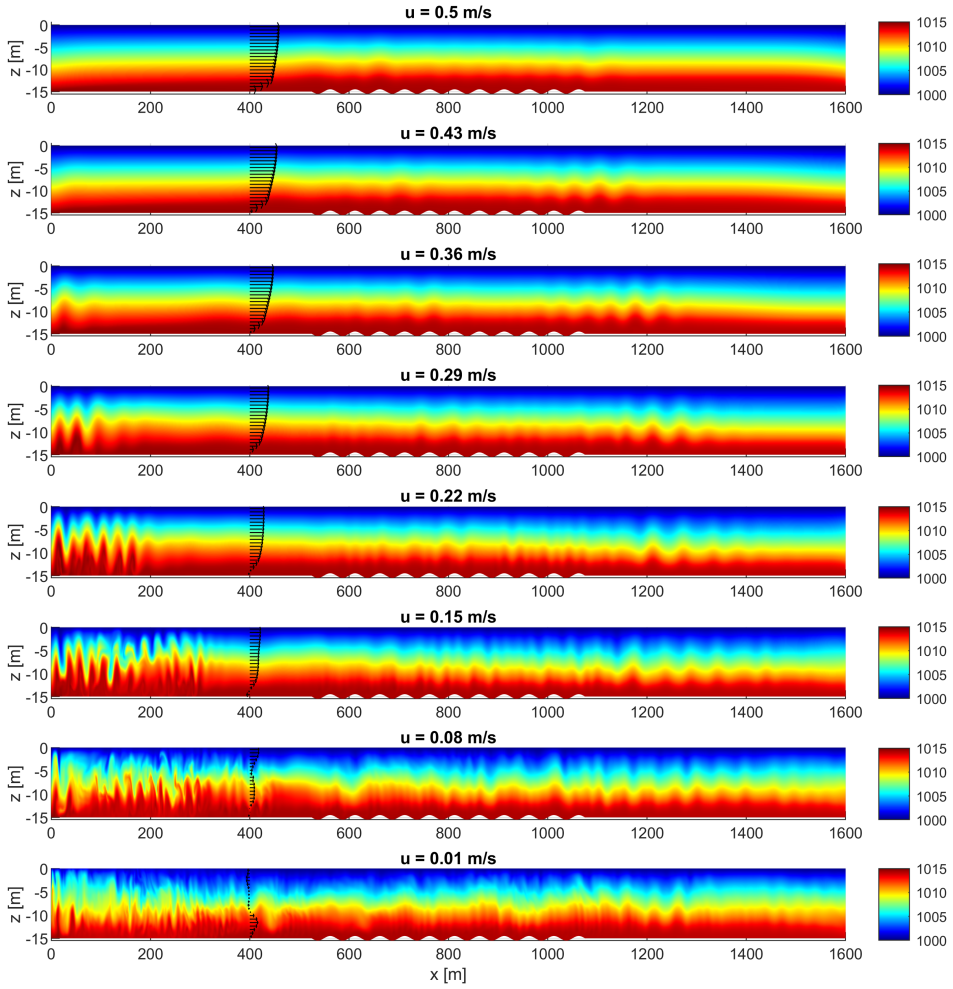

Figure B.1: Simulation of a decelerating flow including bottom friction without sponge layer. Bed waves of amplitude 0.5 m are present. The flow is from left to right.

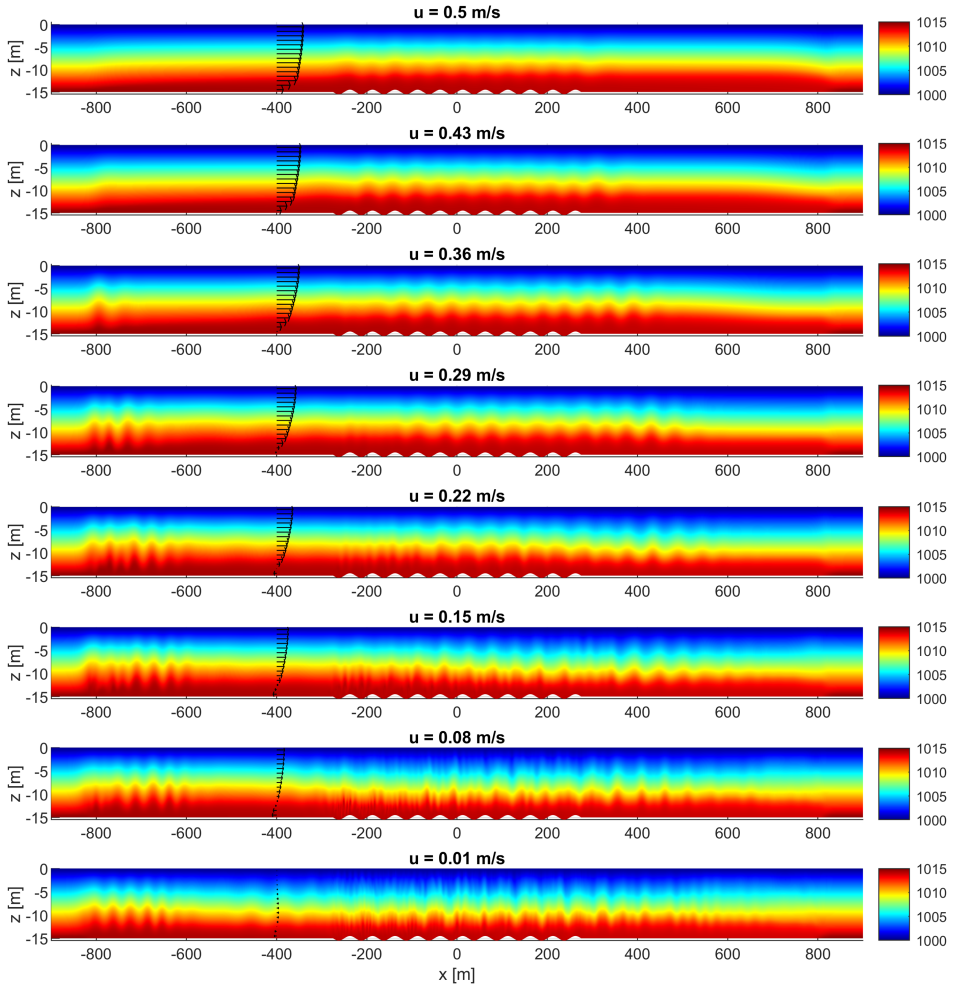

Figure B.2: Simulation of a decelerating flow including bottom friction with sponge layer. Bed waves of amplitude 0.5 m are present. The flow is from left to right.

B.2. Domain size

The domain length is chosen based on earlier numerical simulation based on the Rotterdam Waterway (Pietrzak & Labeur, 2004; Wegman, 2021). This was the starting point for the domain size. From there the domain size was increased. In this way, the influence of the domain size on the results was investigated. In all runs the sponge layer is present at the last 100 m on both sides of the domain. Three different domain lengths are investigated: 1800 m, 3600 m and 7200 m. The model set-up is the same for all three simulations, except for the domain length. The input parameters are the same as the base case, expect the velocity amplitude at the boundaries, which is 0.5 m/s instead of 1 m/s to focus on the part in which the flow is subcritical.

The results of the simulations are shown in Figures B.3, B.4, B.5 respectively. The plots are zoomed in to $-500 \leq x \leq 500$, since most internal waves are present in this part of the domain. The results of the three simulations are the same. Therefore, no boundary effects travel into the domain of interest. A domain length of 3600 m is chosen for the final simulations. The extra space between the boundaries and start of the bed waves create more time for the boundary layer to develop in the case of simulations including bottom friction.

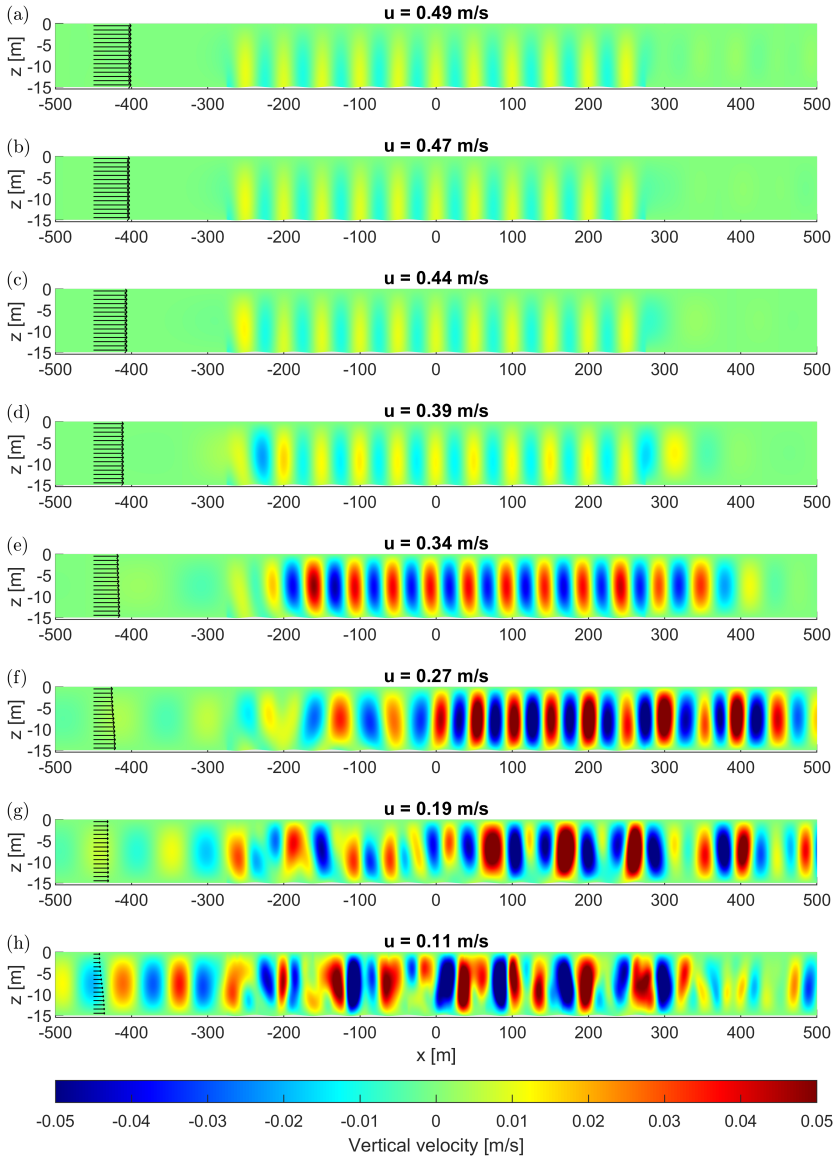

Figure B.3: Vertical velocity profiles of different time instances from a simulation using a domain stretching over $-900 \leq x \leq 900$. Bed waves of amplitude 0.15 m are present over $-275 \leq x \leq 275$ m. The flow is from left to right.

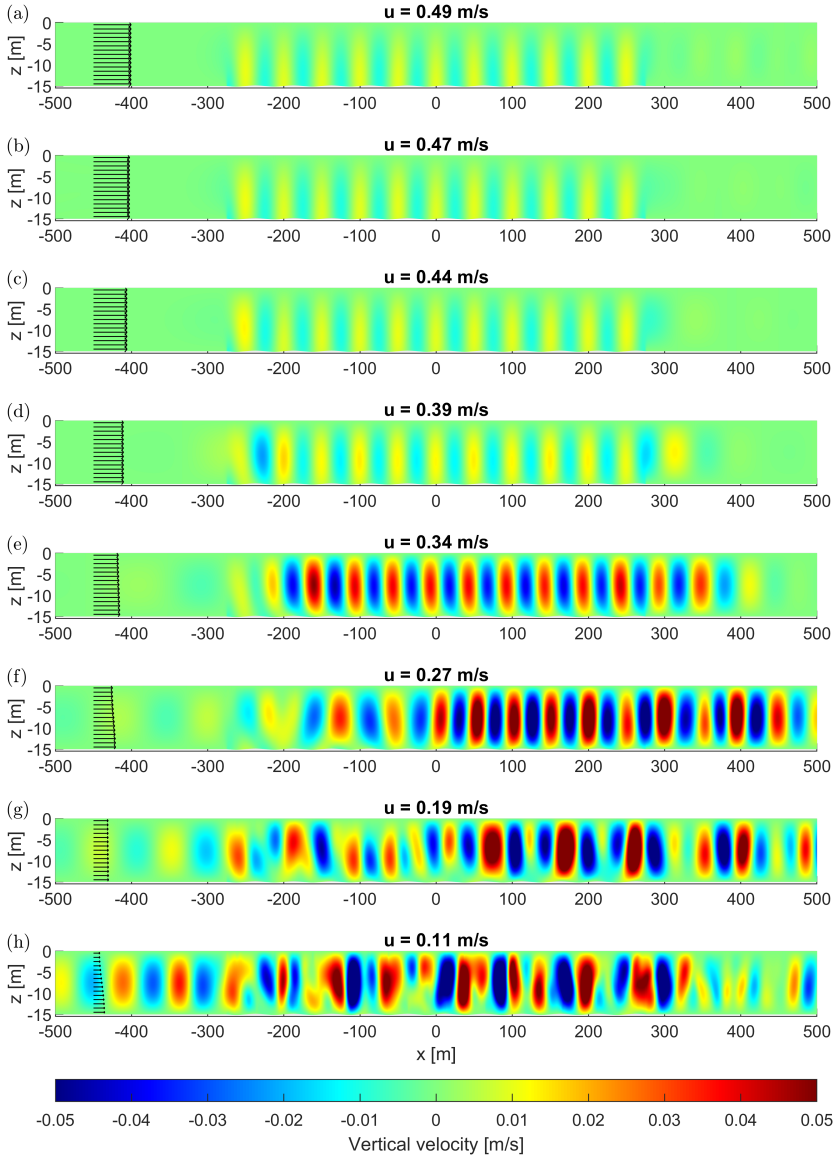

Figure B.4: Vertical velocity profiles of different time instances from a simulation using a domain stretching over $-1800 \leq x \leq 1800$. Bed waves of amplitude 0.15 m are present over $-275 \leq x \leq 275$ m. The flow is from left to right.

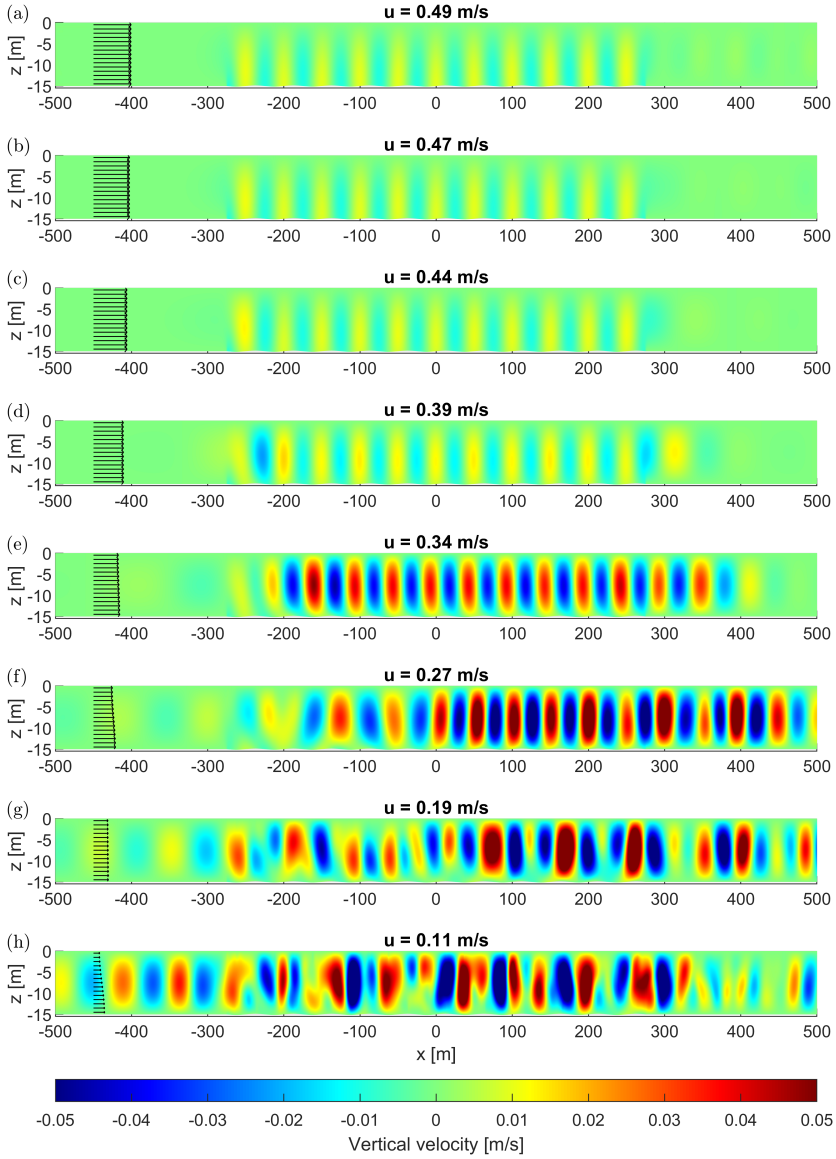

Figure B.5: Vertical velocity profiles of different time instances from a simulation using a domain stretching over $-3600 \leq x \leq 3600$. Bed waves of amplitude 0.15 m are present over $-275 \leq x \leq 275$ m. The flow is from left to right.

B.3. Control volume size

The influence of the size of the control volume and thereby the locations of the boundaries is shown in Figure B.6 for the base case. The different control volumes are centred around $x = 0$. The smallest control volume, solid black line, shows the most fluctuations in cumulative production. A smaller control volume causes the internal waves propagation away from the bed waves to reach the boundaries of the control volume earlier. This results in more fluctuations of the production at an earlier time step. To avoid these boundary effects the control volume of 2000 m is chosen, which is from $-1000 \leq x \leq 1000$.

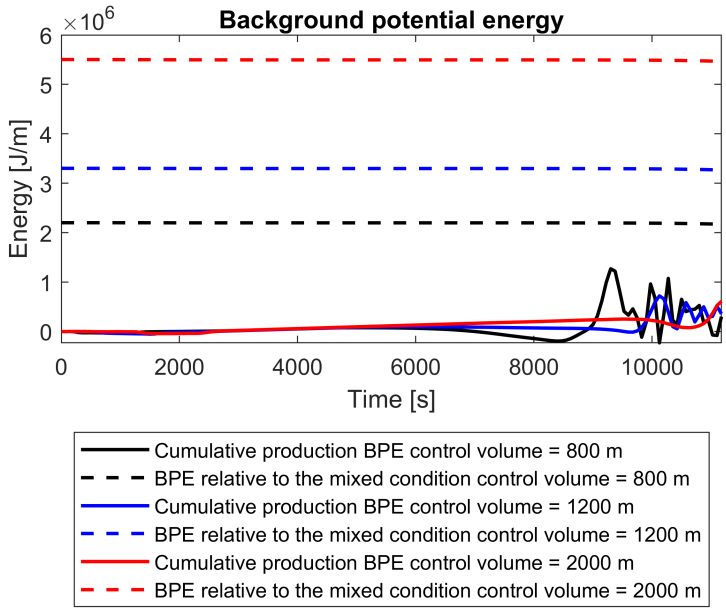

Figure B.6: Background potential energy for three different control volume sizes. Results for a simulation of a decelerating flow without bottom friction, the base case #0.

B.4. Velocity profile boundary

In the simulations using bottom friction the boundary layer needs time and therefore horizontal length to develop. To reduce the distance needed a logarithmic profile is used as input for the velocity boundaries. The velocity profile is determined empirically using numerical simulation. A run with a flat bottom including bottom friction and uniform velocity boundaries is executed. The run is the same as the base case, except for the flat bottom, bottom friction and a spin-up time of 2000 seconds during which the velocity boundaries are kept constant at 1 m/s. The vertical velocity profile is taken at x = 400 m every time step. These vertical profiles are used as the input for the runs containing bottom friction. In this way the domain size does not have to be extended, reducing computational time. The velocity profiles over time are shown in Figure B.7. The orange line is the first time step and blue the last. After 8000 seconds, around a depth-averaged velocity of 0.43 m/s, a return flow starts to develop near the bottom, which increases as the flow decelerates further. This is also visible in the figure when the blue lines start to have a negative velocity near the bottom.

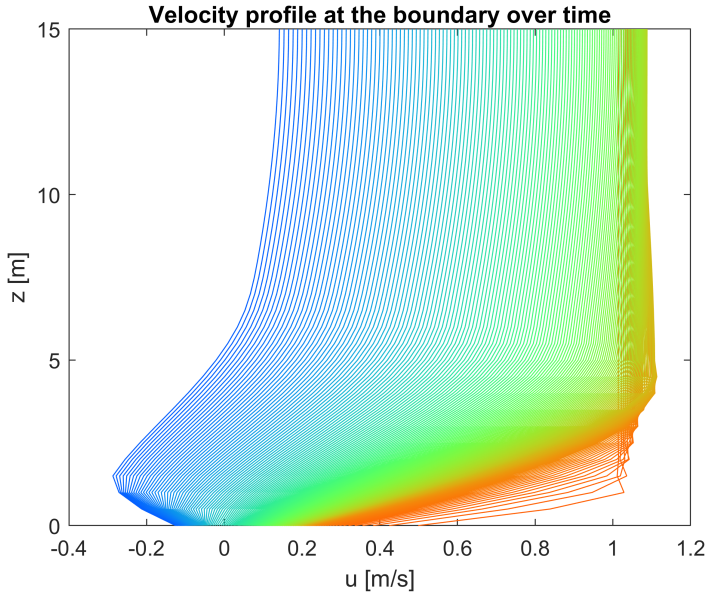

Figure B.7: Velocity profiles imposed at the boundaries for each time step. The orange lines are the first time steps and the blue the last ones.

B.5. Refinement

The verify the accuracy of the results the grid size and the output mapping are refined. The background potential energy is calculated for each refined simulation. For all of the refinements the base case scenario, run #0 of Table 3.3, is used.

B.5.1. Output step

To avoid large amounts of data the rate at which output files containing the flow variables are created can be chosen different from the computational time step. Based on visible observations of the density field a output mapping step of 75 seconds is suitable for the simulations. At this rate changes in propagation direction, as well as, the amplitude of the internal waves are clearly visible in plots of the density and vertical velocity fields. When simulating a quarter M2-tide an output rate each 75 seconds results in 150 output files, this amount can be processed and analyse at low computational costs. Furthermore, the bed waves are present over 550 meters of the domain and the total domain length is 3600 meters. The maximum flow velocity is 1 m/s and reduces with time. Therefore, the advection by the flow is at maximum 75 meters, which is well within the domain length.

The influence of rate of generating output on the amount of potential energy is determined by comparing the potential energy calculated using output which is generated each second to potential energy calculated using output which is generated each 75 seconds. Figure B.8 shows that the potential energies calculated are similar for both output rates. The lines of an output rate of 1 s and 75 s overlap for each of the three potential energies. The background potential energy production is shown for output rates of each second and each 75 seconds in Figure B.9. The difference between the two mapping times is very small. Therefore, an output rate of each 75 seconds is suitable for determining the background potential energy accurately.

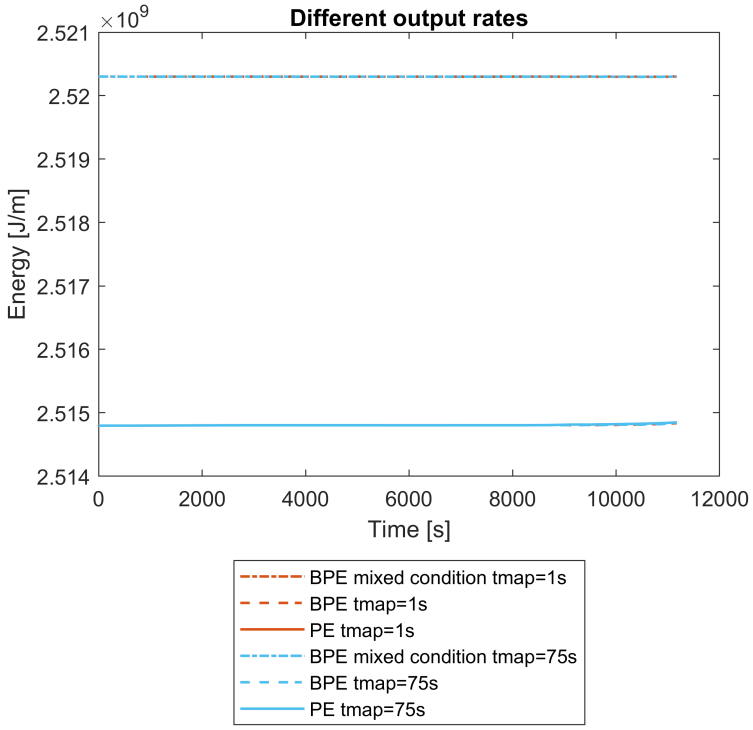

Figure B.8: Background potential energy in case of a fully mixed control volume, background potential energy and potential energy for output rates of 1 second and 75 seconds.

B.5.2. Grid size

To determine the influence of the grid size the grid is refined. In Figure B.10 it can be seen the background potential energy barely changes when compared to background potential energy of the fully mixed control volume. Figure B.11 shows the difference in background potential energy between coarser grids and a grid of 0.25x0.25m relative to the potential energy needed to mix the control volume.

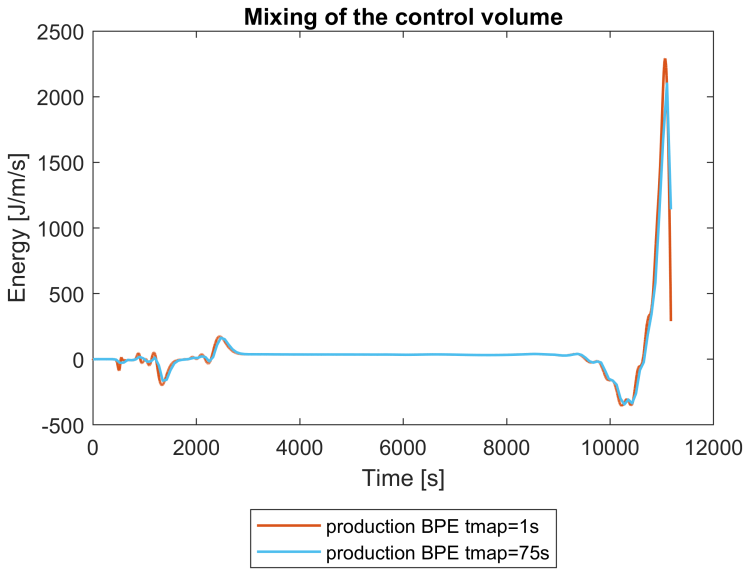

Figure B.9: The amount of background potential energy generated in the control volume for two different output rates. The production of energy is caused by mixing. A negative value for the production indicates counter-gradient mixing.

It shows the difference between the coarsest and finest grid is less than 0.5%.

The generation of background potential energy on different grid sizes is shown in Figure B.12. The production of the energy is related to the energy needed to change from the initial state to a fully mixed control volume. The figure shows the production is small compared to the energy needed, at maximum 2.5%. The simulations using different grid sizes, the blue lines, all have similar results, the difference between the coarsest and the finest grid is around 0.05% production background potential energy relative to background potential energy anomaly. This is a difference of around 5% at maximum between the coarsest and finest grid. Therefore, the grid of 1x0.5m is fine enough.

The results of the interpolation of the 1x0.5m grid to finer grids, orange lines, show different results than the simulations using these finer grids, blue lines. This could be due to the fact that the density and velocity fields are linearly interpolated, which smoothens the sharper density gradients created by the larger internal waves. Furthermore, the interpolated grids have a difference between the coarsest and the finest grid of around 0.0001% production background potential energy relative to background potential energy anomaly. The interpolated results are obtained using the same input, the result of the 1x0.5m grid. Since the interpolation is linear, a finer grid results in more points on an linear line. The integration is done using the trapeziodal method. Therefore, the difference between interpolation on different finer grid sizes is very small, as observed. Since the difference between simulations using finer grid sizes results in negligible differences, interpolation is not necessary.

The maximum Courant number of the runs with different grid sizes are shown in Figure B.13. The Courant numbers are similar for each run, which is achieved by adapting the time step to the horizontal grid size. In this way, the effect of different advection in the different runs is removed. The maximum Courant number is mostly below 1, only when the flow is initiated the maximum Courant number is above 1. Therefore, no instabilities are caused due to a too large Courant number.

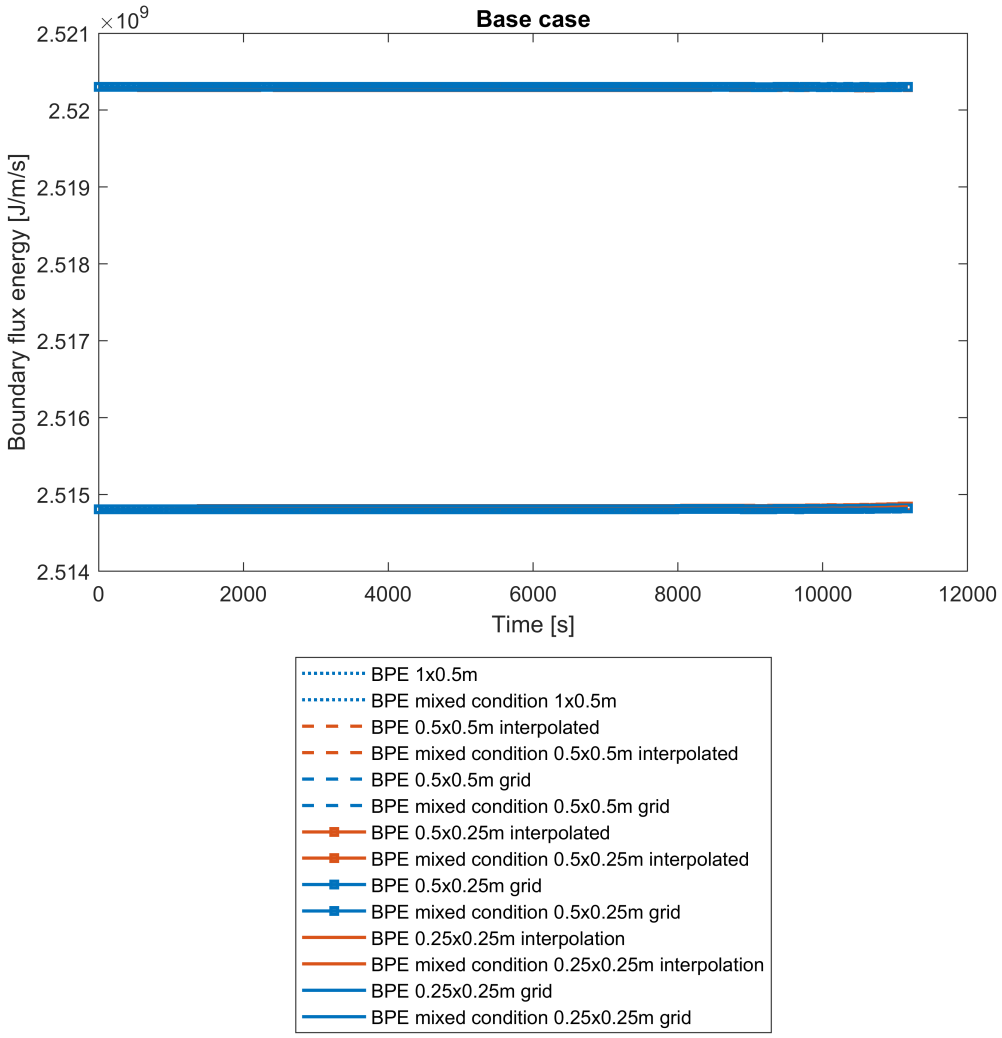

Figure B.10: The lines on the top in the figure are the background potential energy when the control volume is fully mixed. The lines on the bottom are the background potential energy. Simulations on different grids are shown, as well as, interpolations of the 1x0.5m grid to finer grids.

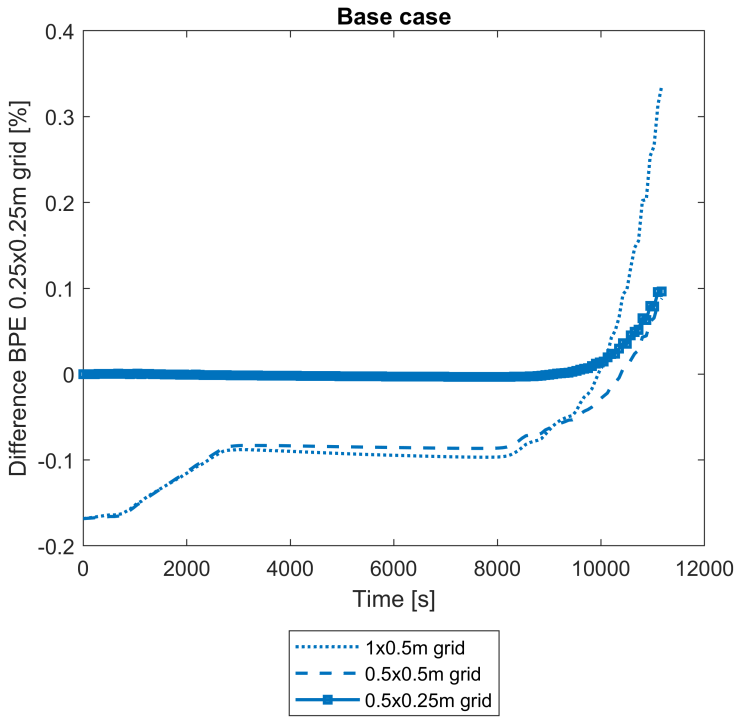

Figure B.11: The difference in background potential energy of the finest grid of 0.25x0.25m and different coarser grid sizes relative to the energy still needed to mix the full control volume.

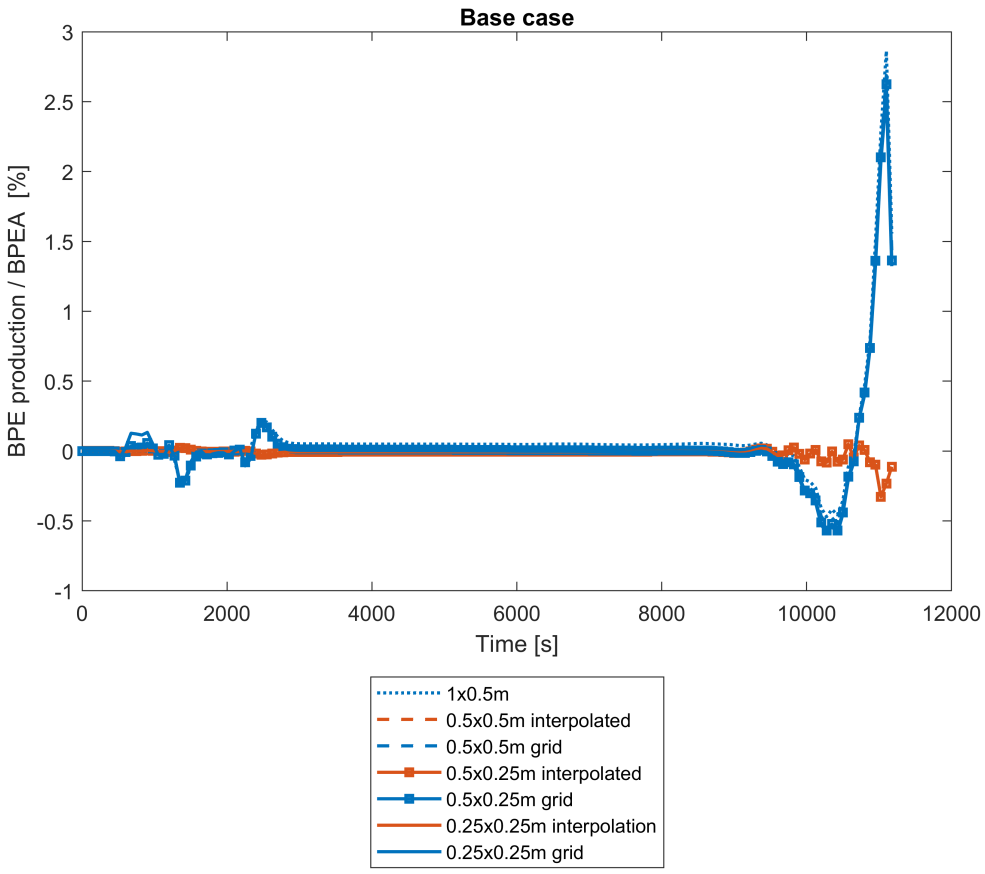

Figure B.12: The amount of background potential energy resulting from mixing in the control volume relative to the amount of energy that is needed to fully mix the control volume. Simulations on different grids are shown, as well as, interpolations of the 1x0.5m grid to finer grids.

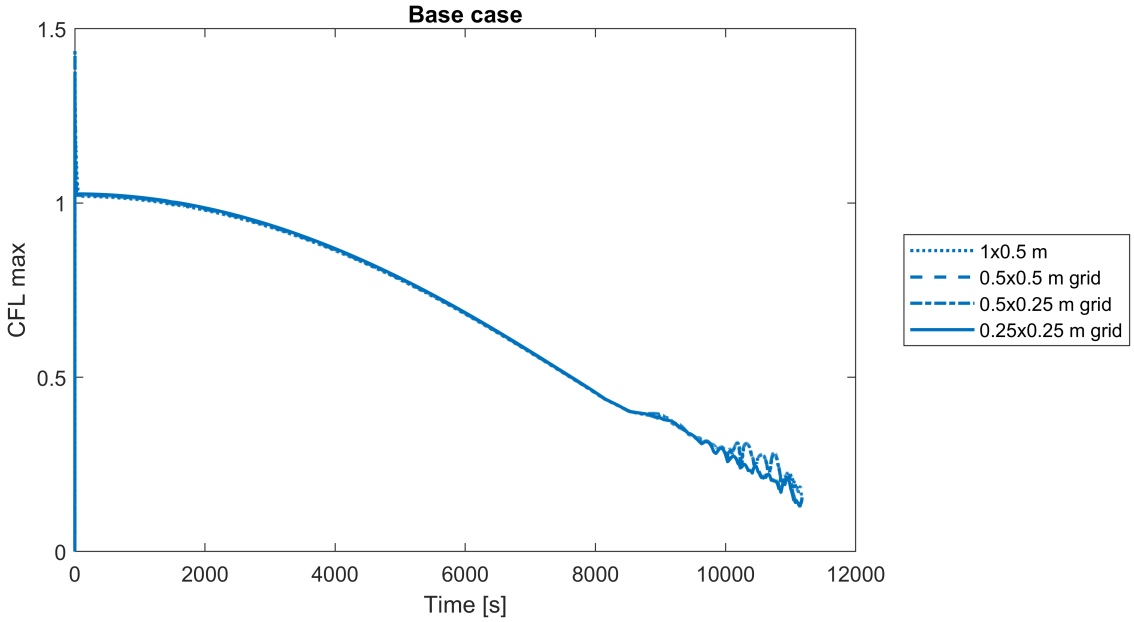

Figure B.13: Courant numbers for simulations using different grid sizes.

C

Internal wave generation

C.1. Verification internal wave generation

The simulations for constant velocities other than mode 1 and simulations of decelerating and accelerating flow referred to in Section 4.2 are shown in this section.

C.1.1. Stationary flow

The second resonant mode is approached in Figure C.1. The analytical solution does not match the model result exactly. Therefore, the background velocity for the Taylor Goldstein equation was chosen slightly higher in the bottom plot, 0.235 m/s instead of 0.22 m/s, which is an increase of 6.8%. The deviation between the background velocity used in model or theory has a small order of magnitude and can be explained by truncation errors. There is a good match between the model solution and Taylor Goldstein equation with slightly higher background velocity, both Figure C.1 (a) and (c) show a response belonging to a mode slightly below 2. The diffusion of vertical velocities of similar sign towards each other visible in the model simulation is caused by numerical diffusion (Labeur & Pietrzak, 2005).

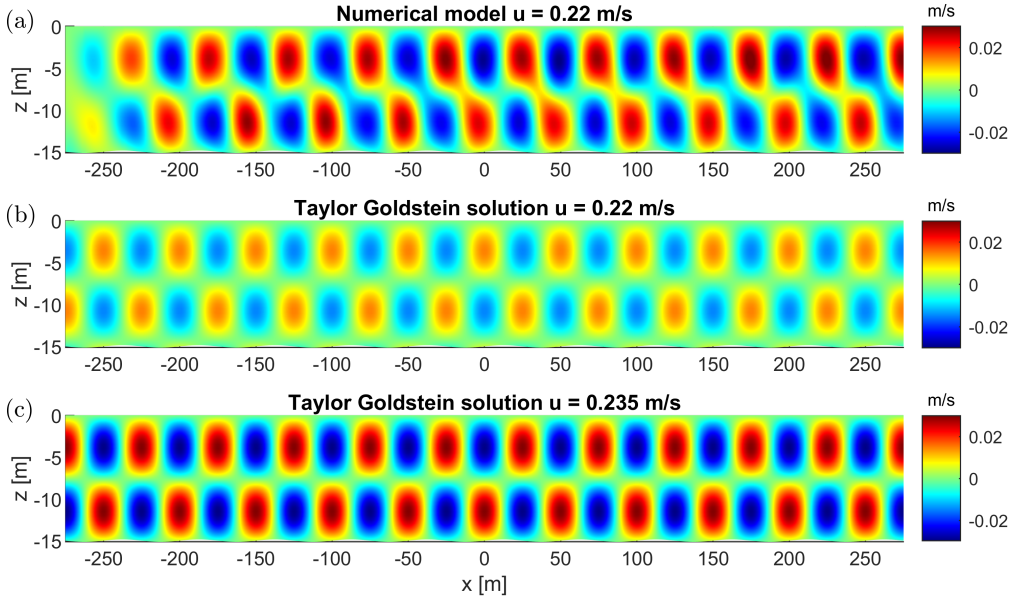

Figure C.1: Theoretical resonant mode 2 response. Bed waves of amplitude 0.15 m are present over $-275 \leq x \leq 275$ m. The flow is from left to right. (a) The vertical velocity determined using the numerical model for a flow with a constant background velocity of 0.22 m/s and including viscosity. (b) The vertical velocity found using the analytical solution to the Taylor Goldstein equation for a constant velocity of 0.22 m/s. (c) The vertical velocity found using the analytical solution to the Taylor Goldstein equation for a constant velocity of 0.236 m/s.

A near resonant mode 3 response and the related Taylor Goldstein solutions are shown in Figure C.2. The vertical velocity magnitudes and the mode of the theoretical solutions and model solution do not match, , Figure C.2 (a) and (b) respectively. Therefore, the background velocity of the analytical solution is slightly increased. The increase in background velocity is 0.009 m/s which is 6% of the initial value of 0.15 m/s. A difference of this order of magnitude could be explained by numerical errors, similar to the mode 2. The vertical velocity is of the same order of magnitude in Figure C.2 (a) and (c). The mode of the response in these plots also corresponds to each other. In both plots a near mode 3 response is visible and the direction of the vertical velocity matches as well. Using the slightly adjusted background velocity the vertical velocity patterns of the model and analytical solution are a good match. Furthermore, similar to the results of mode 2 some numerical diffusion is present in the model simulation.

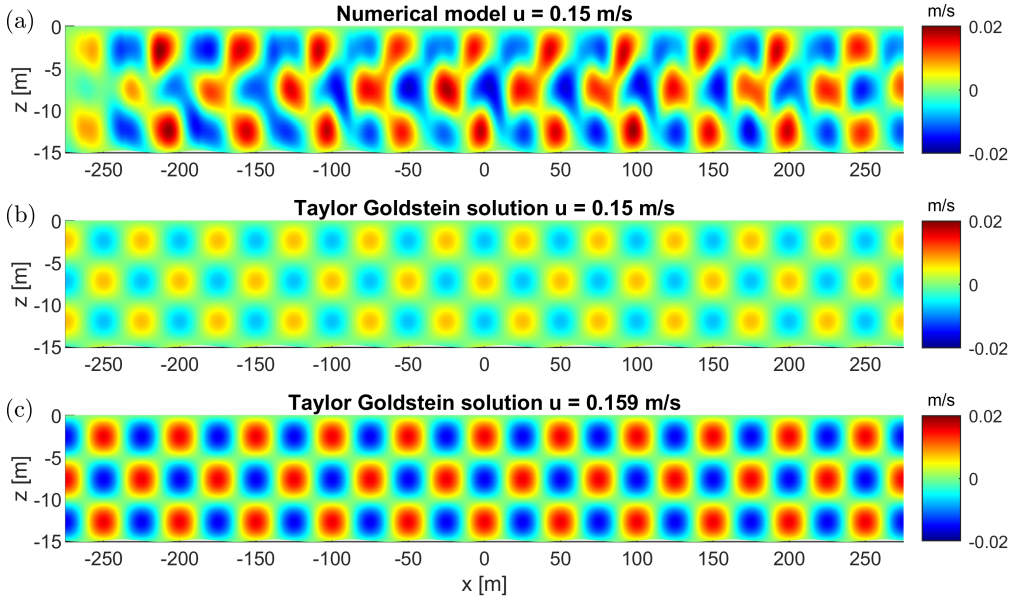

Figure C.2: Theoretical resonant mode 3 response. Bed waves of amplitude 0.15 m are present over $-275 \leq x \leq 275$ m. The flow is from left to right. (a) The vertical velocity determined using the numerical model for a flow with a constant background velocity of 0.15 m/s including viscosity. (b) The vertical velocity found using the analytical solution to the Taylor Goldstein equation for a constant velocity of 0.15 m/s. (c) The vertical velocity found using the analytical solution to the Taylor Goldstein equation for a constant velocity of 0.159 m/s.

The near resonant mode 1 response in the model does not correspond very well to the analytical resonant mode 1 response, as shown in Subsection 4.2.1. Furthermore, the mode 2 and 3 results also do not match exactly to the corresponding analytical solution. Therefore, a constant background velocity away from the resonant point is simulated. Away from the resonant point small deviations in background velocity should result in small deviations in the vertical velocity profile, since no steep peaks are present. In this way, it can be determined whether the deviation only occurs near the resonance peak or for all velocities. A constant background velocity of 0.36 m/s should result in a 1.25 mode response according to theory. The results of a model simulation with background velocity 0.36 m/s, as well as its analytical solution are shown in Figure C.3 (a) and (b) respectively. The model response is a clear near mode 1 and does not match its analytical solution. When comparing the model results of 0.36 m/s, Figure C.3 (a), to an analytical solution with a 17.2% higher background velocity of 0.422 m/s, Figure C.3 (c), a good agreement is found. The mode corresponding to a background velocity of 0.422 m/s in the theoretical solution is 0.96.

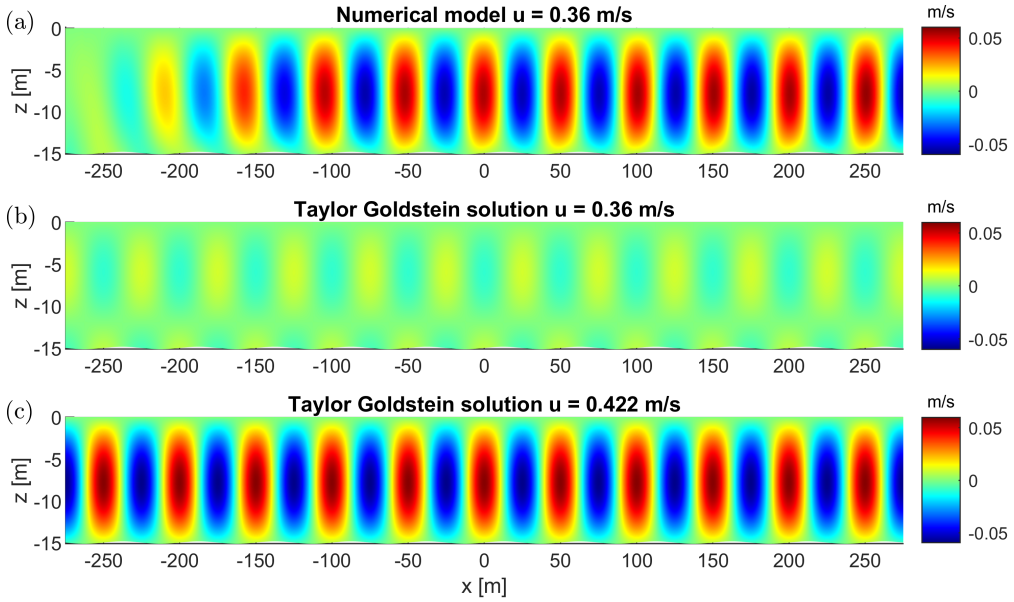

Figure C.3: Steady flow between mode 1 and 2. Bed waves of amplitude 0.15 m are present over $-275 \leq x \leq 275$ m. The flow is from left to right. (a) The vertical velocity determined using the numerical model for a flow with a constant background velocity of 0.36 m/s including viscosity. (b) The vertical velocity found using the analytical solution to the Taylor Goldstein equation for a constant velocity of 0.36 m/s. (c) The vertical velocity found using the analytical solution to the Taylor Goldstein equation for a constant velocity of 0.422 m/s.

A constant background velocity of 0.18 m/s, which is theoretically between mode 2 and 3, deviates from its analytical solution as well, as shown in Figure C.4. The model result are more consistent with the analytical solution of a 19.4% higher background velocity than the one prescribed in the model. A background velocity of 0.18 m/s corresponds to mode 2.65 according to theory, which is about as far away from the resonance peaks as possible. Therefore, the difference in velocity amplitude can not be explained by a slightly different location on the resonance peak due to numerical errors.

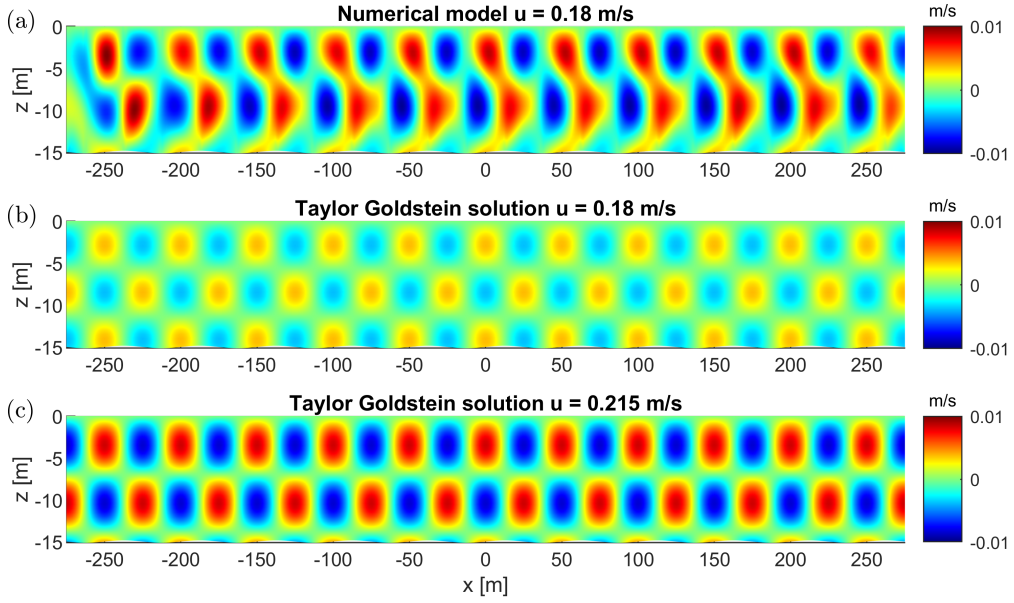

Figure C.4: Steady flow between mode 2 and 3. Bed waves of amplitude 0.15 m are present over $-275 \leq x \leq 275$ m. The flow is from left to right. (a) The vertical velocity determined using the numerical model for a flow with a constant background velocity of 0.18 m/s including viscosity. (b) The vertical velocity found using the analytical solution to the Taylor Goldstein equation for a constant velocity of 0.18 m/s. (c) The vertical velocity found using the analytical solution to the Taylor Goldstein equation for a constant velocity of 0.215 m/s.

C.1.2. Decelerating flow

A decelerating flow and the related stationary Taylor Goldstein solutions are shown in Figure C.5. In this simulation a velocity profile at the boundary of $u(t) = 0.5\cos\left(\frac{\pi}{22350}t\right)$ is prescribed, to be able to compare the results to existing literature in which this velocity profile is applied as well. In Figure C.5 (a) the flow is supercritical. The flow decelerates further and approaches mode 1 in Figure C.5 (b). In Figure C.5 (c) the mode 1 response reaches its maximum. The mode 1 response remains present in most of the domain in Figure C.5 (d) except from -275<x<-200 where the mode 1 response has moved slightly downstream. In Figure C.5 (e) a starting mode 2 response is visible, e.g. between -275<x<-200 and -50<x<0, the rest of the domain remains mode 1. Figure C.5 (f) and C.5 (g) are similar to C.5 (e), no modes higher than mode 2 are observed. The analytical solution corresponding to the background velocity in Figure C.5 (a) until (g) are shown in C.5 (h) until (n). Figure C.5 (h) shows a resonant mode 1 response. At the lower velocity in Figure C.5 (i) the resonance conditions are not satisfied and the amplitude of the response drops, equally for C.5 (j). Mode 2 resonance is approached in Figure C.5 (k). In Figure C.5 (l) the mode 2 resonance has been passed leading to a reduction in vertical velocity magnitude. Mode 3 resonance is reached in Figure C.5 (m). Figure C.5 (n) shows a response between mode 4 and 5. The model results and analytical solution do not match, which is expected due to the non-steady flow used in the simulations. The model results only show a mode 1 response, no higher modes besides a small starting mode 2 are observed. Therefore, the mode 1 dominates the other modes. The resonant mode 1 response occurs around 0.31 m/s in the model, which is a 24% deviation from the theoretical value of 0.406 m/s.

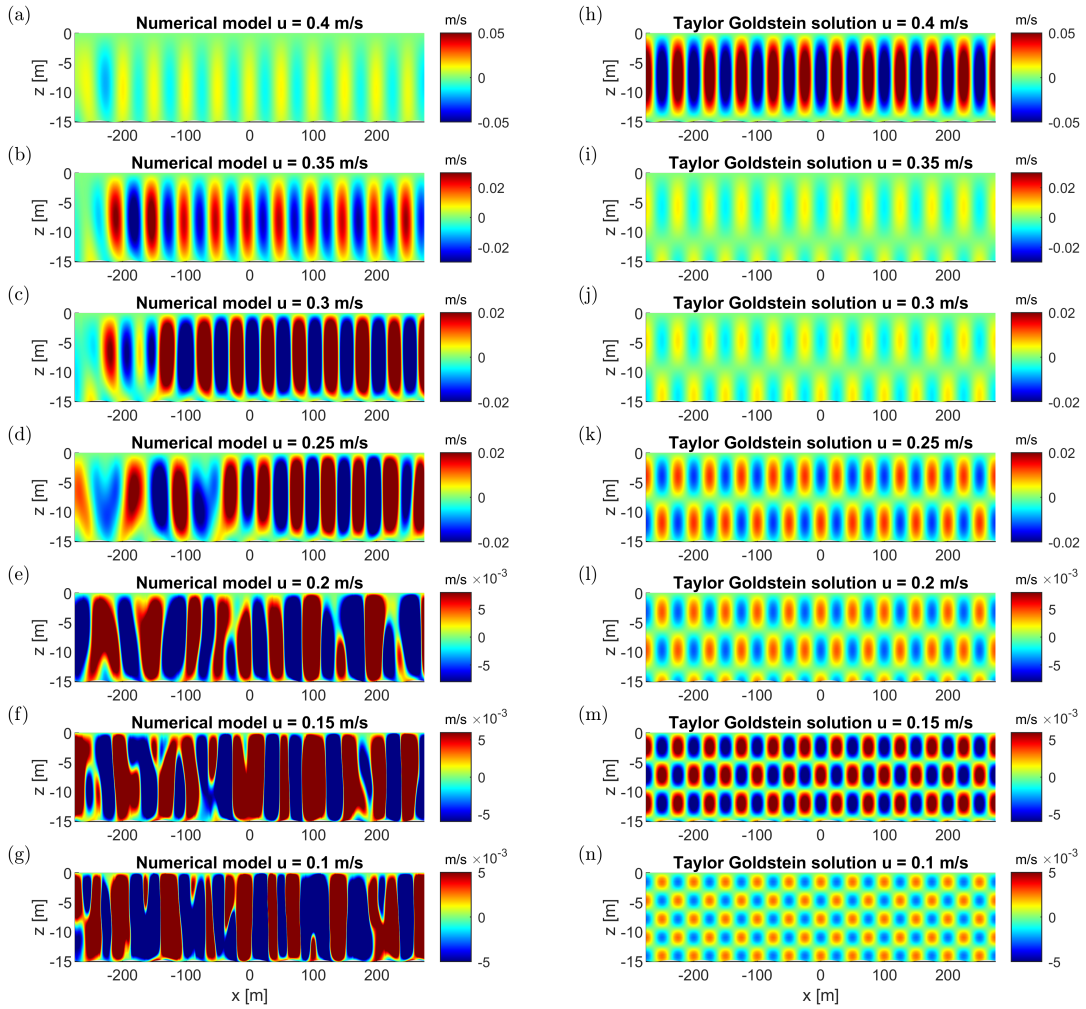

Figure C.5: Decelerating flow. Bed waves of amplitude 0.15 m are present over $-275 \leq x \leq 275$ m. The flow is from left to right. Plots (a) until (g) show the vertical velocity determined using the numerical model for a decelerating flow, $u = 0.5\cos(\frac{\pi t}{22350})$ m/s including viscosity. Plots (h) until (n) show the vertical velocity found using the stationary analytical solution to the Taylor Goldstein equation for the velocities corresponding to the numerical plots.

C.1.3. Accelerating flow

An accelerating flow and the related stationary Taylor Goldstein solutions are shown in Figure C.6. The simulation set-up is the same as for the decelerating flow except the background velocity is increasing instead of decreasing. The velocity profile prescribed at the open boundaries is $u(t) = 0.5\sin(\frac{\pi}{22350}t)$. Figure C.6 (a) shows the presence of higher modes. A mode 3 response is visible in Figure C.6 (b). In Figure C.6 (c) the mode 2 response is approached. The mode 2 response is still present in Figure C.6 (d). The mode is transitioning from 2 to 1 in Figure C.6 (e). Figure C.6 (f) shows a mode 1 response. The mode 1 response is still present in Figure C.6 (g). The stationary analytical solution corresponding to the background velocity in Figure C.6 (a) until (g) are shown in C.6 (h) until (n). Figure C.6 (h) shows a response between mode 4 and 5. Mode 3 resonance is shown in Figure C.6 (i). In Figure C.6 (j) the response is approaching mode 2, similar to C.6 (k). The mode 2 response is weakening in Figure C.6 (l). In Figure C.6 (m) mode 1 is approached. Finally, Figure C.6 (n) shows a resonant mode 1 response. A reasonable match between model and theory is observed. The modes of the internal waves are quite in line with theoretical expectations except for the amplitude of the vertical velocity in Figure C.6 (f). The mode of the model response is close to the one expected from theory. The resonant mode 1 response occurs in the model around 0.38 m/s and at 0.406 m/s according to theory, which is a deviation of about 7.5%.

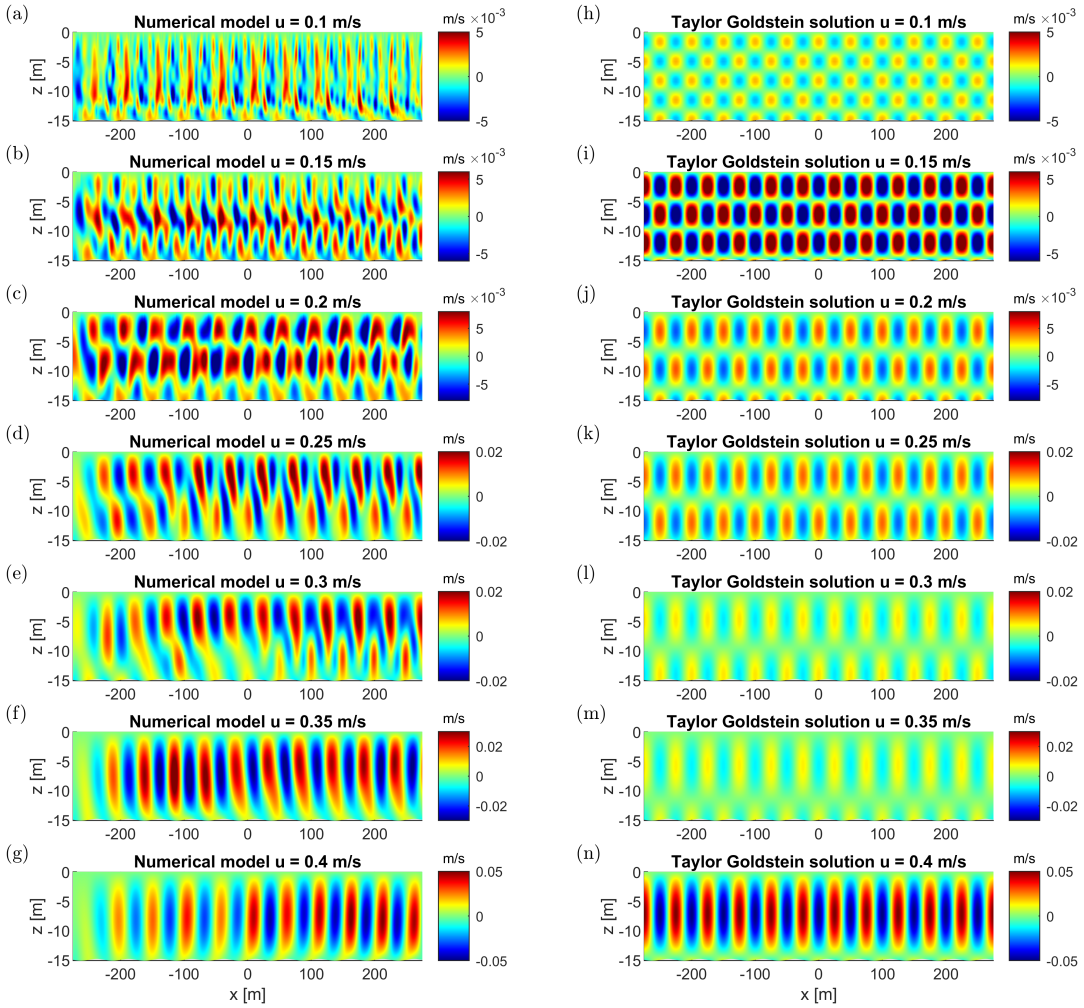

Figure C.6: Accelerating flow. Bed waves of amplitude 0.15 m are present over $-275 \leq x \leq 275$ m. The flow is from left to right. Plots (a) until (g) show the vertical velocity determined using the numerical model for a accelerating flow, $u = 0.5\sin(\frac{\pi t}{22350})$ m/s including viscosity. Plots (h) until (n) show the vertical velocity found using the analytical solution to the Taylor Goldstein equation for the velocities corresponding to the numerical plots.

A difference between the accelerating and decelerating flow is observed. The accelerating flow shows higher modes and the decelerating flow does not. Moreover, the amplitude of the vertical velocity is one order of magnitude higher for the lower background velocities in the decelerating flow than in the accelerating flow, order 10^{-2} m/s and 10^{-3} m/s respectively. This could be due to the fact that the turbulent motions are more complex in a decelerating flow than in an accelerating flow. In an decelerating flow the pressure gradient causes a force in the direction opposite to the flow direction. Therefore, both the pressure force and dissipation force have to be balanced by the decelerating flow, creating larger turbulent motions and allowing the internal waves to stay in the domain. Whereas, in an accelerating flow the pressure gradient is in the flow direction. The internal waves are forced to propagate in downstream direction out of the domain. Therefore, no superposition of modes is present. Using Equation 2.17 the flow state is determined for each mode. In the decelerating flow, the flow is subcritical after the resonant mode is generated. In contrast, the flow is supercritical after the resonant mode is generated in an accelerating flow. Therefore, the generated resonant modes remain in the domain longer for a decelerating flow than for an accelerating flow.

C.1.4. Deceleration rate

The results of a decelerating flow with a deceleration rate of $9.3 \cdot 10^{-5}$ m/s² are shown in Figure C.7. The internal waves reach their maximum amplitude at approximately 0.29 m/s. The mode 1 response remains present in the domain until the end of the simulation. In Figure C.7 (f) and (g) the internal waves no longer have their sinusoidal shape. The results of a decelerating flow with a deceleration rate of $4.6 \cdot 10^{-5}$ m/s² are shown in Figure C.8. The internal waves reach their maximum amplitude at approximately 0.31 m/s. In Figure C.8 (d) until (g) the internal waves no longer have their sinusoidal shape. The non-linear effects start earlier than in the simulation with a deceleration rate of $9.3 \cdot 10^{-5}$ m/s². For a smaller deceleration rate, the simulation takes more time. Therefore, the non-linear effects occur at a higher background velocity for a smaller deceleration rate. The results of a decelerating flow with a deceleration rate of $5.4 \cdot 10^{-6}$ m/s² are shown in Figure C.9. The internal waves reach their maximum amplitude for mode 1 at approximately 0.35 m/s, as depicted in Figure C.9 (b). In Figure C.7 (c) the wavelength of the internal waves has increased a lot. Furthermore, the internal waves no longer have their sinusoidal shape. The wavelength could increase due to lee waves propagating upstream interfering with the newly generated internal waves.

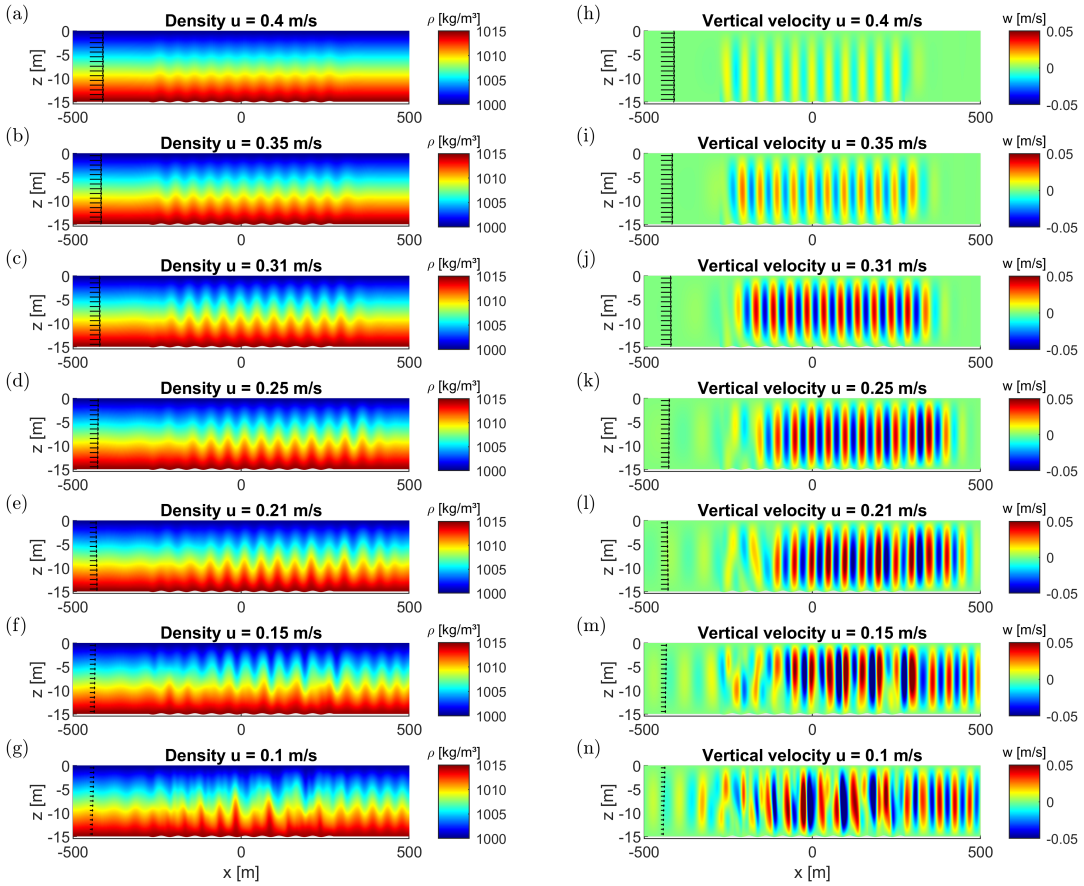

Figure C.7: Numerical simulation of a linearly decreasing flow velocity, deceleration rate $9.3 \cdot 10^{-5}$ m/s², excluding bottom friction. Bed waves of amplitude 0.15 m are present over $-275 \leq x \leq 275$ m. The flow is from left to right. Plots (a) until (g) show the density profile and plots (h) until (n) show the vertical velocity.

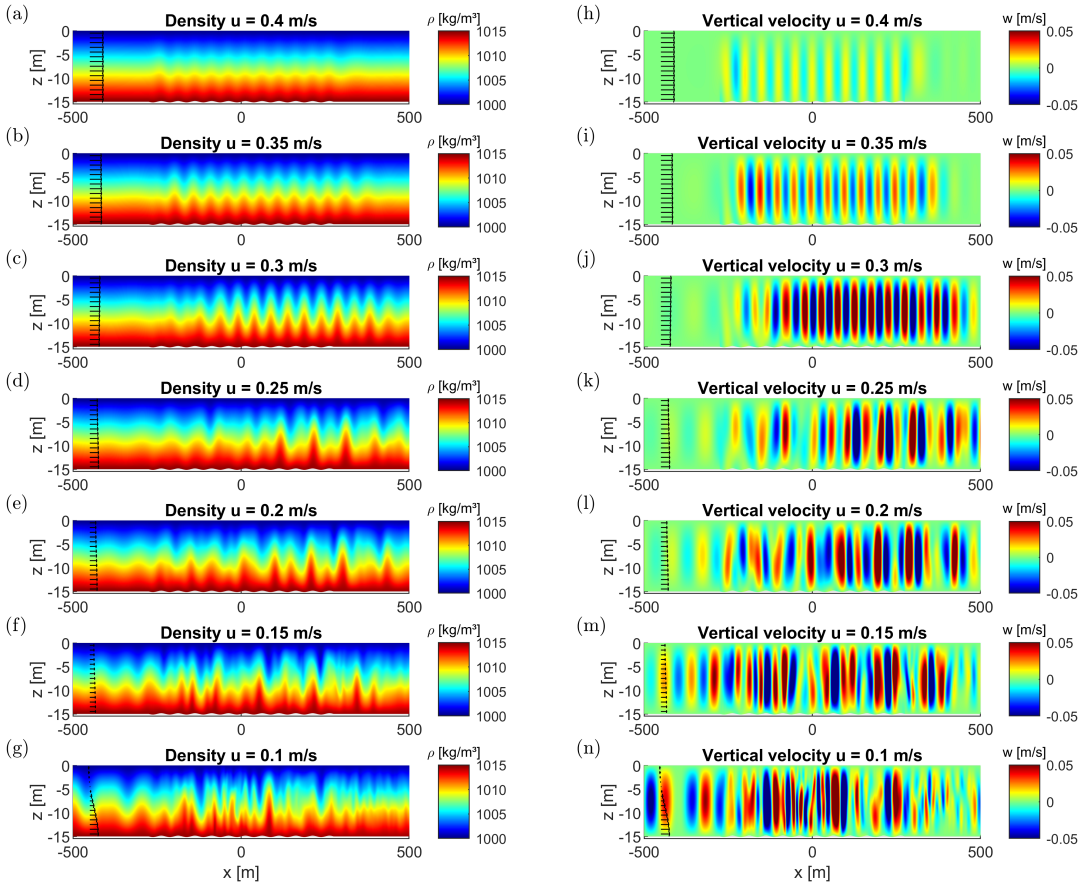

Figure C.8: Numerical simulation of a linearly decreasing flow velocity, deceleration rate $4.6 \cdot 10^{-5}$ m/s², excluding bottom friction. Bed waves of amplitude 0.15 m are present over $-275 \leq x \leq 275$ m. The flow is from left to right. Plots (a) until (g) show the density profile and plots (h) until (n) show the vertical velocity.

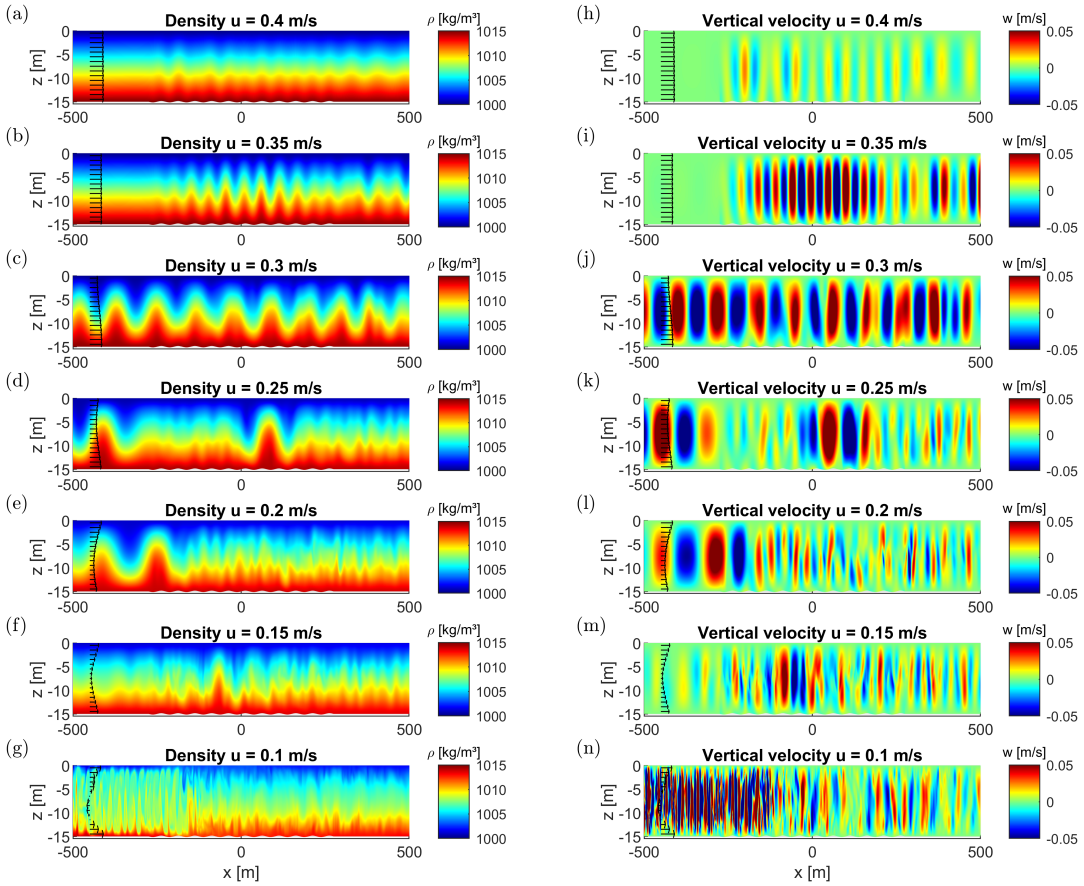

Figure C.9: Numerical simulation of a linearly decreasing flow velocity, deceleration rate $5.4 \cdot 10^{-6}$ m/s², excluding bottom friction. Bed waves of amplitude 0.15 m are present over $-275 \leq x \leq 275$ m. The flow is from left to right. Plots (a) until (g) show the density profile and plots (h) until (n) show the vertical velocity.

C.2. Parameter variation

The additional figures and corresponding descriptions of Section 4.3 are shown in this section.

C.2.1. Bottom friction

The results of a simulation that incorporates bottom friction are shown in Figure C.10. Compared to the base case without bottom friction, the amplitude of the internal waves is smaller. The internal waves reach their maximum amplitude at approximately 0.39 m/s, as depicted in Figure C.10 (b). The mode 1 response remains present in the domain until the end of the simulation. A mode 2 response or higher is not observed The background velocity profile is indicated by the black arrows. This profile follows a logarithmic pattern due to the influence of bottom friction. As the flow decelerates, a recirculation current begins to form near the bed. In Figure C.10 (c) through (h), the horizontal velocity arrows near the bed point in the opposite direction compared to those near the surface.

C.2.2. Bed wave amplitude

The results of a simulation using larger bed waves of amplitude 0.5 m are shown in Figure C.11. The amplitude of the internal waves is larger than for the base case with smaller bed waves of 0.15 m amplitude. The internal waves reach their maximum amplitude around 0.24 m/s, Figure C.11 (e). The internal waves grow to a larger amplitude due to the larger bed waves and additional energy available for internal wave generation. Due to the time scale effect, more time is needed to reach the equilibrium of larger internal waves. This results in a lower background velocity at which the maximum amplitude is reached. Below a background velocity of 0.2 m/s the internal waves start to break, Figure C.11 (f) until (h). The mode 1 response and breaking of these internal waves remains in the domain until the end of the simulation. A mode 2 response or higher is not observed.

The results of a simulation using larger bed waves of amplitude 0.5 m and including bottom friction are shown in Figure C.12. The amplitude of the internal waves is larger than for simulation #6 with smaller bed waves of 0.15 m amplitude. The internal waves reach their maximum amplitude around 0.36 m/s, Figure C.12 (b). The internal waves grow to a larger amplitude compared to the case with smaller bed waves and bottom friction. The internal waves start to break in the bottom half of the simulation at background velocities below 0.18 m/s and additional mixing is observed, Figure C.12 (f) until (h). A mode 2 response or higher is not observed.

C.2.3. Stratification profile

The results of a simulation using a tangent hyperbolic stratification profile are shown in Figure C.13. The internal waves are generated after 7000 s. The resonant mode 1 response is observed around a background velocity of 0.42 m/s, which occurs at time 8100 s. The internal waves then have an amplitude of 1.1 m. The internal waves propagate downstream from Figure C.13 (a) until (e). Thereafter, the internal waves start to propagate upstream and amplify further, Figure C.13 (f) until (h).

The results of a simulation using a tangent hyperbolic stratification profile, bottom friction and bed waves of amplitude 0.5 m are shown in Figure C.14. The resonant mode 1 is observed around 0.38 m/s and the internal waves have an amplitude of 0.5 m, Figure C.14 (c). Below a background velocity of 0.28 m/s boundary effects propagate into the domain of interest, Figure C.14 (e) until (h). The internal waves generated at the boundaries are caused by a mismatch between the velocity profile in the domain and the velocity profile prescribed at the boundary. The logarithmic profile caused by the bottom friction is slightly different for a linear or tangent hyperbolic stratification profile.

C.2.4. Turbulence model

The results of a simulation using the $k - \epsilon$ model for turbulence closure and bed waves of amplitude 0.15 m are shown in Figure C.15. The resonant mode 1 response is observed around 0.3 m/s. The internal waves then have an amplitude of 1 m. Internal wave breaking is not observed for bed waves of amplitude 0.15 m. The results of a simulation using the constant eddy viscosity model for turbulence closure and bed waves of amplitude 0.15 m are shown in Figure C.16. The resonant mode 1 response is observed around 0.3 m/s and the internal waves then have an amplitude of 1 m. Internal wave breaking is again not observed for bed waves of amplitude 0.15 m. The results found are similar to the base case, which uses Large Eddy Simulation for turbulence closure. Therefore, the turbulence model has no influence on the internal wave generation when the internal waves do not break.

To determine the influence of the turbulence model on breaking internal waves, simulations using larger bed waves are analysed. The results of a simulation using the $k - \epsilon$ model for turbulence closure and bed waves of amplitude 0.5 m are shown in Figure C.17. The resonant mode 1 response is observed around 0.25 m/s. The internal waves have an amplitude of 3.5 m. The internal waves start to break at about 9500 s and the amount of breaking increase as the flow decelerates further. The results of a simulation using the constant eddy viscosity model for turbulence closure and bed waves of amplitude 0.5 m are shown in Figure C.18. The resonant mode 1 response is observed around 0.25 m/s and the observed internal waves have an amplitude of 3.5 m. The internal waves start to break at about 9500 s and the breaking increases as the flow decelerates further. These results are similar to the base case. The breaking starts around the same time step for all three models and shows a similar pattern. Therefore, the turbulence model seems to have little influence on the internal wave generation.

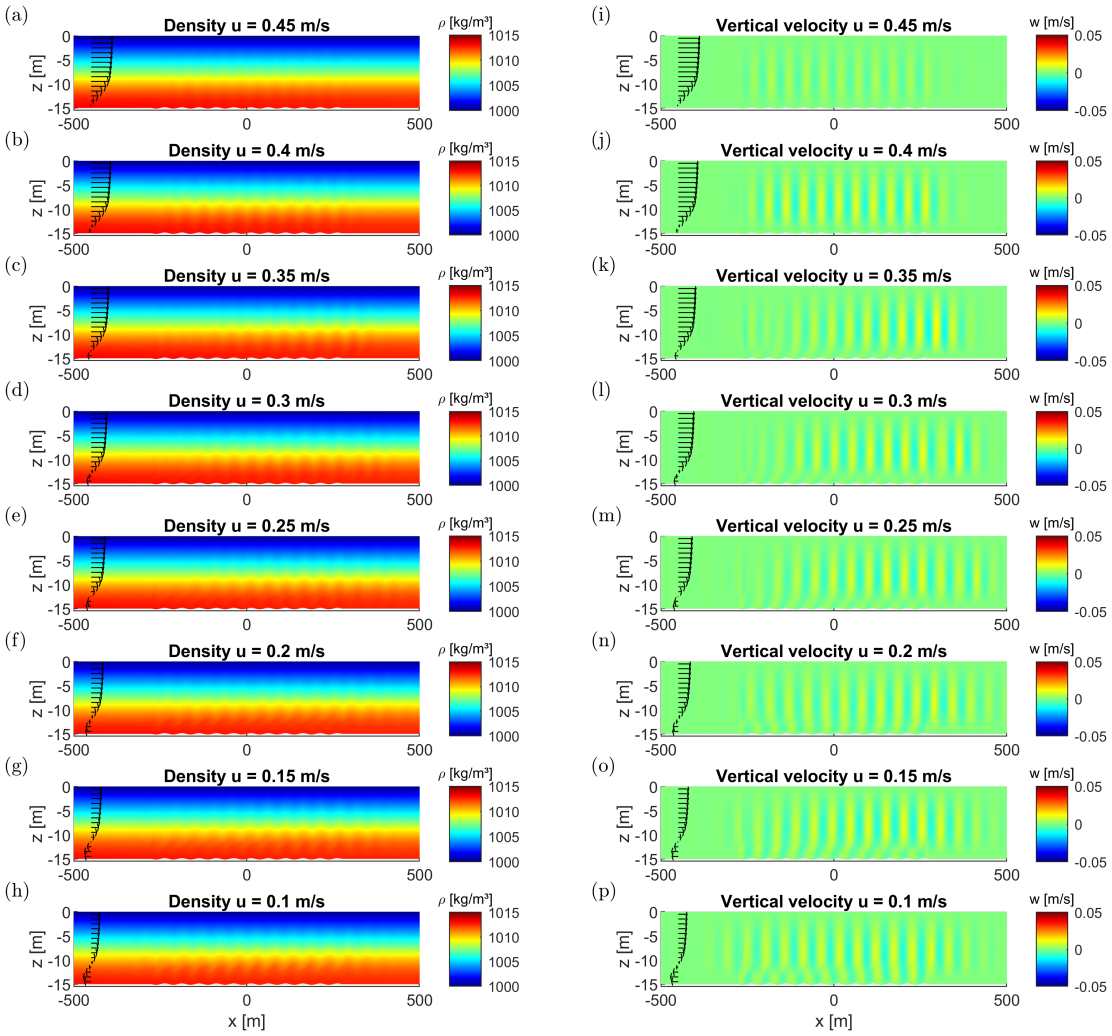

Figure C.10: Numerical simulation of a decelerating flow including bottom friction, simulation #6 of Table 3.3. Bed waves of amplitude 0.15 m are present over $-275 \leq x \leq 275$ m. The flow is from left to right. Plots (a) until (h) show the density profile and plots (i) until (p) show the vertical velocity.

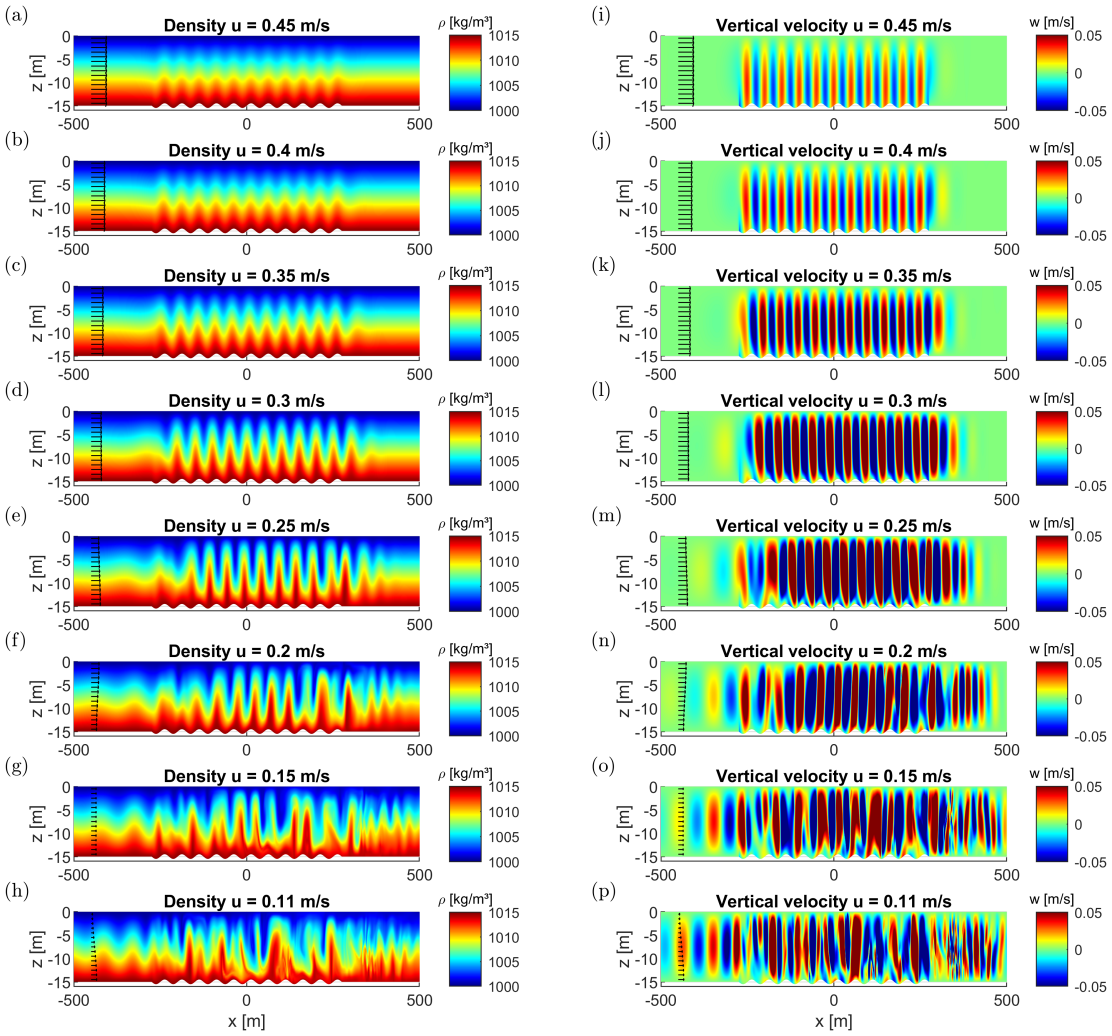

Figure C.11: Numerical simulation of a decelerating flow and bed waves of amplitude 0.5 m over $-275 \leq x \leq 275$ m, simulation #3 of Table 3.3. The flow is from left to right. Plots (a) until (h) show the density profile and plots (i) until (p) show the vertical velocity.

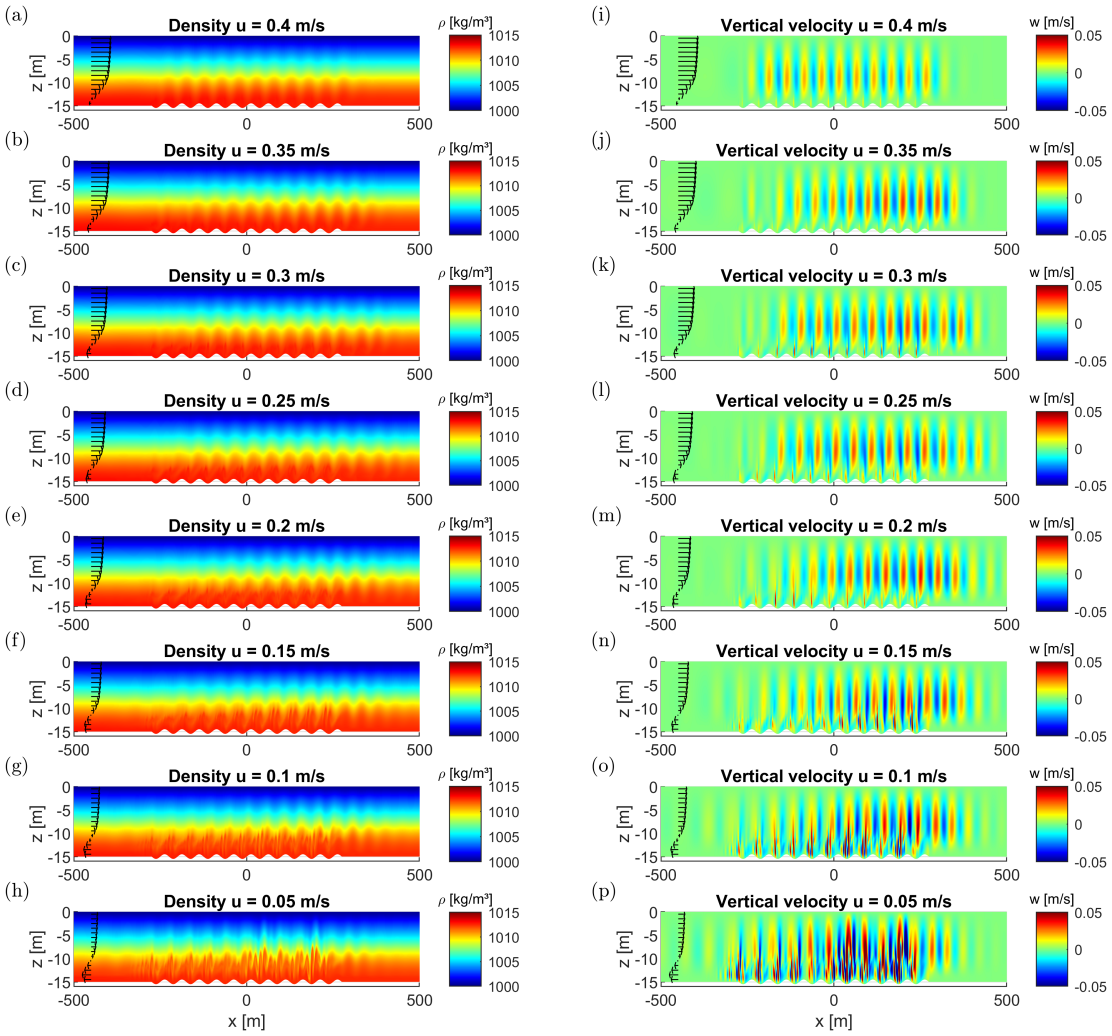

Figure C.12: Numerical simulation of a decelerating flow including bottom friction and bed waves of amplitude 0.5 m over $-275 \leq x \leq 275$ m, simulation #7 of Table 3.3. The flow is from left to right. Plots (a) until (h) show the density profile and plots (i) until (p) show the vertical velocity.

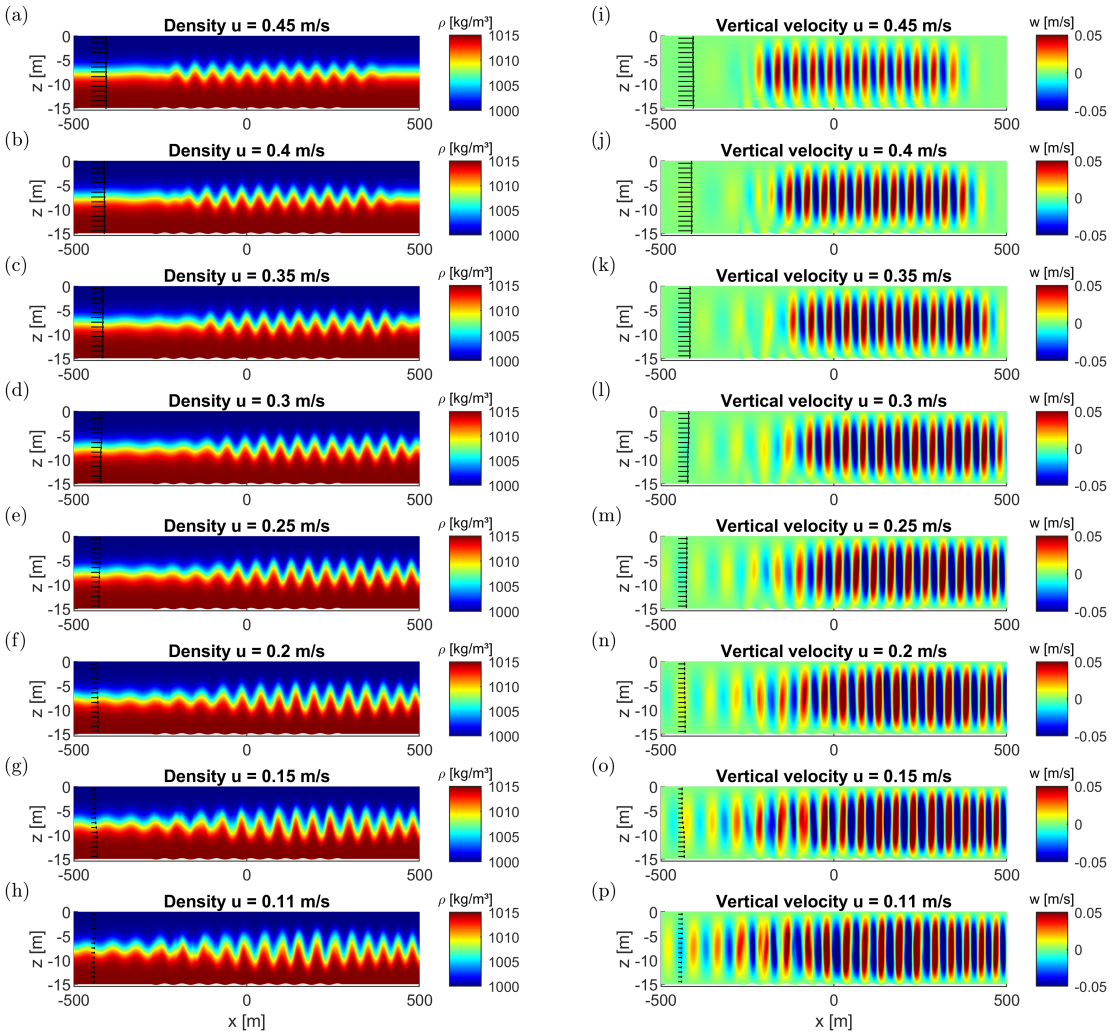

Figure C.13: Numerical simulation of a decelerating flow with a tangent hyperbolic stratification profile. Bed waves of amplitude 0.15 m are present over $-275 \leq x \leq 275$ m, simulation #9 of Table 3.3. The flow is from left to right. Plots (a) until (h) show the density profile and plots (i) until (p) show the vertical velocity.

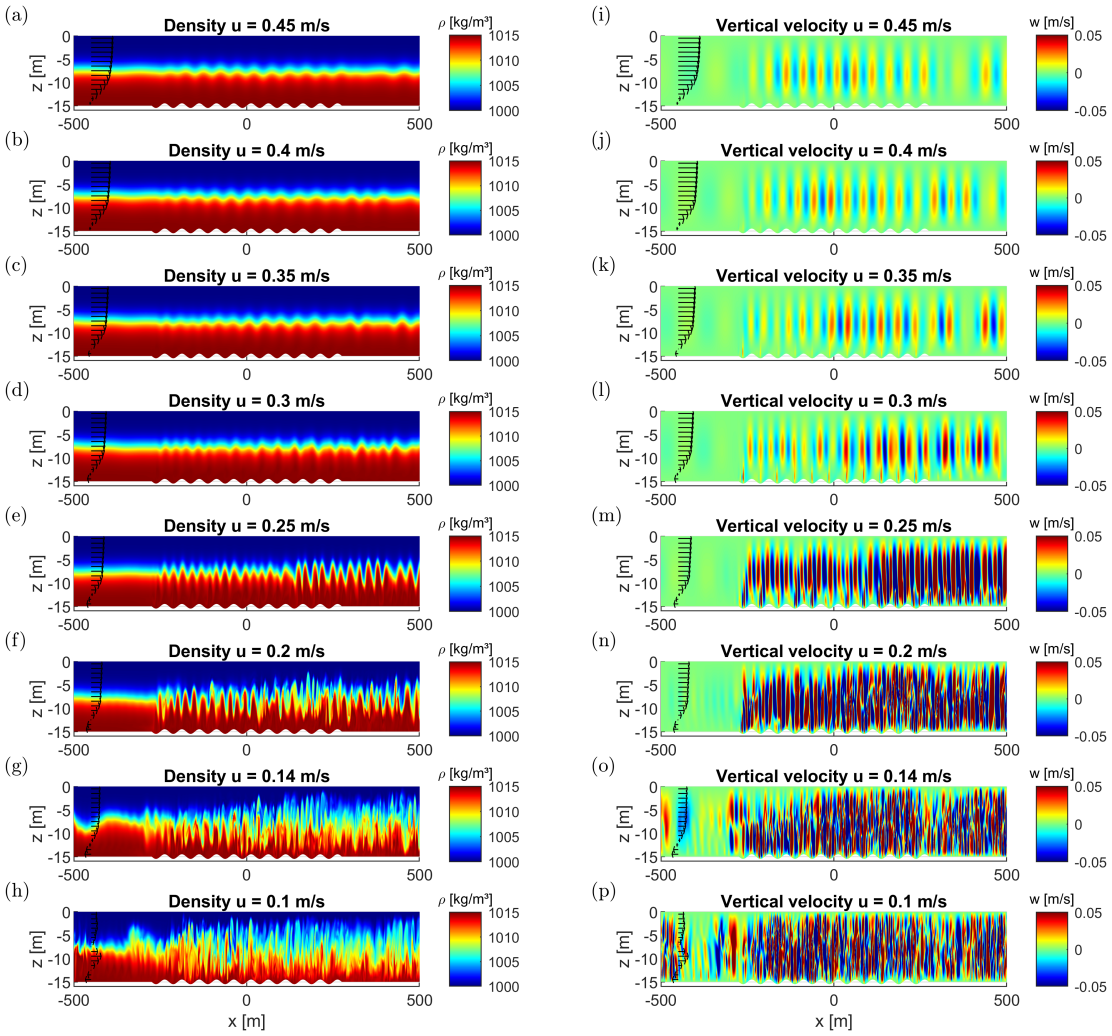

Figure C.14: Numerical simulation of a decelerating flow with a tangent hyperbolic stratification profile and including bottom friction. Bed waves of amplitude 0.15 m are present over $-275 \leq x \leq 275$ m, simulation #8 of Table 3.3. The flow is from left to right. Plots (a) until (h) show the density profile and plots (i) until (p) show the vertical velocity.

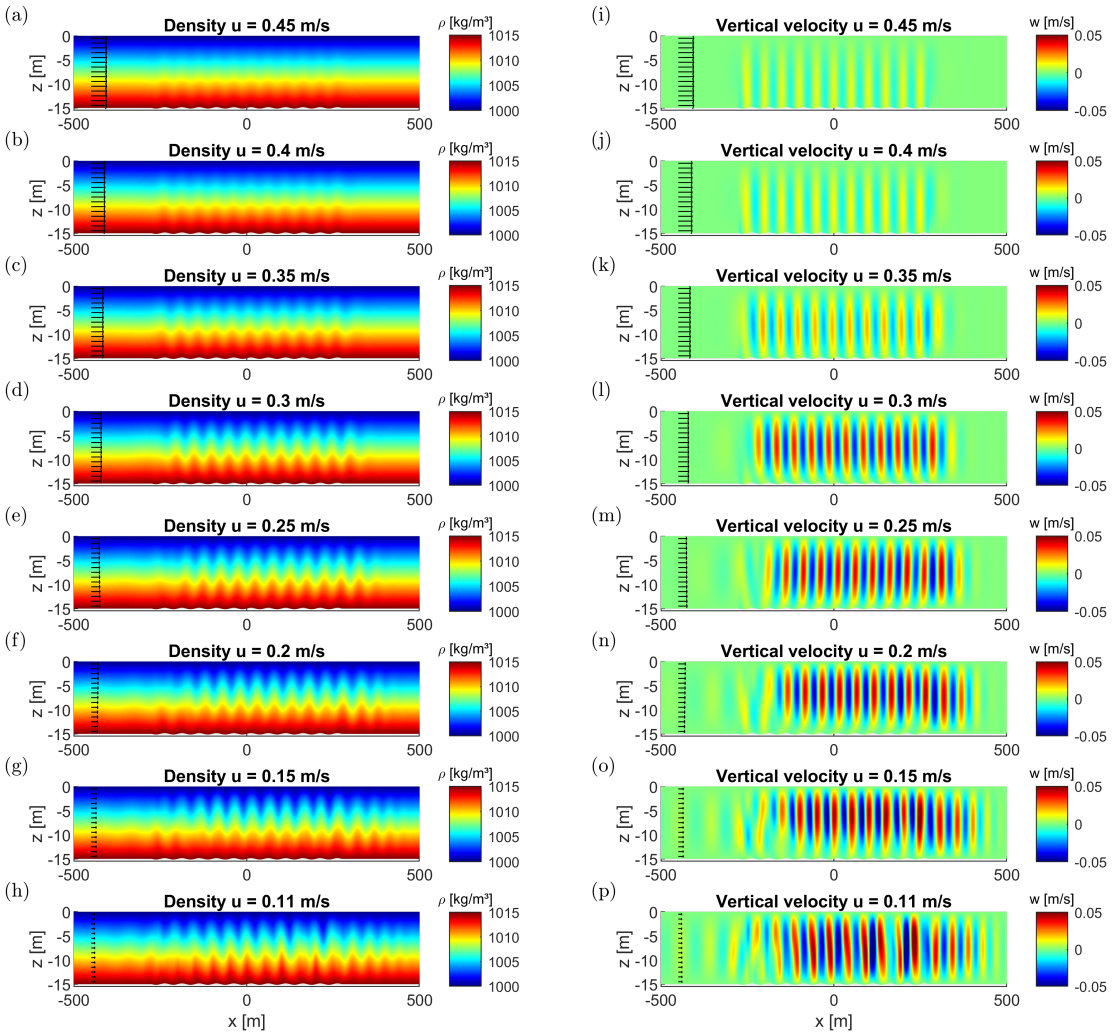

Figure C.15: Numerical simulation of a decelerating flow with $k-\epsilon$ turbulence model, simulation #1 of Table 3.3. Bed waves of amplitude 0.15 m are present over $-275 \leq x \leq 275$ m. The flow is from left to right and bottom friction is excluded. Plots (a) until (h) show the density profile and plots (i) until (p) show the vertical velocity.

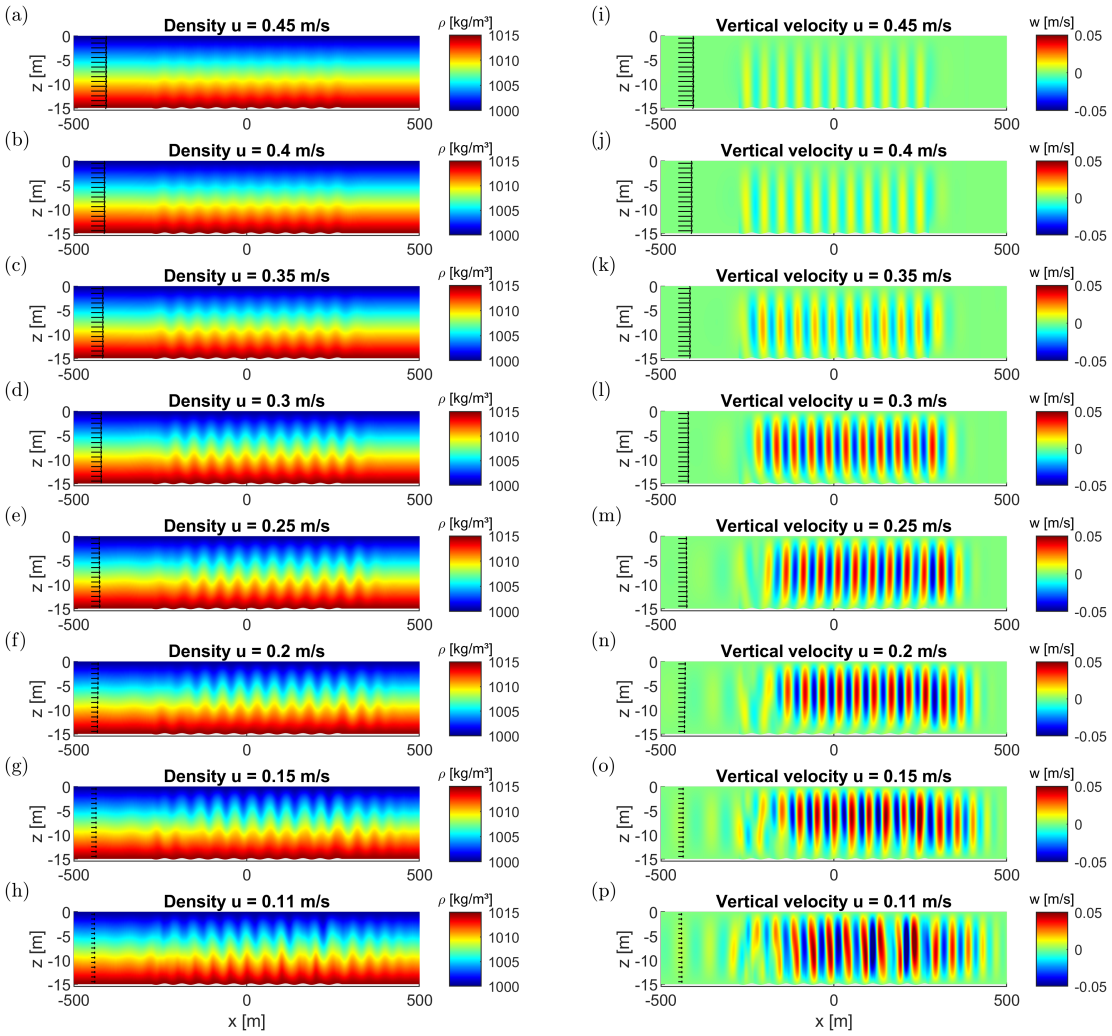

Figure C.16: Numerical simulation of a decelerating flow with $k-\epsilon$ turbulence model, simulation #2 of Table 3.3. Bed waves of amplitude 0.15 m are present over $-275 \leq x \leq 275$ m. The flow is from left to right and bottom friction is excluded. Plots (a) until (h) show the density profile and plots (i) until (p) show the vertical velocity.

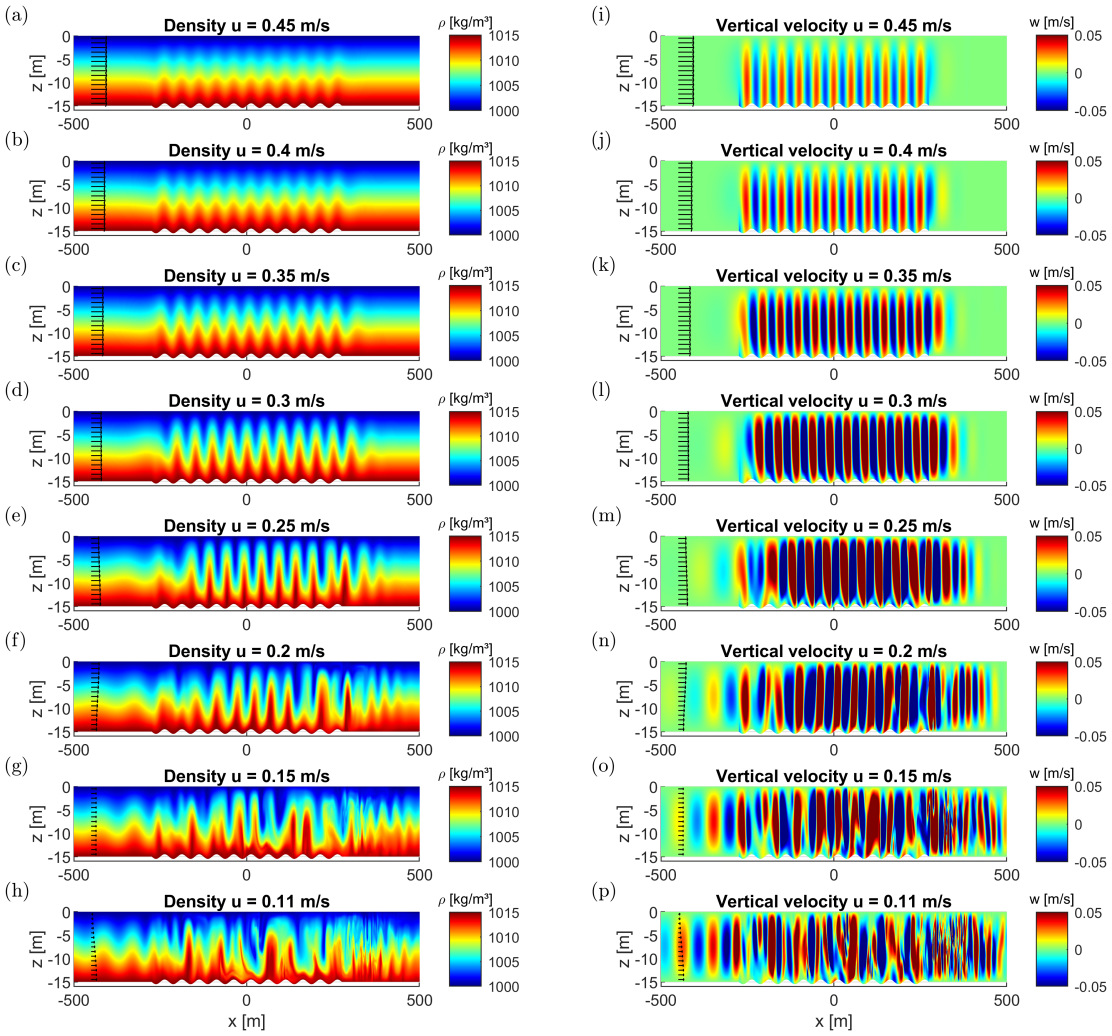

Figure C.17: Numerical simulation of a decelerating flow with $k-\epsilon$ turbulence model, simulation #4 of Table 3.3. Bed waves of amplitude 0.5 m are present over $-275 \leq x \leq 275$ m. The flow is from left to right and bottom friction is excluded. Plots (a) until (h) show the density profile and plots (i) until (p) show the vertical velocity.

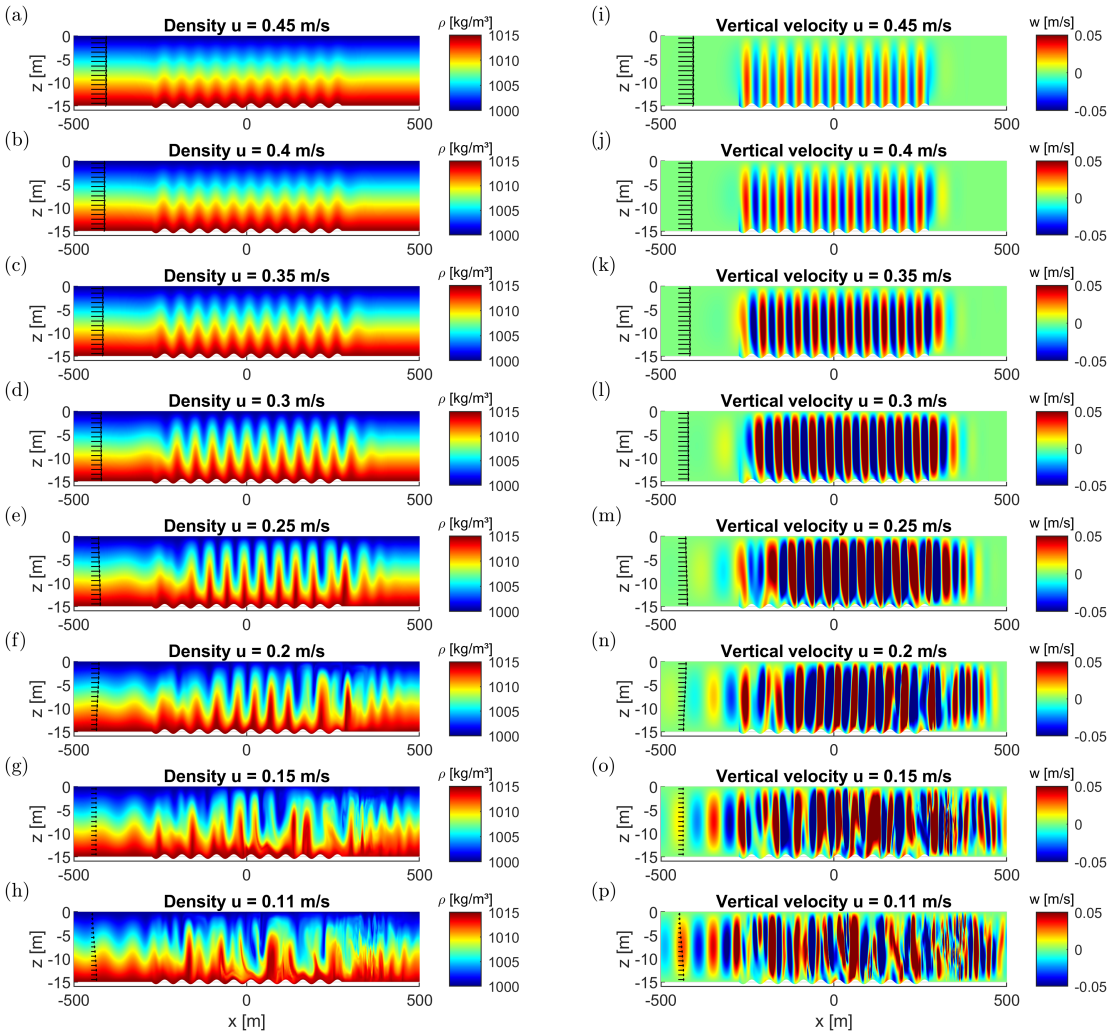

Figure C.18: Numerical simulation of a decelerating flow with $k-\epsilon$ turbulence model, simulation #5 of Table 3.3. Bed waves of amplitude 0.5 m are present over $-275 \leq x \leq 275$ m. The flow is from left to right and bottom friction is excluded. Plots (a) until (h) show the density profile and plots (i) until (p) show the vertical velocity.

D

Quantification irreversible mixing

D.1. Analytical solution

Calculation of the analytical solutions for a closed system, as well as the calculation of the boundary flux in an open system.

D.1.1. Lock exchange

The analytical solutions for the initial state of the lock exchange are determined. The integrals over the density profiles shown in Figure 5.1 are given below. The analytical solution of the potential energy in the initial state is

$$PE_{t0} = \int_0^{100} \int_1^{16} 1015\, g\, z\, dz\, dx + \int_0^{100} \int_1^{16} 1000\, g\, z\, dz\, dx = 252,031,163\ [J/m]. \tag{D.1}$$

The analytical solution of the background potential energy in the initial state is

$$BPE_{t0} = \int_0^{200} \int_1^{8.5} 1015\, g\, z\, dz\, dx + \int_0^{200} \int_{8.5}^{16} 1000\, g\, z\, dz\, dx = 251,203,444\ [J/m]. \tag{D.2}$$

The analytical solution of the background potential energy for a fully mixed domain in the initial state is

$$BPE_{mixed,t0} = \int_0^{200} \int_1^{16} 1007.5\, g\, z\, dz\, dx = 252,031,163\ [J/m]. \tag{D.3}$$

D.1.2. Constant flow

The analytical solution for a constant flow over a flat bed is determined. The analytical inflow and outflow of background potential energy is equal to

$$BPE_{in/out} = \int_1^{16} (1016 - z)\, g\, z\, u\, dz = 377,219\ [J/m/s]. \tag{D.4}$$

D.2. Flat bottom

To determine the mixing created by diffusion without the presence of bed waves a simulation using a flat bottom is executed. The increase in energy compared to the initial state is determined relative to the energy needed to fully mix the initial state is shown in Figure D.1. The increase in BPE over the simulation is 0.1% of the energy needed to fully mix the control volume. For a flat bottom no internal waves are created. Therefore, no available potential energy is created, which can be transferred reversibly to kinetic energy in the oscillating wave pattern. Thus the potential energy is equal to the background potential energy. The increase in background potential energy is caused by mixing generated by the diffusion of the turbulence model.

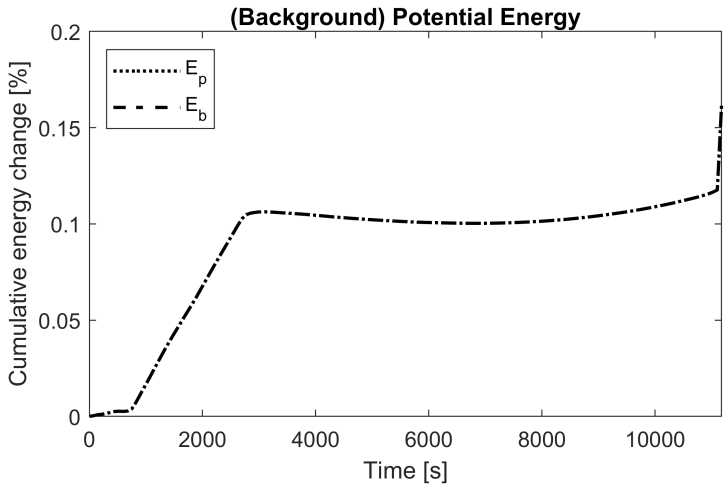

Figure D.1: The cumulative change in potential energy (E_p) and background potential energy (E_b) compared to the initial state relative to the energy needed to reach a fully mixed control volume is plotted for each time step for a simulation of a decelerating flow with a flat bottom, no bottom friction and viscosity.

The boundary flux of the background potential energy is determined. Using the boundary flux and the change of BPE in the control volume, the BPE production is determined using Equation 3.13. The individual terms of the energy balance from Equation 3.13 are determined relative to the energy needed to fully mix the initial state. The results are plotted in Figure D.2. The fluctuations in the beginning, until 3000 s, are caused by spin-up effects. The change in background potential energy, E_b, is negligible compared to the boundary flux, $E_{b,flux}$.

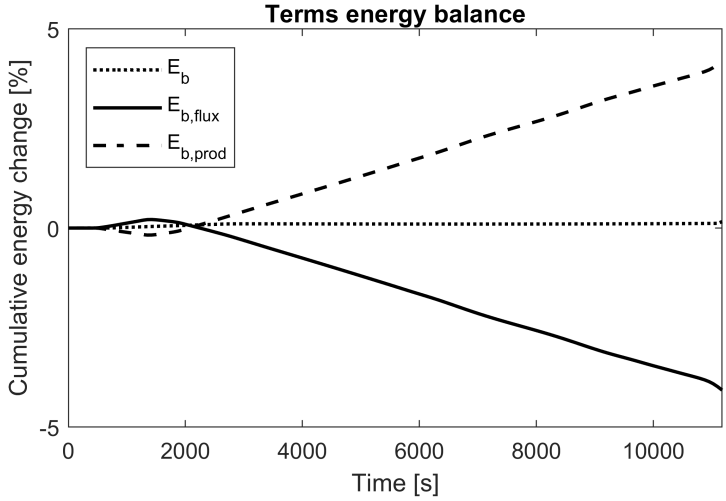

Figure D.2: Simulation of a decelerating flow using a flat bottom. Cumulative change in background potential energy, cumulative boundary flux of background potential energy and cumulative background potential energy production all relative to the energy needed to fully mix the control volume.

D.3. Turbulence model

The cumulative background potential energy in the control volume is plotted as a percentage of the background potential energy needed to fully mix the control volume in Figure D.3 for the turbulence closure models LES, $k-\epsilon$ and constant eddy viscosity. All three turbulence models follow a similar pattern. The constant eddy viscosity is between 0.1-0.2% above the other two models at all times. The internal waves are generated from 8000 s onwards. All models show a more fluctuating pattern from there onwards.

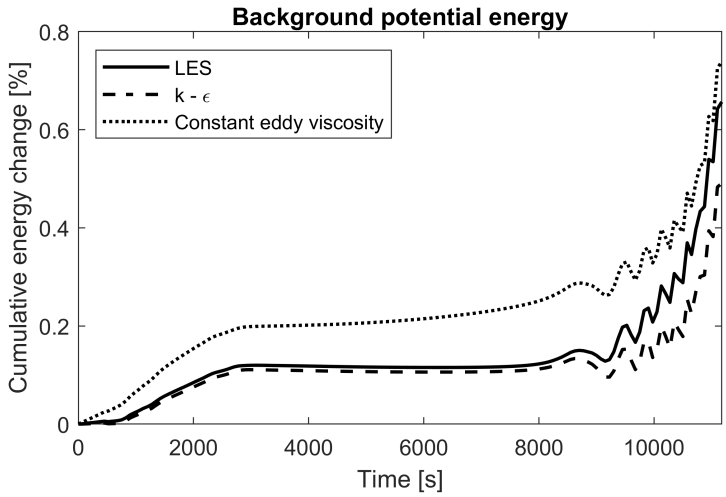

Figure D.3: The cumulative change in background potential energy (E_b) compared to the initial state relative to the energy needed to reach a fully mixed control volume for three different turbulence models. Simulation of a decelerating flow with bed waves of amplitude 0.15 m and no bottom friction.

D.4. Salt imported by estuarine circulation

The squared buoyancy frequency over time for three different simulations is plotted in Figure D.4. The results of a simulation of a flat bottom (#10) show a decrease in the buoyancy frequency at approximately 2000 s, spin-up effects cause this. After 2000 s the buoyancy frequency remains approximately constant for the simulation of the flat bed. The results of the simulation of bed waves of amplitude 0.15 m (#0) show the buoyancy frequency decreases when the internal waves are generated. Furthermore, similar spin-up effects as in the simulation of flat bed are observed at 2000 s. The results of the simulation of bed waves of amplitude 0.5 m (#3) show the buoyancy frequency decreases once the internal waves are generated. Furthermore, the buoyancy frequency drops more rapidly than in the case of the smaller bed waves. Again similar spin-up effects are observed in the first 2000 s.

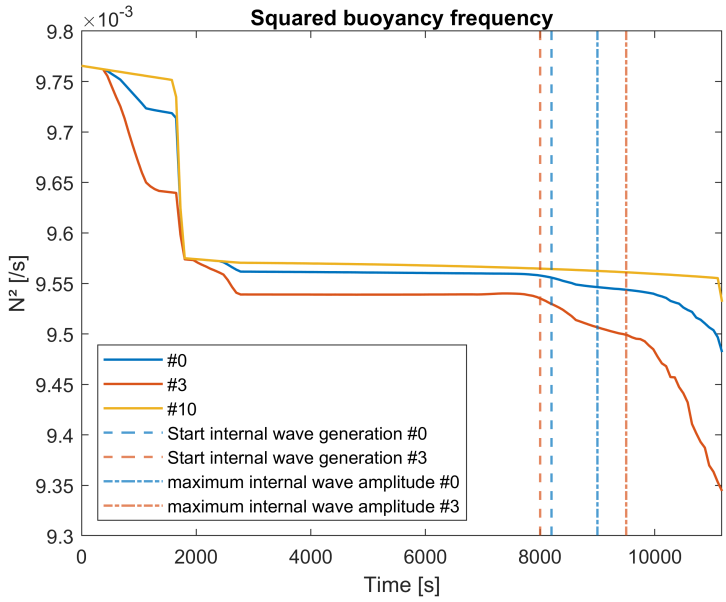

Figure D.4: Squared buoyancy frequency for a simulation with no friction and bed waves of 0.15 m (#0), a simulation with no friction and bed waves of 0.5 m (#3), and a simulation with no friction and flat bed (#10). The dashed vertical lines indicate the time step at which the internal waves start to be generated. The dash-dotted vertical lines indicate the time step at which the internal waves reach their maximum amplitude.